

5-1-2015

# Multi-scale models of ovarian cancer

Kimberly Rene Kanigel Winner

Follow this and additional works at: [https://digitalrepository.unm.edu/biol\\_etds](https://digitalrepository.unm.edu/biol_etds)



Part of the [Biology Commons](#)

---

## Recommended Citation

Kanigel Winner, Kimberly Rene. "Multi-scale models of ovarian cancer." (2015). [https://digitalrepository.unm.edu/biol\\_etds/58](https://digitalrepository.unm.edu/biol_etds/58)

This Dissertation is brought to you for free and open access by the Electronic Theses and Dissertations at UNM Digital Repository. It has been accepted for inclusion in Biology ETDs by an authorized administrator of UNM Digital Repository. For more information, please contact [disc@unm.edu](mailto:disc@unm.edu).

Kimberly Rene Kanigel Winner

*Candidate*

---

Biology

*Department*

---

This dissertation is approved, and it is acceptable in quality and form for publication:

*Approved by the Dissertation Committee:*

Helen J. Wearing, Co-chairperson

---

Melanie E. Moses, Co-chairperson

---

Bridget S. Wilson

---

Yi Jiang

---

---

---

---

---

---

**MULTI-SCALE MODELS OF OVARIAN CANCER**

**BY**

**KIMBERLY KANIGEL WINNER**

B.S., Biology, Fort Lewis College, 1997

DISSERTATION

Submitted in Partial Fulfillment of the  
Requirements for the Degree of  
**Doctor of Philosophy**

**Biology**

The University of New Mexico  
Albuquerque, New Mexico

**May, 2015**

## **DEDICATION**

To my father, David Michael Kanigel (1945-2010).

And to my beloved husband, Evans, and my son Peregrine, who are ever my comfort and  
inspiration.

## ACKNOWLEDGEMENTS

I must acknowledge my advisor, Melanie Moses, for sticking with me through everything. Her brilliant comprehension of both science and human nature have made her most formidable, but she makes herself an even more extraordinary mentor through her kindness and understanding.

I also would like to acknowledge my mentors and committee members Bridget Wilson and Yi Jiang, who have shared with me the tremendous gifts of their perspectives as extraordinarily seasoned, active, productive scientists. They have immersed me in projects at the cutting edge of computational and systems biology, given me the privilege of working with researchers of their exceptional caliber and talent, and, unbelievably, believed in me and my ability to push myself to work on difficult problems. My committee co-chair in Biology, Helen Wearing, has graciously given expert insights to our research and generally been exceedingly supportive and helpful. Notably, Dr. Wilson and Dr. Moses also supported me financially through the birth of my son Peregrine. Altogether, my committee is quite extraordinary, as well as the opportunities they have given me to grow on in science. I would also like to thank Professor Mara Steinkamp for being the key to integrating our experimental and theoretical data, her patience with my lack of understanding of the experimental side of our research, and for ushering me through the growing pains of becoming a more professional scientist. Finally, I must thank my initial biology sponsors, Mary Anne Nelson and Maggie-Werner Washburne,

who admitted me to the UNM Biology department, opened up the opportunity for me to build an interdisciplinary committee, and continued supporting me to the present day.

The faculty and students of Dr. Moses' Scalenet Lab, Dr. Wilson and Dr. Diane Lidke's labs, and the New Mexico Center for the Spatiotemporal Modeling of Cell Signaling have been wonderful. Becky Lee and Genevieve Phillips gave me expert, patient guidance and kind words in the UNM Cancer Research Center Microscopy Facility; Ryan Tanner always brought hugs and good conversation; and Michael Wester has been a steadfast mentor in scientific methods and mathematics, and a tremendously supportive friend. My fellow graduate students in biology, computer science, and the biomedical sciences have also been one of the best parts of graduate school. Their openness to thinking about any scientific problem, their emotional support, and their humor have been key to my experience and much of the reason for any successes I've had. Though so many people have been part of this experience, in particular, I acknowledge Joshua Hecker and his family Ashley and Penny, at whose home I completed this dissertation, Soumya Banerjee and his wife Joyeeta, Flor Espinoza, Tatiana Paz, Neal Holtschulte, Matthew Fricke, Francois Asperti-Boursin, Kenneth Letendre, Mario Paz, Anat Burger, and Meghan McCabe-now-Pryor: you have inspired me at every step along the way.

And I acknowledge my family, for whom I have no words to express my thanks for their absolute constancy, and who have jumped into the whole project with at least as much enthusiasm as I have. My mother, Vivian Kay Kanigel, cared for my son for 7 months before my defense; my sister and brother-in-law, Kara and Trent Copanas, have welcomed us into their home as we transition from New Mexico to Colorado; and my

husband's family, Ellen and Joe O'Laughlin and Keri Winner and Chris Chizzali gave us every kind of support and a sense of calm during stress storms, and would happily have had us co-habitate with them after our move. My aunts, uncles, and especially cousins from the Kanigel family, my Uncle Thomas Hammock, my stepsisters and their wonderful kids and all of our family friends have cheered me on for these many years. I am very lucky: this protective circle has always believed in me and has supported me physically, financially, and emotionally from beginning to end during this process. Finally, we have our old friends, who always helped keep my view wide and made me feel like the world was full of love.

# **MULTI-SCALE MODELS OF OVARIAN CANCER**

by Kimberly Kanigel Winner

B.S. Biology, Fort Lewis College, 1997

Ph.D. Biology, 2015

## **ABSTRACT**

In ovarian cancer, disease and treatment can be examined across multiple spatial scales including molecules, cells, intra-tumor vasculature, and body-scale dynamics of circulating drugs. Survival of primary tumor cells and their development into disseminated tumors is related to adhesion between the cells, attachment, and invasion. Growth of new tumors depends on the delivery of nutrients, which depends on the tumor diameter and the tumor's vasculature. Drug delivery also depends on tumor diameter and vasculature, and molecular- and gross-scale drug processes.

A cellular Potts simulation integrated data at these multiple scales to model microscopic residual disease during relapse after a primary surgery. The model generated new hypotheses about tumor cell behavior, and the effectiveness of drug delivery to tumors disseminated in the peritoneal cavity. First, the model required high intra-tumor adhesion in ovarian tumors, the existence of an unknown factor that drew tumor cells to vessels, a threshold of vascular endothelial growth factor (VEGF) for initiation of endothelial sprouting, and constitutive expression of angiogenic chemical messengers by tumor cells prior to needing oxygen. Alteration of the model incorporated drug delivery by the two standard routes, intraperitoneal and intravenous, from tumor vasculature parameterized from real patient data. Delivery of both small- and large-molecular weight therapies was superior during intraperitoneal therapy. Finally, empirical



and theoretical distributions of vessel radii were considered. Samples from tumors with each type of vascular morphology were run as though too distant from the peritoneal cavity to receive peritoneal delivery, with three results: first, intravenous delivery was superior to the secondary delivery into the circulatory system from a primary intraperitoneal delivery. Second, small molecules penetrated homogeneously across all cells, regardless of vascular volume or morphology, while antibodies penetrated heterogeneously, particularly in low-vessel-volume samples. Third, when each of the whole tumors was considered, this heterogeneity resulted in a large sub-population of cells that accumulated non-therapeutic levels of antibody, even during the best delivery scenario (IV). Fourth, delivery of antibodies was poorest in the empirical distribution. Finally, hypotheses were generated about the impact of heterogeneity of drug delivery, to be addressed as future questions.

## TABLE OF CONTENTS

<b>CHAPTER 1: INTRODUCTION.....</b>	<b>1</b>
<b>CANCER AS AN EVOLUTIONARY PROCESS .....</b>	<b>1</b>
<b>MOTIVATION .....</b>	<b>2</b>
<b>PROCESS OF DISSEMINATION, AND THE PERITONEAL ENVIRONMENT</b>	<b>3</b>
<b>COMPUTATIONAL BACKGROUND OF DRUG MODELS AND OVARIAN</b>	
<b>CANCER MODELS .....</b>	<b>5</b>
<b>MODELING METHODS IN DRUG DELIVERY .....</b>	<b>6</b>
<b>THE CELLULAR POTTS MODEL AS AN AGENT-BASED MODEL AND</b>	
<b>CELLULAR AUTOMATON .....</b>	<b>7</b>
<b>DISSERTATION SUMMARY .....</b>	<b>9</b>
<b>REFERENCES .....</b>	<b>12</b>
<b>CHAPTER 2: OVARIAN TUMOR ATTACHMENT, INVASION AND</b>	
<b>VASCULARIZATION REFLECT UNIQUE MICROENVIRONMENTS IN THE</b>	
<b>PERITONEUM: INSIGHTS FROM XENOGRAFT AND MATHEMATICAL</b>	
<b>MODELS .....</b>	<b>17</b>
<b>ABSTRACT .....</b>	<b>17</b>
<b>INTRODUCTION .....</b>	<b>18</b>
<b>MATERIALS AND METHODS .....</b>	<b>21</b>
<i>CELL CULTURE AND CELL LINES .....</i>	<i>21</i>
<i>INTRAPERITONEAL MOUSE MODEL OF OVARIAN CANCER RELAPSE .....</i>	<i>21</i>
<i>CO-INJECTION EXPERIMENTS.....</i>	<i>22</i>
<i>HISTOLOGY AND IMMUNOFLUORESCENCE.....</i>	<i>23</i>

<i>TRANSMISSION ELECTRON MICROSCOPY</i> .....	23
<i>THE OVARIAN TUMOR MODEL (OVTM)</i> .....	23
<b>RESULTS</b> .....	37
<i>STRONG HOMOTYPIC INTERACTIONS DRIVE SKOV3.IP AGGREGATION</i> .....	39
<i>TUMOR CELLS MIGRATE THROUGH THE OPEN ARCHITECTURE OF THE MESENTERY IN RESPONSE TO CHEMOTACTIC SIGNALS</i> .....	43
<i>SMALL SKOV3.IP1 TUMORS ATTACHED TO SURFACES OF THE STOMACH OR SMALL INTESTINE ARE NON-INVASIVE AND INITIATE ANGIOGENESIS</i> . ....	49
<i>SKOV3.IP1 TUMOR SPHEROIDS ARE INITIALLY WELL OXYGENATED AND LIKELY INDUCE NEOVASCULARIZATION VIA CONSTITUTIVE SECRETION OF ANGIOGENIC FACTORS</i> .....	52
<b>DISCUSSION</b> .....	55
<b>ACKNOWLEDGEMENTS</b> .....	61
<b>REFERENCES</b> .....	61
 <b>CHAPTER 3: SPATIAL MODEL OF DRUG DELIVERY ROUTE FOR TREATMENT OF DISSEMINATED OVARIAN CANCER</b> .....	 <b>66</b>
<b>ABSTRACT</b> .....	68
<b>INTRODUCTION</b> .....	70
<b>METHODS AND MATERIALS</b> .....	72
<i>DRUG PENETRATION INTO SPHEROIDS</i> .....	72
<i>OVARIAN CANCER XENOGRAFT MODEL</i> .....	73
<i>QUANTIFICATION OF VASCULATURE DENSITY AND VESSEL DIAMETER IN PATIENT TUMORS</i> .....	73

<i>CELLULAR POTTS MODEL</i> .....	74
<i>MODELING TUMOR VASCULAR NETWORKS</i> .....	77
<b>RESULTS</b> .....	78
<i>DRUG PENETRATION AND ACCUMULATION IN AVASCULAR TUMORS</i> .....	78
<i>VESSEL DENSITY OF HUMAN OVARIAN TUMORS AS PARAMETERS FOR</i> <i>MATHEMATICAL MODELING</i> .....	81
<i>SCHEMATIC OF THE MODELING APPROACH</i> .....	84
<i>CISPLATIN ACCUMULATION IN TUMOR CELLS AFTER IP OR IV DELIVERY IS</i> <i>INFLUENCED BY VASCULAR DENSITY</i> .....	86
<i>INTRAPERITONEAL DELIVERY OFFERS ADVANTAGES FOR THERAPEUTIC</i> <i>ANTIBODIES</i> .....	90
<b>DISCUSSION</b> .....	97
<b>ACKNOWLEDGEMENTS</b> .....	100
<b>AUTHOR CONTRIBUTIONS</b> .....	100
<b>SUPPLEMENTAL MATERIAL</b> .....	101
<i>REFERENCES FOR THE SUPPLEMENT</i> .....	111
<b>REFERENCES</b> .....	112
<b>CHAPTER 4: MESOSCOPIC TUMOR MODELS SHOW CORRELATIONS</b> <b>BETWEEN VASCULAR VOLUME, VESSEL MORPHOLOGY, AND DRUG</b> <b>DELIVERY</b> .....	<b>117</b>
<b>ABSTRACT</b> .....	118
<b>INTRODUCTION</b> .....	120
<b>METHODS</b> .....	125

<i>INITIALIZATION DATA SETS</i> .....	125
<b>RESULTS</b> .....	129
<b>DISCUSSION</b> .....	145
<b>ACKNOWLEDGEMENTS</b> .....	148
<b>REFERENCES</b> .....	149
<b>CHAPTER 5: CONCLUSION</b> .....	<b>150</b>

## **Chapter 1: Introduction**

This dissertation uses mathematical modeling to test and generate hypotheses about the dynamics of cancer. Models do not exist in a void without data from the real world. However, they can explore things we cannot measure easily in reality, they can do so quickly and with less expense than empirical studies, and they can develop and refine hypotheses to guide future experiments. Parameters in a model can be changed methodically and many replicates run quickly and efficiently to show the bounds in which they produce realistic and meaningful behavior. Extra processes can be added, to creatively explore what set of events may be producing the system's behavior. The results direct us to experimental efforts to confirm the new parameters and processes, producing useful and novel empirical results, more efficiently than if we had explored the same parameter space with experiments alone. In this work we examine cancer dynamics in order to parameterize models that we hope will identify processes that provide exploitable vulnerabilities in a direct, efficient manner.

### **Cancer as an evolutionary process**

Cancer is not always considered in evolutionary terms, but a tumor is a population of cells undergoing evolutionary pressures from their host, their own population<sup>1</sup>, and ultimately from toxic drugs, once a patient is diagnosed and begins chemotherapy. Cancer and tumors fit well into the paradigm of an ecosystem of individuals, in which the effects of living in a crowded space surrounded by other individuals with unique genetic make-ups can be advantageous, or competitive. Tumors create their own

microenvironment of growth factors and nutrient gradients, and interact with the external environment produced by the host<sup>1</sup>. Thinking about the cells as individuals collaborating, competing, and adapting to their local and global environment can help us to key in on the most critical characteristics, or, in networking terms, “connected nodes,” for the survival of a tumor’s individual cells and entire population. Therefore cancer biologists and ecologists continue to encourage researchers to try to exploit the ecological aspects of cancer<sup>1</sup>. While this is not always explicitly mentioned here in the model descriptions, it is important that it remains an undercurrent in thinking about and generating hypotheses about processes that could be targeted for treatment.

Our models began as attempts to recapitulate ovarian tumor morphology and behavior during cancer relapse. In the process, we realized that they could provide hypotheses for biological experimentation by showing us what was missing for the model – a quantifiable element such as a chemical concentration or a rate of cell movement, or what sequence of events led to our observations in microscopy images. We were then better able to produce testable hypotheses about the process of relapse in ovarian cancer and the efficacy of intraperitoneal and intravenous drug delivery.

## **Motivation**

Ovarian cancer is the tenth most common and sixth most deadly cancer in the U.S.<sup>2</sup>. Because it is largely asymptomatic, 61% of patients are diagnosed with late-stage cancer disseminated in the abdominal cavity, for which the five-year survival rate is 44%<sup>3</sup>. Tests for the early detection of ovarian cancer are under development<sup>4</sup>, but the unfortunate common case is that diagnoses are usually made at a late stage of cancer progression.

Tumors are found after noticeable abdominal distension, disruption of organ function, and buildup of fluid (ascites) in the peritoneal cavity after circulation blockage by tumor masses<sup>5</sup>.

### **Process of dissemination, and the peritoneal environment**

Ovarian tumor cells disseminate and seed within the abdominal, or peritoneal, cavity, and possibly metastasize via the bloodstream to abdominal organs<sup>6</sup>. The peritoneal cavity contains the ovaries and fallopian tubes, from the epithelia of which it is theorized primary tumors grow<sup>7, 8</sup>, and the other reproductive and digestive organs, to which secondary tumors disseminate. Single cells that come off of the primary ovarian tumor stick to one another in the peritoneal fluid. These cell clusters appear to have survival and drug resistance advantages, through avoidance of anoikis (cell death in cells needing adherence to other cells to survive), outer cells protecting those within the spheroid from drug molecules in the solution outside, and an overall lower replication rate reducing response to drug<sup>7</sup>.

Drug movement between the peritoneal (abdominal) and the blood plasma compartments is a key part of the pharmacokinetics affecting tumors in the peritoneal environment. 10-30ml of normal peritoneal fluid fills the space between organs. This fluid originates from the plasma, which convects into the interstitial spaces between cells, and then out from between the cells into the peritoneal cavity, and combines with a lubricant secreted by the cavity's monocellular lining of mesothelial cells<sup>9</sup>. The fluid circulates through the cavity and re-enters blood circulation via adjunct capillaries (40-50%), and through stomata on the underside of the diaphragm at the top of the cavity (50-



60%). The stomata can admit particles up to 25  $\mu\text{m}$  in diameter into the diaphragmatic lymphatics, which connect to the greater lymphatic system, which ultimately drains fluid back into the venous circulation, near the heart<sup>9</sup>. Because the blood and intraperitoneal compartments are intimately connected, we simultaneously model the initial drug bolus to the primary intraperitoneal (IP) or intravenous (IV) compartment, and the drug that appears in the secondary compartment (IV or IP, respectively).

After these disseminated metastases become noticeable and a diagnosis is made, surgeons begin treatment by resecting large tumor masses from the abdominal cavity and by scraping cavity surfaces. The remaining cells are termed microscopic residual disease or minimal residual disease.

Drugs are the primary defense against microscopic residual disease, including chemotherapy (small molecules) or therapeutic antibodies (large protein molecules) administered by intraperitoneal (IP, intra-abdominal) or intravenous (IV) injection. Delivering drug effectively to all tumor cells is of paramount importance to optimizing cell kill, which is correlated with improved survival<sup>10</sup> and reducing evolution of drug-resistant cells in tissue volumes exposed to lower drug concentrations. Many factors affect drug delivery, including physical barriers to drug penetration such as the vessel wall for large molecules, chemical barriers such as binding to non-target molecules, the half-life of the drug, which includes decay and elimination, and the surface area of tumor adjunct to compartments from which drug is delivered, such as blood volume and the peritoneal cavity. In the peritoneal cavity, remaining cells or newly developing tumors may receive limited exposure to intraperitoneal drug due to embedding in folds of normal tissue, or tissue adhesions that develop during tissue regrowth after surgery<sup>11</sup>.

Ovarian tumors exhibit a wide range of vascular densities. Spheroids floating in ascites are avascular<sup>7</sup>. We have also observed up to 10 percent vascular area in cross-section in tumors attached to organs in patients. The canonical model of vascularization is that tumors must reach approximately 1mm in diameter to become anoxic at their centers, and initiate angiogenesis. However, we have observed human ovarian (SKOV3.ip1) tumors grown in mice to be uniformly and densely vascularized in micro-tumors as little as 60 $\mu$ m, about ten cells, in diameter<sup>12</sup>. Residual disease exposed to chemotherapy will therefore likely have a wide range of vascularities.

### **Computational background of drug models and ovarian cancer models**

Mathematical modeling of drug delivery began in approximately 1960<sup>13,14</sup>. Since 2000, thousands of studies of drug penetration from vessels into tissues have had a modeling component (Google Scholar search, 4480 results, "mathematical model vessel drug penetration tissue"), including multi-scale models<sup>15,16</sup>. Sinek *et al.*<sup>17</sup> created a 2-dimensional multi-scale model of cisplatin and doxorubicin intravascular delivery to vascularized tumors. There is also an entire literature devoted to metabolic and spatial characteristics of cell spheroids grown *in vitro*, such as the work of James Freyer<sup>25-41</sup>, from which has naturally sprung models of tumor cell spheroids and effects on them of limited metabolites, excesses of toxins or metabolic by-products, and drug penetration and effectiveness, and thresholds of these characteristics at which tumor angiogenesis is stimulated<sup>42,43</sup>.

Hundreds of studies mention or include a modeling or mathematical analysis component in conjunction with an ovarian cancer study; ("ovarian cancer", 738 results);

of these, approximately 39 have a mathematical model described in the text. These models include the effects of transcriptional and regulatory networks<sup>18,19</sup>, long-term recurrence predictions and prognostic value of CA-125, a blood-borne cancer marker commonly utilized for ovarian cancer<sup>20-22</sup>, effectiveness of treatment (lymphadenectomy<sup>23</sup>), and survival rates of patients after surgical or drug treatment<sup>24</sup>.

Few spatially explicit models of ovarian cancer exist aside from our own<sup>12</sup>. Giverso *et al.*<sup>44</sup> built a 2-dimensional cellular Potts model of ovarian cancer that explores the interaction of ovarian cancer cells with the mesothelium (one-cell-deep lining of the peritoneal cavity) and extracellular matrix during invasion. More common are models of drug penetration in the peritoneal cavity. El-Kareh *et al.*<sup>45</sup> modeled the penetration distance of cisplatin into the rat peritoneum (the peritoneal cavity surface) with and without hyperthermia (application of heat). This model and others, as well as experimental efforts regarding penetration of tissues in the peritoneal cavity, have acknowledged absorption of small-molecule drugs by vessels as a major barrier to drug penetration<sup>46</sup>.

### **Modeling methods in drug delivery**

We implement drug modeling simplification guidelines outlined by Thurber *et al.*<sup>47</sup>, which recommend considering only the primary rate-limiting step for drug diffusion in tumor tissue, determined by the molecular weight, shape, and charge of a drug. For therapeutic antibodies, diffusion through the blood vessel wall is the rate-limiting step, as only a small percentage of antibody can permeate the vascular endothelium. For low-molecular-weight chemotherapeutics that easily penetrate the vascular wall and diffuse in

tissue, the rate-limiting factor is blood flow. As a further simplification, we do not consider blood flow to be limited in the model, since we are implicitly limiting flow in the low-vascular-density models. Therefore, aside from the limit of diffusion length in tumor tissues, no explicit barrier to small-molecule therapies is represented. For therapeutic antibodies, we represent the vascular endothelial barrier with the Biot number, the ratio between drug concentration in the vessel lumen and the vessel surface. The Biot number incorporates vessel permeability and vessel diameter, and is the ratio of extravasation rate to diffusion in tumor tissue for a typical antibody in a typical capillary<sup>46</sup>. Finally, although we initially assumed that diffusion of antibody from the IP fluid into the outside of a micrometastasis undergoes only passive diffusion into the tumor surface, while antibody coming from vessel is parameterized from *in vivo* effective penetration lengths that likely include convective velocity of the interstitial fluid, our experiments showed that the two diffusion rates are approximately the same ( $\sim 1.3 \text{ cm}^2/\text{s}$ ; see Results and Fig. 1). Therefore antibody diffuses at equal rates from peritoneal fluid and blood. Low-molecular-weight drugs also diffuse from the two compartments at equal rates.

### **The Cellular Potts Model as an agent-based model and cellular automaton**

The cellular Potts model is a lattice-based discrete model that simulates biological cells. It is derived from a series of models in physics, the most recent ancestor being the large-Q Potts model of non-biological adhesion-driven processes in which lowering surface energy over the whole model is the goal, as in the evolution of bubbles in foam<sup>48</sup>. The Glazier-Graner-Hogeweg cellular Potts model is then altered to use differential

adhesion between different cell types to recapitulate the spontaneous cell sorting seen in real systems of mixed cells as the surface energy decreases in the system, known as the Differential Adhesion Hypothesis<sup>48,49</sup>. It is therefore well suited to simulating systems in which adhesion between cells, or between cells and elements of their environment, is central to the system's function. The initial model was ideal for modeling systems of cell rearrangement<sup>48,49</sup>. However, the model was extended to allow additional cellular constraints, such as volume, surface area, length-width ratio, and polarity. Other extensions were added to the CompuCell3D software package<sup>50</sup>, such as the capacity for fluid flow and the maintenance of preserved compartments within cells<sup>51</sup>. The model is not suited to systems requiring advective diffusion, such as models where blood flow rate might change delivery of a chemical along the length of a vessel, or where<sup>51</sup> explicit convection is required to deliver a chemical (though convection can be implicit in the penetration length of the chemical). It is also too computationally expensive to run if individual cells in even a small piece of tissue must be modeled. Our simulations of tumors 0.75mm in diameter with 1 million cells and chemical diffusion processes take over a month to run on a standard processor. However, CompuCell3D developers are trying to increase the speed of simulations through parallelization and GPU (graphical processing unit) processing.

Cellular Potts is ideal for modeling the evolution of complex cellular-scale shapes in space, including body segmentation, as during embryonic development<sup>52</sup>, structures with branches such as human and plant vascular structures<sup>53,51</sup>, filamental structures such as strands of muscle<sup>54</sup>, and the formation of fluid-filled voids (in a cellular Potts model of vascular lumen formation with agent-based extensions<sup>55</sup>). It can also model ordered

movement of cellular populations, such as in the growth of biofilms<sup>56</sup>, bacterial swarming<sup>57</sup>, and the development of slime mold morphology<sup>58</sup>.

## **Dissertation Summary**

In Chapter 2, we use a cellular Potts model to examine spatial, temporal, morphological and adhesive dynamics of small tumor spheroids of seven cells. These tumor models employ cell growth, mitosis, adhesion, and chemotaxis during the processes of tumor growth, invasion, and angiogenesis.

Our questions in this chapter were whether we could use the cellular Potts model to recapitulate tumor morphology, tumor invasion, and tumor-initiated angiogenesis. By making intracellular adhesion in the tumor higher than tumor cells' adhesion to surrounding tissue, fluid, or matrix, we produce a spheroidal morphology similar to that of tumors protruding into the peritoneal cavity. We do not model invasive, "spongy" tumors. Parameterizing our model of invasion of a 7-cell spheroid into fatty tissue shows that a parameter to direct the cells toward vessels – a chemokine or other attractant or physical guide -- is missing. We use a theoretical chemical attractant of similar molecular weight to VEGF emanating from blood vessels in fatty tissue to complete the model. Finally, the angiogenesis model is not morphologically accurate, since the final vessel structure does not have well-defined vessels and is more of a convoluted surface, but it does generate a hypothesis for a chemical threshold of VEGF to initiate angiogenesis when the tumor spheroid is within 5 $\mu$ m of a vascular endothelial cell. Also, in attempting to generate the correct level of vascularity at the right time in the tumor's growth, given the growth rate of the endothelial sprouts, we realized that tumors were

initiating angiogenesis very early. This in turn caused us to examine our microarray data, which shows that the cells are constitutively expressing angiogenic factors.

In Chapter 3, we ask whether primary delivery of a drug by the IP or IV route results in higher accumulation of either pertuzumab or cisplatin. We also ask how the percent vascular area in the tumor (as measured in a tumor cross-section) affects IP and IV delivery of both drugs.

We use a cellular Potts model with frozen cells, functioning as a cellular automaton (with no spatially dynamic cellular agents, but synchronous updating of the cell states at each time step<sup>59</sup>), representing vessels, tumor, and peritoneal fluid to test the effects of variation in vascular density of tumors upon drug penetration. We use *effective penetration* from empirical studies in tumor spheroids and *in vivo* tumor studies to implicitly parameterize convection and molecular-scale barriers to penetration in tissue. We model the delivery of drugs and antibodies by intravenous injection (IV), or intraperitoneal (IP) (intra-abdominal) injection to tumors with 0 to 10% vascular area in the central plane, the range of vascular densities in tumors (n=18) found attached to the bowel and omentum in nine patients. We predict the effectiveness of IV or IP delivery, in combination with the molecular weight and correlated potential for penetration into the tumor tissue. Our models show that IP delivery results in better delivery of both cisplatin and pertuzumab to abdominally disseminated tumors, with the most marked improvement in avascular tumors. We also find that higher vascular area leads slower drug uptake and greater heterogeneity of drug accumulation.

In Chapter 4, we extend the delivery model by examining 3 models of vascular morphology in tumor tissue. We ask if drug accumulation varies with the distribution of

vascular vessel sizes, the vessel volume density, or with drug delivery (IP or IV). Additionally we ask whether these factors affect heterogeneity of drug accumulation across tumor cells.

We consider regions of tumor that are not within drug penetration distance from the intraperitoneal cavity. We change only *i.* the vascular morphology, and *ii.* the fact that no surface of the simulation domain receives intraperitoneal drug directly – only indirectly from the secondary drug concentration that appears in the blood, or directly from an intravenous injection. We then examine the levels of accumulation in the tumor cells, and measure heterogeneity of accumulation via the Shannon Entropy metric. We find that IP delivery gives sub-therapeutic levels of both drugs. IV delivery greatly improves accumulation of cisplatin, as well as the rate of accumulation of pertuzumab, though IP pertuzumab eventually plateaus close to the levels accumulated after IV delivery. Vascular volume affects the rate of delivery of pertuzumab, but not as dramatically as mode of delivery. Vascular volume does not affect cisplatin's accumulation. We also observe that Entropy, in combination with a histogram, is a good measure of both effectiveness and heterogeneity of drug delivery. These measures show that there is some moderate change with alterations in vessel diameter distributions. Finally, in the whole tumor for each vessel distribution, even during the best delivery scenario (IV), antibody accumulation is highly heterogeneous, and leaves behind a large sub-population of cells below the therapeutic threshold.



## References

1. Korolev KS, Xavier JB, Gore J. Turning ecology and evolution against cancer. *Nat Rev Cancer*. 2014;14(5):371–80. doi:10.1038/nrc3712.
2. Siegel R, Naishadham D, Jemal A. Cancer Statistics , 2012. *CA Cancer J Clin*. 2012;62:10–29. doi:10.3322/caac.20138. Available.
3. Howlader N, Noone AM, Krapcho M, Neyman N, Aminou R, Waldron W. SEER Cancer Statistics Review, 1975–2010, National Cancer Institute. Bethesda, MD, based on November 2012 SEER data submission, posted to the SEER web site, 2013. [http://seer.cancer.gov/csr/1975\\_2010](http://seer.cancer.gov/csr/1975_2010) (Accessed June 08, 2013). 2011.
4. Yale Early Detection Program For Ovarian Cancer. Available at: <http://medicine.yale.edu/obgyn/gynonc/services/detection.aspx>.
5. Badgwell D, Lu Z, Le K, Gao F, Yang M. The tumor-suppressor gene ARHI (DIRAS3) suppresses ovarian cancer cell migration through inhibition of the Stat3 and FAK/Rho signaling pathways. *Oncogene*. 2011. Available at: <http://www.nature.com/onc/journal/vaop/ncurrent/abs/onc2011213a.html>. Accessed September 30, 2011.
6. Pradeep S, Kim S, Wu S, et al. Hematogenous Metastasis of Ovarian Cancer: Rethinking Mode of Spread. *Cancer Cell*. 2014;26:77–91. doi:10.1016/j.ccr.2014.05.002.
7. Ahmed N, Stenvers KL. Getting to know ovarian cancer ascites: opportunities for targeted therapy-based translational research. *Front Oncol*. 2013;3:256. doi:10.3389/fonc.2013.00256.
8. Erickson BK, Conner MG, Landen CN. The role of the fallopian tube in the origin of ovarian cancer. *Am J Obstet Gynecol*. 2013;209(5):409–14. doi:10.1016/j.ajog.2013.04.019.
9. Krediet RT. *Nolph and Gokal's Textbook of Peritoneal Dialysis*. 2009:934. Available at: <http://books.google.com/books?hl=en&lr=&id=hSkN5rbg6o0C&pgis=1>. Accessed November 15, 2010.
10. Pascal J, Ashley CE, Wang Z, et al. Mechanistic Modeling Identifies Drug-Uptake History as Predictor of Tumor Drug Resistance and Nano-Carrier-Mediated Response. 2013;(Xx).
11. Petignat P, du Bois A, Bruchim I, Fink D, Provencher DM. Should intraperitoneal chemotherapy be considered as standard first-line treatment in advanced stage ovarian cancer? *Crit Rev Oncol Hematol*. 2007;62(2):137–47. doi:10.1016/j.critrevonc.2006.11.009.
12. Steinkamp M. Ovarian Tumor Attachment, Invasion, and Vascularization Reflect Unique Microenvironments in the Peritoneum: Insights from Xenograft and Mathematical Models. Available at: <http://www.ncbi.nlm.nih.gov/pmc/articles/PMC3656359/>.
13. Bellman R, Jacquez J, Kalaba R. Some mathematical aspects of chemotherapy: I. One-organ models. *Bull Math* .... 1960. Available at: <http://link.springer.com/article/10.1007/BF02478005>. Accessed March 22, 2015.

14. Jacquez J, Bellman R, Kalaba R. Some mathematical aspects of chemotherapy—II: The distribution of a drug in the body. *Bull Math ...*. 1960. Available at: <http://link.springer.com/article/10.1007/BF02478352>. Accessed March 22, 2015.
15. Ribba B, Colin T, Schnell S. A multiscale mathematical model of cancer, and its use in analyzing irradiation therapies. *Theor Biol Med Model*. 2006;3(1):7. doi:10.1186/1742-4682-3-7.
16. Gallo JM, Vicini P, Orlansky A, et al. Pharmacokinetic model-predicted anticancer drug concentrations in human tumors. *Clin Cancer Res*. 2004;10(23):8048–58. doi:10.1158/1078-0432.CCR-04-0822.
17. Sinek JP, Sanga S, Zheng X, Frieboes HB, Ferrari M, Cristini V. Predicting drug pharmacokinetics and effect in vascularized tumors using computer simulation. *J Math Biol*. 2009;58(4-5):485–510. doi:10.1007/s00285-008-0214-y.
18. Khalil HS, Goltsov A, Langdon SP, Harrison DJ, Bown J, Deeni Y. Quantitative analysis of NRF2 pathway reveals key elements of the regulatory circuits underlying antioxidant response and proliferation of ovarian cancer cells. *J Biotechnol*. 2014. doi:10.1016/j.jbiotec.2014.09.027.
19. Bilsland AE, Stevenson K, Liu Y, et al. Mathematical model of a telomerase transcriptional regulatory network developed by cell-based screening: analysis of inhibitor effects and telomerase expression mechanisms. *PLoS Comput Biol*. 2014;10(2):e1003448. doi:10.1371/journal.pcbi.1003448.
20. Wilboux M, Hénin E, Oza A, et al. Dynamic modeling in ovarian cancer: an original approach linking early changes in modeled longitudinal CA-125 kinetics and survival to help decisions in early drug development. *Gynecol Oncol*. 2014;133(3):460–6. doi:10.1016/j.ygyno.2014.04.003.
21. You B, Colomban O, Heywood M, et al. The strong prognostic value of KELIM, a model-based parameter from CA 125 kinetics in ovarian cancer: data from CALYPSO trial (a GINECO-GCIG study). *Gynecol Oncol*. 2013;130(2):289–94. doi:10.1016/j.ygyno.2013.05.013.
22. Hori SS, Gambhir SS. Mathematical model identifies blood biomarker-based early cancer detection strategies and limitations. *Sci Transl Med*. 2011;3(109):109ra116. doi:10.1126/scitranslmed.3003110.
23. Pereira A, Irishina N, Pérez-Medina T, et al. Defining the optimal lymphadenectomy cut-off value in epithelial ovarian cancer staging surgery utilizing a mathematical model of validation. *Eur J Surg Oncol*. 2013;39(3):290–6. doi:10.1016/j.ejso.2012.12.006.
24. Sigal BM, Munoz DF, Kurian AW, Plevritis SK. A simulation model to predict the impact of prophylactic surgery and screening on the life expectancy of BRCA1 and BRCA2 mutation carriers. *Cancer Epidemiol Biomarkers Prev*. 2012;21(7):1066–77. doi:10.1158/1055-9965.EPI-12-0149.
25. Freyer JP, Sutherland RM. Selective Dissociation and Characterization of Cells from Different Regions of Multicell Tumor Spheroids. *Cancer Res*. 1980;40(11):3956–3965. Available at: <http://cancerres.aacrjournals.org/cgi/content/abstract/40/11/3956>. Accessed July 9, 2012.
26. Freyer JP, Sutherland RM, Sutherland JPF. Regulation of Growth Saturation and Development of Necrosis in EMT6 / Ro Multicellular Spheroids by the

- Glucose and Oxygen Supply Regulation of Growth Saturation and Development of Necrosis in EMT6 / Ro Multicellular Spheroids by the Glucose and Oxygen. 1986:3504–3512.
27. Freyer JPJP, Sutherland RM. A Reduction in the In Situ Rates of Oxygen and Glucose Consumption of Cells in EMT6/Ro Spheroids During Growth. *J Cell Physiol.* 1985;124(3):516–24. doi:10.1002/jcp.1041240323.
  28. Freyer J, Schor P, Saponara A. Partial purification of a protein growth inhibitor from multicellular spheroids. *Biochem Biophys Res Commun.* 1988. Available at: <http://www.sciencedirect.com/science/article/pii/S0006291X88807368>. Accessed March 22, 2015.
  29. Freyer J, Schor P. Automated selective dissociation of cells from different regions of multicellular spheroids. *Vitr Cell Dev Biol.* 1989. Available at: <http://link.springer.com/article/10.1007/BF02624405>. Accessed March 22, 2015.
  30. Freyer J. Spheroids in radiobiology research. *Spheroid Cult cancer Res.* 1992. Available at: [https://scholar.google.com/scholar?q=james+freyer+spheroid&btnG=&hl=en&as\\_sdt=0%2C32#17](https://scholar.google.com/scholar?q=james+freyer+spheroid&btnG=&hl=en&as_sdt=0%2C32#17). Accessed March 22, 2015.
  31. Sillerud L, Freyer J. Proton NMR microscopy of multicellular tumor spheroid morphology. *Magn Reson Chem.* 1990. Available at: [http://www.researchgate.net/profile/Laurel\\_Sillerud/publication/21079359\\_Proton\\_NMR\\_microscopy\\_of\\_multicellular\\_tumor\\_spheroid\\_morphology/links/0c96052cb1a22d3836000000.pdf](http://www.researchgate.net/profile/Laurel_Sillerud/publication/21079359_Proton_NMR_microscopy_of_multicellular_tumor_spheroid_morphology/links/0c96052cb1a22d3836000000.pdf). Accessed March 22, 2015.
  32. LaRue K, Bradbury E, Freyer J. Differential regulation of cyclin-dependent kinase inhibitors in monolayer and spheroid cultures of tumorigenic and nontumorigenic fibroblasts. *Cancer Res.* 1998. Available at: <http://cancerres.aacrjournals.org/content/58/6/1305.short>. Accessed March 22, 2015.
  33. Freyer J, Schor P. Regrowth kinetics of cells from different regions of multicellular spheroids of four cell lines. *J Cell Physiol.* 1989. Available at: <http://onlinelibrary.wiley.com/doi/10.1002/jcp.1041380222/abstract>. Accessed March 22, 2015.
  34. Freyer J. Rates of oxygen consumption for proliferating and quiescent cells isolated from multicellular tumor spheroids. *Oxyg Transp to Tissue XV.* 1994. Available at: [http://link.springer.com/chapter/10.1007/978-1-4615-2468-7\\_44](http://link.springer.com/chapter/10.1007/978-1-4615-2468-7_44). Accessed March 22, 2015.
  35. Freyer J, Schor P, Jarrett K, Neeman M, Sillerud L. energetics measured by phosphorous nuclear magnetic resonance spectroscopy are not correlated with chronic nutrient deficiency in multicellular tumor spheroids. *Cancer Res.* 1991. Available at: <http://cancerres.aacrjournals.org/content/51/15/3831.short>. Accessed March 22, 2015.
  36. LaRue K, Khalil M, Freyer J. Microenvironmental regulation of proliferation in multicellular spheroids is mediated through differential expression of cyclin-dependent kinase inhibitors. *Cancer Res.* 2004. Available at: <http://cancerres.aacrjournals.org/content/64/5/1621.short>. Accessed March 22, 2015.

37. Freyer J, Sutherland R. Proliferative and clonogenic heterogeneity of cells from EMT6/Ro multicellular spheroids induced by the glucose and oxygen supply. *Cancer Res.* 1986. Available at: <http://cancerres.aacrjournals.org/content/46/7/3513.short>. Accessed March 22, 2015.
38. Freyer J. Role of necrosis in regulating the growth saturation of multicellular spheroids. *Cancer Res.* 1988. Available at: <http://cancerres.aacrjournals.org/content/48/9/2432.short>. Accessed March 22, 2015.
39. Freyer J, Sutherland R. Selective dissociation and characterization of cells from different regions of multicell tumor spheroids. *Cancer Res.* 1980. Available at: <http://cancerres.aacrjournals.org/content/40/11/3956.short>. Accessed March 22, 2015.
40. Casciari JJ, Sotirchos S V, Sutherland RM. Variations in tumor cell growth rates and metabolism with oxygen concentration, glucose concentration, and extracellular pH. *J Cell Physiol.* 1992;151(2):386–94. doi:10.1002/jcp.1041510220.
41. Stewart JB, Freyer C, Elson JL, Larsson N-G. Purifying selection of mtDNA and its implications for understanding evolution and mitochondrial disease. *Nat Rev Genet.* 2008. doi:10.1038/nrg2396.
42. Jiang Y, Pjesivac-Grbovic J, Cantrell C, Freyer JP. A multiscale model for avascular tumor growth. *Biophys J.* 2005;89(6):3884–94. doi:10.1529/biophysj.105.060640.
43. Loessner D, Little JP, Pettet GJ, Huttmacher DW. A multiscale road map of cancer spheroids - incorporating experimental and mathematical modelling to understand cancer progression. *J Cell Sci.* 2013;126(Pt 13):2761–71. doi:10.1242/jcs.123836.
44. Giverso C, Scianna M, Preziosi L, Buono N Lo, Funaro A. Individual Cell-Based Model for In-Vitro Mesothelial Invasion of Ovarian Cancer. ... *Model Nat* .... Available at: [http://journals.cambridge.org/abstract\\_S0973534810051096](http://journals.cambridge.org/abstract_S0973534810051096). Accessed October 21, 2011.
45. El-Kareh AW, Secomb TW. A theoretical model for intraperitoneal delivery of cisplatin and the effect of hyperthermia on drug penetration distance. *Neoplasia.* 2004;6(2):117–27. doi:10.1593/neo.03205.
46. Thurber GM, Schmidt MM, Wittrup KD. Antibody tumor penetration: transport opposed by systemic and antigen-mediated clearance. *Adv Drug Deliv Rev.* 2008;60(12):1421–34. doi:10.1016/j.addr.2008.04.012.
47. Thurber GM, Weissleder R. A systems approach for tumor pharmacokinetics. Boswell CA, ed. *PLoS One.* 2011;6(9):e24696. doi:10.1371/journal.pone.0024696.
48. Graner F, Glazier J. Simulation of biological cell sorting using a two-dimensional extended Potts model. *Phys Rev Lett.* 1992. Available at: <http://link.aps.org/doi/10.1103/PhysRevLett.69.2013>. Accessed April 15, 2013.
49. Glazier J, Graner F. Simulation of the differential adhesion driven rearrangement of biological cells. *Phys Rev E.* 1993;47(3):2128–2154. doi:10.1103/PhysRevE.47.2128.

50. Swat MH, Thomas GL, Belmonte JM, Shirinifard A, Hmeljak D, Glazier JA. Multi-scale modeling of tissues using CompuCell3D. *Methods Cell Biol.* 2012;110:325–66. doi:10.1016/B978-0-12-388403-9.00013-8.
51. Balter A, Merks R, Popławski N. The Glazier-Graner-Hogeweg model: extensions, future directions, and opportunities for further study. *Single-Cell-Based ....* 2007. Available at: [http://link.springer.com/chapter/10.1007/978-3-7643-8123-3\\_7](http://link.springer.com/chapter/10.1007/978-3-7643-8123-3_7). Accessed March 22, 2015.
52. Vroomans RMA, Hogeweg P, Ten Tusscher KHWJ. Segment-specific adhesion as a driver of convergent extension. *PLoS Comput Biol.* 2015;11(2):e1004092. doi:10.1371/journal.pcbi.1004092.
53. Daub J. A cell-based model of extracellular-matrix-guided endothelial cell migration during angiogenesis. 2010. Available at: <http://oai.cwi.nl/oai/asset/17513/17513B.pdf>. Accessed August 7, 2012.
54. Boer B de. Integrating multi-scale knowledge on cardiac development into a computational model of ventricular trabeculation. ... *Syst Biol ....* 2014. Available at: <http://onlinelibrary.wiley.com/doi/10.1002/wsbm.1285/full>. Accessed March 22, 2015.
55. Boas SEM, Palm MM, Koolwijk P, Merks RMH. Computational modeling of angiogenesis: towards a multi-scale understanding of cell-cell and cell-matrix interactions. :1–23. Available at: <http://oai.cwi.nl/oai/asset/18954/18954B.pdf>. Accessed February 18, 2012.
56. Poplawski N. Simulation of single-species bacterial-biofilm growth using the Glazier-Graner-Hogeweg model and the CompuCell3D modeling environment. *Math ....* 2008. Available at: [https://scholar.google.com/scholar?q=poplawski+biofilm&btnG=&hl=en&as\\_sdt=0%2C32#0](https://scholar.google.com/scholar?q=poplawski+biofilm&btnG=&hl=en&as_sdt=0%2C32#0). Accessed March 22, 2015.
57. Starruß J, Peruani F, Bär M, Deutsch A. Bacterial Swarming Driven by Rod Shape. *Math Model ....* 2007. Available at: [http://link.springer.com/chapter/10.1007/978-0-8176-4558-8\\_14](http://link.springer.com/chapter/10.1007/978-0-8176-4558-8_14). Accessed March 22, 2015.
58. Marée AF, Hogeweg P. How amoeboids self-organize into a fruiting body: multicellular coordination in Dictyostelium discoideum. *Proc Natl Acad Sci U S A.* 2001;98(7):3879–83. doi:10.1073/pnas.061535198.
59. Chavali AK, Gianchandani EP, Tung KS, Lawrence MB, Peirce SM, Papin J a. Characterizing emergent properties of immunological systems with multi-cellular rule-based computational modeling. *Trends Immunol.* 2008;29(12):589–99. doi:10.1016/j.it.2008.08.006.

## **Chapter 2: Ovarian tumor attachment, invasion and vascularization reflect unique microenvironments in the peritoneum: insights from xenograft and mathematical models**

### **ABSTRACT**

Ovarian cancer relapse is often characterized by metastatic spread throughout the peritoneal cavity with tumors attached to multiple organs. In this study, interaction of ovarian tumor cells with the peritoneal tumor microenvironment was evaluated in a xenograft model based on intraperitoneal injection of fluorescent SKOV3.ip1 ovarian cancer cells. Intra-vital microscopy of mixed GFP-RFP cell populations injected into the peritoneum demonstrated that tumor cells aggregate and attach as mixed spheroids, emphasizing the importance of homotypic adhesion in tumor formation. Electron microscopy provided high resolution structural information about local attachment sites. Experimental measurements from the mouse model were used to build a three-dimensional cellular Potts ovarian tumor model (OvTM) that examines ovarian tumor cell attachment, chemotaxis, growth and vascularization. OvTM simulations provide insight into the relative influence of tumor cell-cell adhesion, oxygen availability, and local architecture on tumor growth and morphology. Notably, tumors on the mesentery, omentum or spleen readily invade the “open” architecture, while tumors attached to the gut encounter barriers that restrict invasion and instead rapidly expand into the peritoneal space. Simulations suggest that rapid neovascularization of SKOV3.ip1 tumors is

triggered by constitutive release of angiogenic factors in the absence of hypoxia. This research highlights the importance of cellular adhesion and tumor microenvironment in the seeding of secondary ovarian tumors on diverse organs within the peritoneal cavity. Results of the OvTM simulations indicate that invasion is strongly influenced by features underlying the mesothelial lining at different sites, but is also affected by local production of chemotactic factors. The integrated *in vivo* mouse model and computer simulations provide a unique platform for evaluating targeted therapies for ovarian cancer relapse. This chapter was co-authored by Mara Steinkamp, Kimberly Kanigel Winner, Suzy Davies, Carolyn Muller, Yong Zhang, Robert M. Hoffman, Abbas Shirinifard, Melanie Moses, Yi Jiang and Bridget S. Wilson. It was published in *Frontiers in Oncology*, Volume 3, 2013, page 97. Copyright ©2013 Steinkamp, Winner, Davies, Muller, Zhang, Hoffman, Shirinifard, Moses, Jiang and Wilson.

## **INTRODUCTION**

Ovarian cancer is often detected at a late stage of disease after the cancer has locally disseminated to the peritoneum. Visible tumors are surgically removed and residual microscopic disease is targeted with chemotherapy. However, 90% of patients who originally respond to treatment will relapse with chemotherapy-resistant disease [McGuire, 1996]. Relapse is thought to occur because residual cancer cells aggregate in the peritoneal fluid and form microscopic tumor spheroids that are more resistant to chemotherapy [Shield, 2009]. These spheroids can then adhere to the surface of organs

in the peritoneum and seed new tumors, encouraged by chemokines and growth factors within the peritoneal fluid [Milliken et al., 2002;Bast et al., 2009].

A common feature of the peritoneal environment is the mesothelial lining that tumor cells must sequentially bind to [Strobel and Cannistra, 1999;Casey et al., 2001;Kenny et al., 2008] and penetrate [Burlison et al., 2006;Iwanicki et al., 2011] in order to adhere to underlying tissues. Recent *in vitro* studies suggest that this penetration step can occur within a few hours after spheroid attachment [Iwanicki et al., 2011]. Nevertheless, unique features associated with different organs clearly influence progression in this disease. For example, ovarian cancer cells preferentially colonize the omentum, a fatty tissue that has pockets of resident immune cells referred to as “milky spots” and easily accessible blood vessels [Gerber et al., 2006;Khan et al., 2010;Nieman et al., 2011]. Tumor cells also colonize other organs in the peritoneum, with distinct growth rates and morphology depending on the site. It is reasonable to expect that these heterogeneous tumor populations will respond differently to treatment, motivating further investigation into the features of the microenvironment that govern these differences.

To establish a mouse model of ovarian cancer relapse, SKOV3.ip1 cells expressing fluorescent proteins (GFP, RFP) were injected into the peritoneum of nude mice and the resulting tumors growing on the omentum, intestine, mesentery and spleen were imaged. Excised tumors were processed for both transmission and light microscopy, providing detailed information about the cellular environment and vascularization patterns.



The distinct features in tumor morphology at different sites led us to consider the potential contributions of local chemotactic factors, oxygenation and adhesion through mathematical modeling. In recent years, mathematical models have moved beyond the generic models of tumor growth and development e.g., [Jiang et al., 2005;Shirinifard et al., 2009;Morton et al., 2011;Giverso and Preziosi, 2012] and are now able to realistically model cancers, e.g. breast cancer [Chauviere et al., 2010;Macklin et al., 2012] and colon cancer [Rejniak and McCawley, 2010]. Few have addressed the unique features of ovarian cancer. Arakelyan et al. (2005) modeled ovarian tumor growth response to the dynamics of vascular density and vessel size [Arakelyan et al., 2005]. Giverso et al. (2010) developed a two-dimensional model of early ovarian tumor spheroid invasion through the mesothelium and underlying extracellular matrix [Giverso et al., 2010]. In this work, our focus is on understanding the distinct features of tumor morphology at different sites in ovarian cancer relapse in three dimensions. The cellular Potts model framework was chosen because of its previous successes in studying similar problems in tumor growth and angiogenesis [Jiang et al., 2005;Shirinifard et al., 2009]. Our cell-based and geometrically-realistic ovarian tumor computer model, OvTM, takes into account characteristics of the peritoneal microenvironment and provides insight into the earliest steps in spheroid attachment, invasion and vascularization within the peritoneum. In particular, homotypic and heterotypic adhesion observed between SKOV3.ip1 xenograft tumor cells and the niche tissue structure are the starting point of OvTM. We applied the model to explore the roles of cell adhesion, cell migration and proliferation as influenced by the microenvironment at two sites and were able to reproduce experimental observations. The ultimate goal of our model is a realistic representation of spheroid

growth, whose dimensions and morphology qualitatively resemble the tumors disseminated in different tissue niches in the peritoneal cavity in our mouse xenografts. Such a model can be further developed to include short-term drug delivery after debulking surgery, allowing the evaluation of local drug responsiveness.

## **MATERIALS AND METHODS**

### **Cell culture and cell lines**

SKOV3ip.1 parental cells and GFP-stable transfectants were kind gifts of Laurie Hudson and Angela Wandinger-Ness (UNM). This aggressive line was passaged through a nude mouse [Yu et al., 1993]. Cells were maintained in RPMI media supplemented with 5% heat-inactivated FBS, 1% L-glutamine, 1% sodium pyruvate and 0.5% penicillin/streptomycin (Invitrogen, Grand Island, NY). SKOV3.ip1-GFP cells were treated with 250  $\mu$ g/ml Hygromycin to maintain GFP expression. To create red fluorescent protein (RFP)-expressing SKOV3.ip1 cells, parental cells were transfected with pTagRFP-N vector (Axxora, San Diego, CA) using Lipofectamine LTX reagent (Invitrogen). Stably fluorescent cells were selected with geneticin sulfate (Invitrogen) for one week. Transfectants were sorted for high fluorescence using a Beckman Coulter Legacy MoFlo cell sorter (UNM Flow Cytometry Core Facility).

### **Intraperitoneal mouse model of ovarian cancer relapse**

All mouse procedures were approved by the University of New Mexico Animal Care and Use Committee, in accordance with NIH guidelines for the Care and Use of Experimental Animals.

Nu/nu nude mice (NCI) or nude mice ubiquitously expressing RFP [Yang et al., 2009] were engrafted by intraperitoneal injection with 100  $\mu$ l of a single cell suspension containing five million SKOV3.ip1 cells expressing GFP. Tumor adhesion and invasion was assessed at four days and two weeks post-injection. For low magnification assessment of total tumor burden, eight nude mice were imaged using a Pan-A-See-Ya Panoramic Imaging System (Lighttools, Inc., Encinitas, CA) two or three weeks post-injection of SKOV3.ip GFP cells. For high resolution images (up to 16X, single cell resolution), mice were imaged on the OV100 Olympus whole mouse imaging system (Olympus Corp., Tokyo, Japan) at AntiCancer, Inc., San Diego, CA, as previously reported [Yamauchi et al., 2006].

Where described, sections of intestine and attached mesentery with tumors were excised and fixed in zinc fixative for 30 minutes [Howdieshell et al., 2011]. Samples were mounted on glass slides with ProLong Gold mounting media (Invitrogen). GFP fluorescence and brightfield images were collected on a Nikon TE2000 Microscope (UNM Microscopy Core Facility) using an Axiocam digital color camera and SlideBook Image Acquisition software.

### **Co-injection experiments**

SKOV3.ip1-GFP cells and SKOV3.ip1-RFP cells ( $2.5 \times 10^6$  each population) were harvested from culture by trypsinization and mixed together as a single cell suspension immediately before injecting a total of five million cells into the peritoneum of three nude mice. For consecutive injections, 2.5 million SKOV3.ip1 GFP cells were injected IP into

three nude mice followed by injection of 2.5 million SKOV3.ip1 RFP cells a week later. The mice were sacrificed at the end of week 2 and tumors were imaged on the OV100.

### **Histology and immunofluorescence**

Mouse tumors were fixed in formalin or zinc fixative, embedded in paraffin, sectioned and hematoxylin/eosin (H & E) stained by TriCore (Albuquerque, NM) or processed for immunofluorescence using anti-CD31 antibodies (BD Biosciences, San Jose, CA). Images were acquired on a Zeiss AxioSkop or LSM500 confocal microscopes. The area of mesenteric tumors was determined by analysis of images from H&E-stained sections using ImageJ [Schneider et al., 2012]. The cross-sectional tumor area corresponding to the hypoxic threshold was calculated to be  $<104,000 \mu\text{m}^2$  based on the diameter of the spheroid in Figure 7B (364  $\mu\text{m}$ ).

### **Transmission electron microscopy**

Tissue was collected and fixed in 2% glutaraldehyde, post-fixed with osmium tetroxide, dehydrated in ascending alcohols and embedded in Epon. Ultrathin sections were stained and imaged on a Hitachi H600 transmission electron microscope (TEM). To identify SKOV3.ip1 cells present in tissue samples, their characteristic nuclear ultrastructure was determined from high magnification TEM images taken of SKOV3.ip1 GFP cells grown as 5,000 cell spheroids in a U-bottom Lipidure-coated 96-well plate (NOF America, Irvine, CA) for 48 hours.

### **The Ovarian Tumor Model (OvTM)**

We based our model on the following set of major assumptions that are inspired by the biology and empirical data.

1. The 3-D tissues we model consist of ovarian tumor (SKOV3.ip1), mesothelial, adipocyte, endothelial and smooth muscle cells, as well as extracellular matrix fibers and peritoneal fluid.
2. Adhesion strengths between various cell types are prescribed and remain constant. E.g., adhesion between SKOV3.ip1 cells is stronger than between SKOV3.ip1 and mesothelial cells.
3. The chemical environment consists of oxygen, tumor-secreted VEGF, adipocyte-secreted IL-8 [Nieman et al., 2011], and another unidentified growth factor (Growth Factor 2) secreted by blood vessels.
4. Both IL-8 and Growth Factor 2 are chemoattractants for tumor cells. VEGF is a chemoattractant for endothelial cells. Chemotaxis speed is proportional to the chemical gradient.
5. Cells consume oxygen supplied by the peritoneal fluid and blood vessels. When oxygen levels are below a threshold value (20 mmHg), tumor cells become hypoxic and stop growing. They resume proliferation if oxygen rises above the threshold level.
6. Cells are required to approximately double in volume before dividing and their division times have a Gaussian distribution.
7. OvTM does not represent the flow of peritoneal fluid (or ascites). Because the diffusion process for all chemicals considered in our study is much faster than the cellular processes under consideration, chemicals are well-mixed. Therefore, it is reasonable to omit convective delivery of chemicals in this model.

8. Cells can become immobilized if we impose shape constraints. Addition of a surface area constraint as well as a high volume constraint can make cells insensitive to changes in adhesion and to low chemotaxis constants. Adhesion parameter sensitivity analysis was therefore conducted without a surface area constraint on the cells. This constraint was added after adhesion optimization to produce cells that were more spheroidal, as they are seen *in vivo*.

The three-dimensional (3-D) ovarian tumor growth and invasion model, OvTM, is based on the cellular Potts model framework using CompuCell3D (Cickovski et al., 2007; Swat et al., 2009). Ovarian cancer cells growing in the peritoneum were simulated using parameters obtained from the mouse model and from published data. Parameters for the SKOV3.ip1 cells, endothelial cells, oxygen, growth factors, and measurements of mouse peritoneal tissue are shown in Table 1.

In the OvTM, five cell types are considered: ovarian tumor (SKOV3.ip1), mesothelial, adipocyte, endothelial and smooth muscle. Extracellular matrix fibers and peritoneal fluid are represented as special types. This cell-based model describes cell growth, division, death, and chemotactic migration within a 3-D tissue environment that mimics the specific organ site.

Cells are domains on a three-dimensional lattice. Each cell has an ID number,  $S$ , on each lattice site  $i$  of the cell domain, and an associated cell type  $\square$ . Cell-cell and cell-environment interactions are specified by an “*effective energy*”:

$$H = \sum_{i,j} J_{\tau(S_i),\tau(S_j)} [1 - \delta(S_i, S_j)] + \sum_S \lambda [V(S) - V^t(S)]^2 + \sum_i \mu C_i \quad (1)$$

The parameter  $J$  describes the cell-type-dependent adhesion. Adhesion coefficients ( $J$ ) for the cell types in each model are listed in Tables 2 and 3. The Kronecker delta function  $\delta$  ensures no energy is within cells where ID numbers are the same, limiting adhesion to cell boundaries. A cell's volume  $V$  is elastically constrained to  $V^t$ , the target cell volume;  $V^t$  is constant for the tissue cells, but is set to increase linearly for proliferating cells.  $\mu$  is the chemical potential describing the strength of chemotaxis, and  $C$  is the chemical concentration at the cell. This term applies to tumor and endothelial cells when their respective chemoattractant signals are above threshold activation values.

A modified Metropolis algorithm was used to simulate cell dynamics. A cell boundary lattice site is selected at random; the cell number,  $S$ , is copied to an unlike neighbor site  $S'$  (selected at random). This copying corresponds to the cell  $S$  protruding a unit volume into the neighboring cell  $S'$ . The difference between the effective energies before and after the protrusion event,  $E$ , determines if this copying event will be accepted. If the energy decreases, the protrusion is accepted; if it increases, the protrusion is accepted with a Boltzmann probability,  $\exp(-E/T)$ . The effective temperature,  $T$ , describes the amplitude of cytoskeletal fluctuation (Mombach et al., 1995). By such microscopic membrane protrusion and retraction, the cells perform biased random walks, and rearrange themselves, within the constraints of their volumes and chemical guidance.

***Chemical dynamics.*** Chemical dynamics are evaluated through continuous diffusion equations and are considered well-mixed in the peritoneal fluid. Chemicals acting as

chemoattractants to SKOV3-ip are: adipocyte-secreted IL-8 (Nieman et al., 2011), and an unidentified growth-factor secreted from the vessel (Growth Factor 2). The chemoattractant for endothelial cells during angiogenesis is VEGF. A system of partial differential equations describes the chemical dynamics, including diffusion through tissues, growth factor decay, glucose and oxygen consumption, and cell-uptake of signal molecules.

$$\frac{\partial C_1}{\partial t} = D_{C_1} \nabla^2 C_1 - \rho_{C_1} C_1 + \alpha_{C_1} \delta(\tau(S), adipocyte) \quad (2)$$

$$\frac{\partial C_2}{\partial t} = D_{C_2} \nabla^2 C_2 - \kappa_{C_2} C_2 + \alpha_{C_2} \delta(\tau(S), vessel) \quad (3)$$

$$\frac{\partial V}{\partial t} = D_V \nabla^2 V - \gamma_V V + \alpha_V \delta(\tau(S), tumor) \quad (4)$$

where  $C_1$  is IL-8,  $C_2$  is Growth Factor 2, and  $V$  is VEGF. These equations describe diffusion through tissue, decay, receptor binding/internalization by tumor cells, and production by source cells.

Oxygen is delivered by the vessel (see Figure 7) and diffuses from the peritoneal fluid. Its level is kept constant within the peritoneum. Diffusion of  $O_2$  through tissue and its consumption by the cells is described as:

$$\frac{\partial O_2}{\partial t} = D_{O_2} \nabla^2 O_2 - \epsilon \delta(\tau(S), tumor) \quad (5)$$

Depending on the availability of oxygen in their surrounding environment, tumor cells have the potential to be proliferating, quiescent or necrotic. Although the capability for tumor cells to become hypoxic or necrotic was integrated into the model, the spheroids



we simulated were too small in diameter to develop internal hypoxia under normal physiological conditions, and never became hypoxic or necrotic.

The secretion rates for IL-8, VEGF, and Chemotactic Factor 2 were taken from quantitative experiments (or estimated for Chemotactic Factor 2). Oxygen was kept constant at the simulation boundaries with the value corresponding to the steady state oxygen level in the mouse peritoneal fluid (~98.5 mmHg). Background IL-8 was also kept constant at the z boundaries, defined as normal to the mesothelium surface, with the value corresponding to its steady state concentration in the peritoneal fluid. IL-8 concentration at the x and y boundaries was constant at levels diffusing from the adipocytes. Boundary values of VEGF and Chemotactic Factor 2 were set to steady-state at 0, as background values were unknown and the cells generated small, concentrated fields that reached approximately 0 at the distance of the simulation boundaries. For the diffusion rates of these four chemicals ( $D > 15 \mu\text{m}^2/\text{min}$ ), CompuCell3d cannot generate boundary conditions for tissues or cell types, as the necessary solver requires extra solutions per time step that make running models intractably slow (*e.g.* ~525,000 extra solutions per time step are required in the case of oxygen, resulting in ~24 hours simulation time/1 minute experimental time simulated). All parameters are listed in Table 1.

The chemotaxis constant for SKOV3.ip1 cell response to IL-8 was increased until the cells were moving through the IL-8 gradient in mesenteric fat tissue at a rate we derived from the ovarian cancer spheroid experiments by Iwanicki *et al* (Iwanicki et al., 2011). Chemotaxis by tumor cells to Chemotactic Factor 2 coming from the vessel was tuned to

have the same order of magnitude of response as to IL-8 (order of magnitude (IL-8 concentration \* chemotaxis constant) = order of magnitude (Chemotactic Factor 2 concentration \* chemotaxis constant), where the chemotaxis constant =  $1 \times 10^{13}$ ).

***Cell reproduction.*** In OvTM, the cellular level model and the chemical environment model are integrated through the choice of a common time-scale. In the cellular Potts model, each Monte Carlo Step (MCS) corresponds to as many cellular protrusion events as the number of lattice sites in the simulation domain. We define one MCS to correspond to one minute of real time. The chemical equations (Eqn 2, 3, and 4) are solved at the time step of 1 minute, when the cell lattice configuration and states are assumed constant. The cells update their states according to their local chemical concentrations. The cell lattice is then updated for 1 MCS assuming chemicals stay constant. Such iterative feedback and update links the discrete cellular Potts model and the continuous chemical equations together. Each cell has its own division time and age clock. Division time for cells is set on a Gaussian distribution; SKOV3.ip1 cells divide between 24.5 and 26.5 hours and endothelial cells divide between 23 and 25 hours. A cell divides when two conditions are satisfied: a) the cell's age is greater than or equal to its division time, and b) the cell's volume is greater than or equal to its target volume, which increases linearly with the cell's age. When the cell ( $S$ ) divides, it is halved into two daughter cells,  $S$  and  $S'$ .

***Tissue Microenvironments.*** The three OvTM model scenarios each represent several cubic millimeters of peritoneal space, about one third of which is tissue. (The invasion model is  $7.6 \text{ mm}^3$  and contains  $2.6 \text{ mm}^3$  of tissue.) The rest of the volume is filled with

peritoneal fluid present in the mammalian peritoneal cavity. Cell shapes and sizes were determined by cell morphometry studies of normal mice, nude mice, and SKOV3.ip1 xenografts. Thickness of the adipose layer surrounding vessels of the mesentery was taken from the literature. Tissue rigidity in smooth muscle and adipocytes was estimated based on cell junctions and spacing from EM images of mouse tissues. The depth of penetration of SKOV3.ip1 cells on both tissue types was based upon xenograft tumors in our microscopic images.

The tissue microenvironments we considered were the outer surface of the intestine (Figures 2 and 7) and the mesentery (Figure 5). A layer of mesothelium covers both surfaces. Both environments are initialized with a tumor spheroid of seven cells contacting the center of the contiguous mesothelial surface in the peritoneal cavity.

On the intestine, smooth muscle lies beneath the mesothelium, separated from it by a thin layer of extra-cellular matrix (ECM). Ovarian cancer cells can push aside the mesothelium and degrade ECM (Kenny et al., 2008; Sodek et al., 2008), but strong adhesion between the muscle cells prevents further invasion. Scattered blood vessels lie just below the mesothelium. In our model, initiation of angiogenesis was triggered by a threshold VEGF level. When the local VEGF concentration exceeds a threshold, endothelial cells lining the blood vessels begin to proliferate and migrate, organizing into vascular sprouts.

Tumors on the omentum or mesentery can invade through the mesothelium and migrate through the loose matrix and adipocyte fields below. On the mesentery, ovarian cancer

cells adhering to the mesothelium push past the mesothelial cells as chemotactic gradients originating from adipocytes and vasculature stimulate migration into the tissue.

Both models are initialized with a tumor spheroid of seven cells contacting the center of the contiguous mesothelial surface in the peritoneal cavity. We assume ECM degradation rate by SKOV3.ip1 tip cells at the invading front is the same as the degradation rate by endothelial cells at the sprout tip (Bauer et al., 2009).

The process of angiogenesis is driven by endothelial cell chemotaxis toward VEGF, and by differential adhesive interactions between endothelial sprout cells and tumor cells. This simple model suggests that, to produce vasculature morphology similar to that in very small xenograft tumors, latent endothelial cells must become proliferating endothelial cells and initiate angiogenic behavior as soon as the spheroid comes within diffusion distance for low concentrations of VEGF of the vessel. Given VEGF production of  $3.82 \times 10^{-7}$  pg/min/SKOV3.ip1 cell, the threshold for the switch from latent to sprouting endothelial cells is set at  $2.08 \times 10^{-8}$  pg/cell volume, which initiates angiogenesis when the spheroid is about 5 microns from the vessel.

Exploration of adhesion parameters: To reproduce the morphology of *in vivo* SKOV3.ip1 xenografts on the intestine, we tested four combinations of homotypic and heterotypic adhesion parameters (Table 3). Only when tumors were parameterized to have high homotypic adhesion between tumor cells along with low heterotypic adhesion between tumor cells and components of the microenvironment (peritoneal fluid, extracellular matrix, visceral mesothelium and smooth muscle cells) did tumor cells form rounded spheroids similar to those seen *in vivo*. A surface area constraint was also imposed on the

tumor cells to maintain cell integrity. We ran at least five replica simulations for each parameter set, and observed no qualitative differences, within small variations, in our results.

**Table 1. OvTM parameters.** Values were obtained from direct measurement (indicated by ‘m’) of tissues and tumors or from previously published work. Where experimental values were not available, values were estimated for the model (indicated by ‘e’).

Chemical fields	Value	Units	Source
O <sub>2</sub> concentration (blood and peritoneal fluid)	98.5	mm Hg	(Shirasawa et al., 2003;Kizaka-Kondoh et al., 2009)
O <sub>2</sub> diffusion (D <sub>O2</sub> )	84,000	μm <sup>2</sup> /min	(Macdougall and McCabe, 1967)
VEGF diffusion (D <sub>V</sub> )	600	μm <sup>2</sup> /min	(Serini et al., 2003;Bauer et al., 2009)
VEGF decay (γ <sub>V</sub> )	0.01083	/min	(Serini et al., 2003;Bauer et al., 2009)
VEGF secretion: normoxic tumor cell (α <sub>V</sub> )	3.82 x 10 <sup>-7</sup>	pg/min/cell	(Huang et al., 2000)
Chemotactic Factor 2 diffusion (D <sub>C2</sub> )	700	μm <sup>2</sup> /min	e (Serini et al., 2003;Bauer et al., 2009)
Chemotactic Factor 2 decay (κ <sub>C2</sub> )	0.01083	/min	e (Serini et al., 2003;Bauer et al., 2009)
Chemotactic Factor 2 secretion (α <sub>C2</sub> )	1.8 x 10 <sup>-4</sup>	pg/min/cell	e (Serini et al., 2003;Bauer et al., 2009)
IL-8 diffusion (D <sub>C1</sub> )	15000	μm <sup>2</sup> /min	(Li Jeon et al., 2002)
IL-8 decay (equal to VEGF) (ρ <sub>C1</sub> )	0.01083	/min	e as in (Jain et al., 2008)

**Table 1 continued. OvTM parameters.**

IL-8 secretion by visceral adipocyte ( $\alpha_{C1}$ )	$2.2 \times 10^{-4}$	pg/min/cell	(Bruun et al., 2004)
IL-8 background concentration (peritoneal fluid)	1.732	pg/ml	(Barcz et al., 2002)
<b>Metabolic Parameters</b>	<b>Value</b>	<b>Units</b>	<b>Source</b>
O <sub>2</sub> consumption: proliferating tumor cell ( $\epsilon$ )	4.93	fmoles/min/cell	(Freyer and Sutherland, 1985; Casciari et al., 1992) (Höckel and Vaupel, 2001; Evans et al., 2006; Shirinifard et al., 2009)
O <sub>2</sub> threshold for hypoxia and VEGF production	19	mm Hg	
VEGF activation threshold for angiogenesis	0.0001	pg/cell volume	e
VEGF deactivation threshold for angiogenesis	0.00002	pg/cell volume	e
Average distance between adipocytes in the mesentery	0.2	$\mu\text{m}$	M
<b>Rate Parameters</b>	<b>Value</b>	<b>Units</b>	<b>Source</b>
SKOV3.ip1 invasion speed	10	$\mu\text{m/hr}$	e from (Iwanicki et al., 2011)
Rate of ECM degradation	0.55	$\mu\text{m}^2/\text{min}$	(Bauer et al., 2009)
SKOV3.ip1 cell cycle duration	25.5 +/- 1	hours	m
Vascular endothelial cell cycle duration	24 +/- 1	hours	(Ausprunk and Folkman, 1977; Levine et al., 2001; Bagley et al., 2003)
Cell volume after division	96 +/- 17	%	e from m

**Table 1 continued. OvTM parameters.**

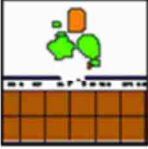
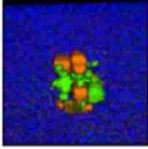
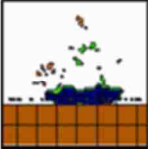
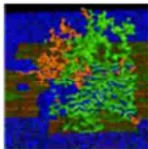
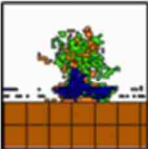
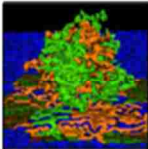
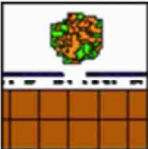
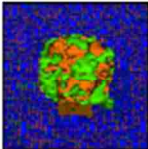
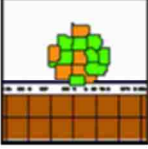
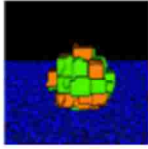
Morphometric Parameters	Value	Units	Source
Tumor cell radius	3.50	μm	M
Average adipocyte cell radius	10.1	μm	M
ECM (extracellular matrix) thickness	2	μm	M
ECM collagen fiber radius	1	μm	M
ECM collagen fiber length	20	μm	E
Vascular endothelial cell diameter (initial size)	10	μm	(Bauer et al., 2009)
Height of mesothelial cell on mesentery	0.44 – 2.5	μm	m, (Khanna and Krediet, 2009)

**Table 2. Combined tension and adhesion matrix for OvTM simulations of spheroid invasion, growth and angiogenesis.** White boxes show adhesion coefficients between cell types ( $J_{ij}$ ) and green boxes show adhesion coefficients between cells of the same type ( $J_{ii}$ ). Grey boxes show the surface tension values between cell types. Surface tension is defined as  $ST_{ij} = J_{ij} - (J_{ii} + J_{jj})/2$  (Glazier, Graner, 1993). Negative  $ST_{ij}$  signifies attraction, and positive  $ST_{ij}$  signifies repulsion. Surface tension = 0 for all  $ST_{ii}$ , but homotypic adhesion  $J_{ii}$  can still be strong. Maximum adhesion is 0. Mesenteric invasion models contain peritoneal fluid (PF), visceral mesothelium (VM), proliferating tumor cells (PTC), vessel wall endothelial cells (VW), adipocytes (A), and extracellular matrix (ECM). Included in the spheroid growth model are: proliferating tumor cell (PTC), peritoneal fluid (PF), visceral mesothelium (VM), vessel wall endothelial cells (VW), extracellular matrix (ECM), and smooth muscle (SM). Models with angiogenesis further include vessel wall endothelial cells (VW) and sprouting endothelial cells (SE).

	PF	VM	PTC	SE	VW	A	ECM	SM
PF	0	10	10	10	10	10	10	10
VM	10	0	20	20	10	20	0	10
PTC	10	20	0	0	0	3	3	0
SE	9.5	19.5	-0.5	1	0	13	5.5	2.5
VW	10	10	0	0	0	13	0	0
A	3.5	13.5	-3.5	6.5	6.5	13	1	0
ECM	9.5	-0.5	2.5	0.5	-0.5	0.5	1	0
SM	10	10	0	2.5	0	0	0	0



**Table 3. Exploration of adhesion parameters in spheroids attached to the surface of the small intestine.** Abbreviations are the same as in Table 2.

Parameters tested	Results	Spheroid images	
		2-D (tumor center)	3-D
<p>Low homotypic adhesion and low heterotypic adhesion to non-tumor cells</p> <p>Cell type 1    Cell type 2    Adhesion 1 ↔ 2                      PTC            PTC            20                      PTC            other           20                      other = PF, ECM, VM, and SM</p>	By 24 h, tumor cells show reduced volume and the spheroid is no longer cohesive		
<p>Low homotypic adhesion and high heterotypic adhesion</p> <p>Cell type 1    Cell type 2    Adhesion 1 ↔ 2                      PTC            PTC            20                      PTC            other           Tested 0, 1, 3, and 5</p>	By 24 h, the spheroid has fragmented while the mesothelium has aggregated		
<p>High homotypic adhesion and high heterotypic adhesion</p> <p>Cell type 1    Cell type 2    Adhesion 1 ↔ 2                      PTC            PTC            0                      PTC            other           0</p>	By 12 h, the spheroid has begun to disintegrate and the mesothelium has aggregated at the base of the spheroid		
<p>High homotypic adhesion and low heterotypic adhesion</p> <p>No surface area constraint</p> <p>Cell type 1    Cell type 2    Adhesion 1 ↔ 2                      PTC            PTC            0                      PTC            other           Tested 10 and 20</p>	At 24 h, a coherent spheroid with a similar appearance to the SKOV3.ip1 <i>in vivo</i> tumors can be seen. The mesothelium remains intact. However, cells are abnormally convoluted		
<p>High homotypic adhesion and low heterotypic adhesion</p> <p>Additional surface area constraint</p> <p>Cell type 1    Cell type 2    Adhesion 1 ↔ 2                      PTC            PTC            0                      PTC            other           See <b>Table 2</b></p>	This model most closely approximates the shape of SKOV3.ip1 spheroids and cells <i>in vivo</i> as shown at 12 h		

## RESULTS

SKOV3.ip1 ovarian cancer cells adhere to the surface of numerous organs in the peritoneum and form large tumors by two weeks post-injection.

To recapitulate the essential steps in ovarian cancer relapse from minimal residual disease in the peritoneum, five million SKOV3.ip1 human ovarian cancer cells expressing GFP were injected into the peritoneum of nude mice as a single cell suspension. Mice were euthanized after two weeks and mounted on the stage of an OV100 fluorescence imaging system. As shown in Figure 1A, macroscopic tumors developed on numerous organs in the peritoneum during this period. The main sites of attachment were the omentum (Figure 1 A, B), the surface of the stomach (Figure 1C) and small intestine, the mesentery (Figure 1D) and the spleen (Figure 1E). Tumors also develop on the liver in half of the mice examined. The largest tumors grow from the omentum and expand into the peritoneum, reaching volumes up to  $200 \text{ mm}^3$  by two weeks. Even within this short time frame, the tumors are well vascularized with vessels penetrating and wrapping around the outside of the largest tumors. Many smaller tumors can be found attached to the mesentery, often visible to the naked eye, but ranging in size from  $0.4 \mu\text{m}^3$  to  $1 \text{ mm}^3$ .

Figure 1

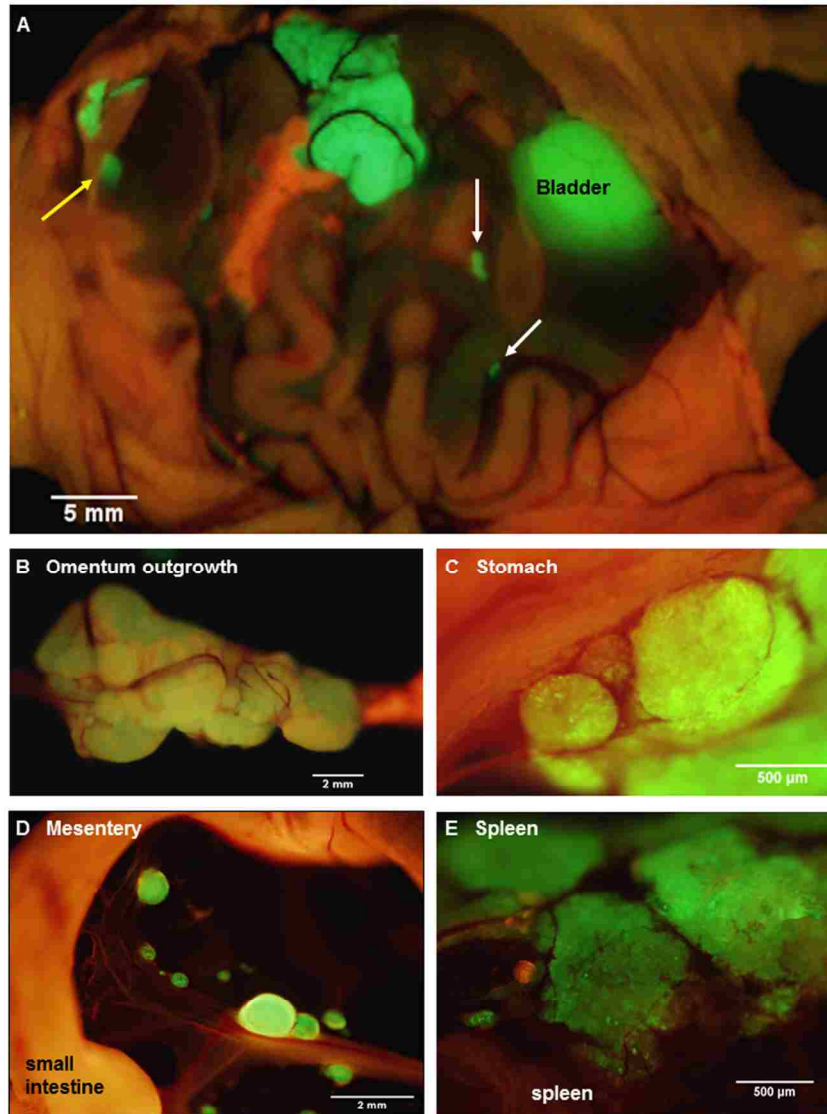


Figure 1. SKOV3.ip1-GFP cells colonize the surface of many organs in the mouse peritoneum. (A) Whole body image of SKOV3.ip1 tumors growing from the omentum (large central tumor), the intestine, attached mesentery (white arrows), and the liver (yellow arrow) of an RFP nude mouse. Tumors on the spleen are not visible in this image. (B) The largest tumors are attached to the omentum located on the larger curvature of the stomach and are well vascularized. (C) Tumors attached to the stomach are spherical and non-invasive. (D) On the mesentery, small tumors are located adjacent to major blood vessels. (E) Small tumors growing on the spleen have a flatter, sponge-like morphology with less well defined borders between the tumor and the normal tissue.

### **Strong homotypic interactions drive SKOV3.ip aggregation.**

It has been hypothesized that ovarian cancer cells aggregate and form spheroids when suspended in peritoneal fluid and that these spheroids then attach to the peritoneal surface and form large tumors (Shield et al., 2009). To test this hypothesis and to assess the clonality of the tumors at distinct sites, a mixture of SKOV3.ip1-GFP and SKOV3.ip1-RFP cells were co-injected into nude mice as a single cell suspension and the resulting tumors were imaged two weeks later. Tumors on the omentum developed as well-mixed chimeras, with both green and red fluorescence throughout (Figure 2A and B). In higher magnification images, small areas with predominantly red fluorescence can be distinguished from areas with predominantly green fluorescence, but there are no large sections of tumor expressing a single fluorescent protein (Figure 2C). The majority of the observed mesenteric tumors (92% +/- 2% of 51 observed tumors) also have mixed green and red fluorescence, indicating that even these small tumors originated from a mixed spheroid (Figure 2D and E). The few small tumors consisting solely of GFP-positive or RFP-positive cells may represent rare instances where a single cell, or a small group of singly fluorescent cells, was able to adhere and grow (Figure 2E, arrow).

These data provided the first essential parameters for initialization of our OvTM mathematical model, since adhesion is a predominant feature of the cellular Potts framework (Graner and Glazier, 1992). Simulations were initiated with an adherent spheroid on the surface of the intestine. The spheroid subsequently pushes through the mesothelium. This process has been observed *in vitro*, where tumor spheroids cause retraction of the mesothelium using a myosin-mediated process (Iwanicki et al., 2011).

Figure 2

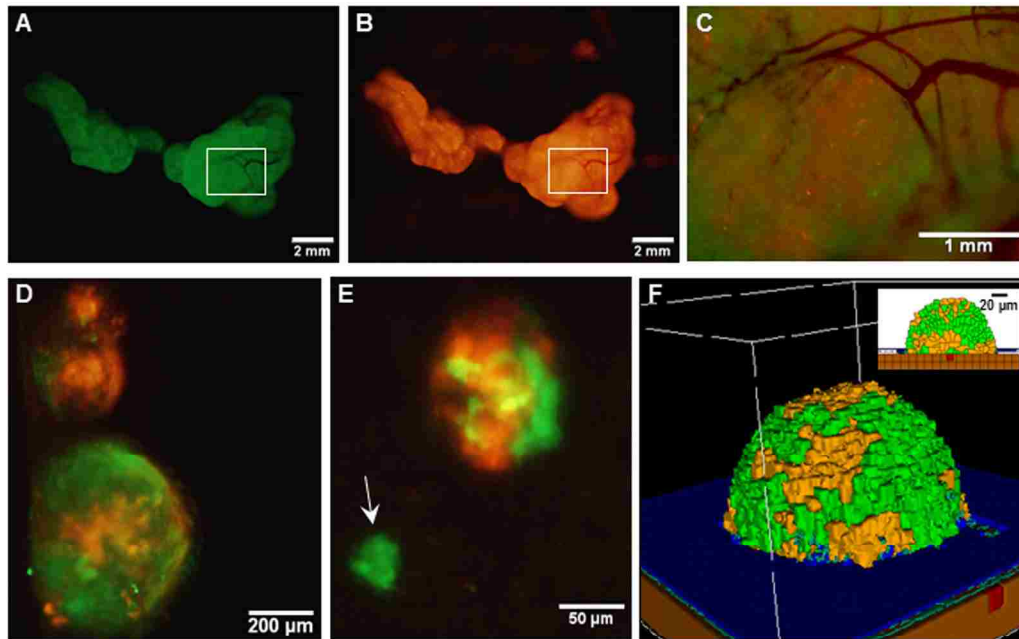


Figure 2 Co-injected SKOV3.ip1-GFP and RFP cells yield chimeric tumors. Equal numbers of SKOV3.ip1-GFP and SKOV3.ip1-RFP cells were injected as a single cell suspension into the peritoneum of nude mice. (A – C) Large tumors on the omentum are both GFP-positive (A) and RFP-positive (B). White boxes: magnified region shown in C. (C) A magnified composite image of the tumor from A and B showing a mixture of GFP- and RFP-positive cells. (D – E) Chimeric tumors on the mesentery have patches of green and red fluorescence. A clonal tumor that is only GFP-positive can be seen (E, arrow). (F) Endpoint of a mathematical simulation initialized with a mixed GFP/RFP spheroid of 56 cells attached to the mesothelial surface of the intestine. A  $180 \times 180 \times 180 \mu\text{m}$  lattice ( $5.832 \text{ mm}^3$ ) is partitioned into layers of smooth muscle (brown), extracellular matrix fibers (teal), mesothelium (dark blue), and vessel (red) creating a  $0.84 \text{ mm}^3$  tissue layer. Above the tissue is peritoneal fluid. The 3-D image shows a chimeric tumor (orange and green cells) after 7 days of growth.

The *in silico* experiments using OvTM showed that only by assigning high homotypic adhesion strength to the cancer cells could the model reproduce spheroid cohesiveness and growth (Figure 2F). For details on how the adhesion parameters were optimized, see Materials and Methods (Table 3). Simulations in which tumor cells adhered more strongly to other tumor cells than to any other cell type produced the most rounded tumor morphology that closely resembled the xenograft tumors. Adding a cellular surface area constraint maintained the integrity of the cells themselves. Since the model indicated that tumor cell homotypic adhesion is an essential feature governing dissemination and growth, this concept was further tested experimentally by sequentially introducing fluorescent tumor cells into the peritoneum (Figure 3). In this experiment, tumors were first established by injection of 2.5 million SKOV3.ip1-GFP cells. After a period of one week to permit engraftment of the green fluorescent cells, an equal number of SKOV3.ip1-RFP cells were injected. Following another week, the relative distribution and burden of both green and red fluorescent tumor cells were evaluated. As expected, SKOV3.ip1-GFP tumors formed on the omentum, mesentery, and spleen. Notably, the majority of red fluorescent cells adhered to and enveloped the pre-existing GFP-positive tumors as can be seen on the omental tumors (Figure 3A) and on the spleen (Figure 3B), rather than forming tumors independently. Although some exclusively RFP-positive tumors were present on the mesentery (Figure 3C, arrows), 70% of the 24 RFP-positive tumors examined were also GFP-positive.

Figure 3

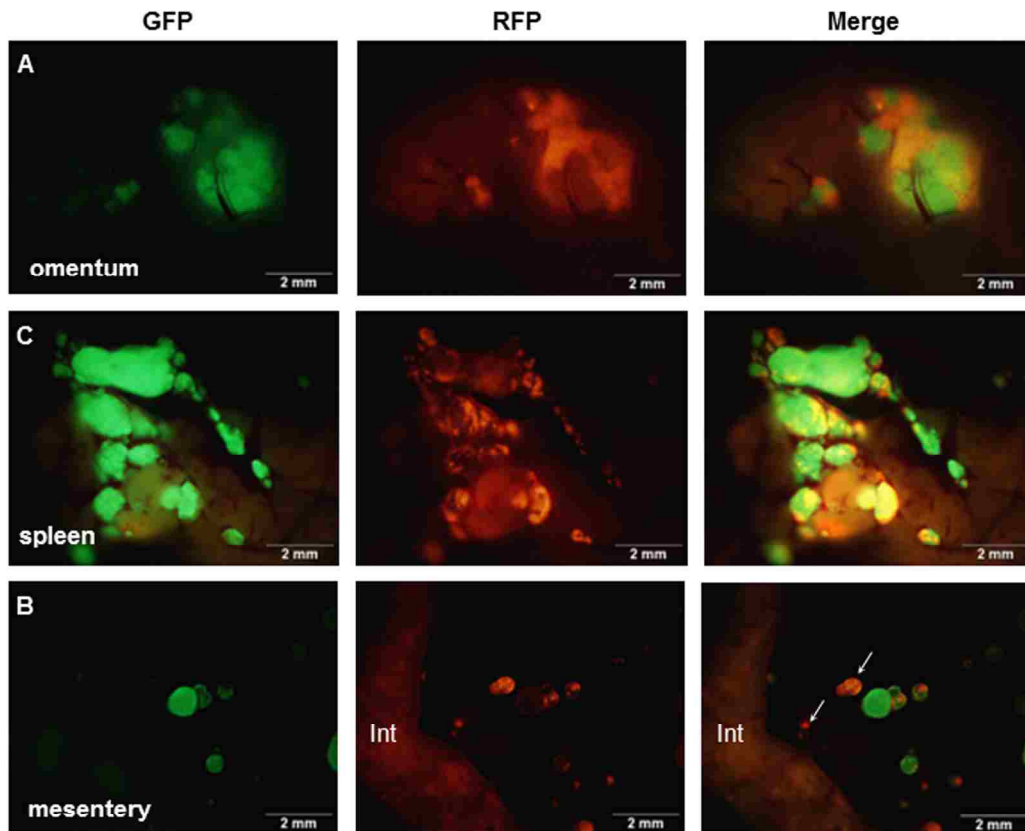


Figure 3. SKOV3.ip1-GFP and RFP cells injected sequentially emphasize the importance of tumor cell-cell adhesion. 2.5 million SKOV3.ip1-GFP cells were injected into nude mice and allowed to grow for one week before injection of an equal number of SKOV3.ip1-RFP cells. Tumors were imaged one week later. (A) SKOV3.ip1-RFP cells preferentially adhere to and coat existing GFP-positive tumors on the omentum. (B) Similar to the omentum, SKOV3.ip1-RFP cells preferentially adhere to existing GFP-positive tumors on the spleen. (C) On the mesentery, RFP-positive cells form new tumors (white arrows) as well as adhering to existing tumors. Int: small intestine (autofluorescent).

## **Tumor cells migrate through the open architecture of the mesentery in response to chemotactic signals.**

Our next goal was to identify specific features of the microenvironment that underlie differences in ovarian tumor morphology by examining the structure of external tissue layers facing the peritoneum. Both normal and tumor-associated tissues were extracted and prepared for TEM imaging. The micrograph in Figure 4A illustrates the open architecture of the normal mesentery, with loosely packed fat cells below the mesothelium (Figure 4A). The mesothelial layer is remarkably thin in some areas, ranging from 0.4 to 2.5 microns in thickness. A second image (Figure 4B) shows a cross section of mesentery excised from mice engrafted with SKOV3.ip1 human ovarian cancer cells. Labels mark the locations of probable tumor cells, identified by the characteristic ultrastructure of their nuclei. The tumor cells are interior to the mesothelium and adjacent to a small blood vessel.

To understand how tumors are established in the mesentery, SKOV3.ip1-GFP cells were injected into the peritoneum and four days later segments of the mesentery were removed for whole mount imaging. As shown in Figures 4C-D, images from this early time point provide a window into the initial steps in the engraftment process. Small groups of fluorescent tumor cells were seen within the mesenteric adipose layer (Figure 4C) or beneath the adipose layer immediately adjacent to vessels (Figure 4D).



Figure 4

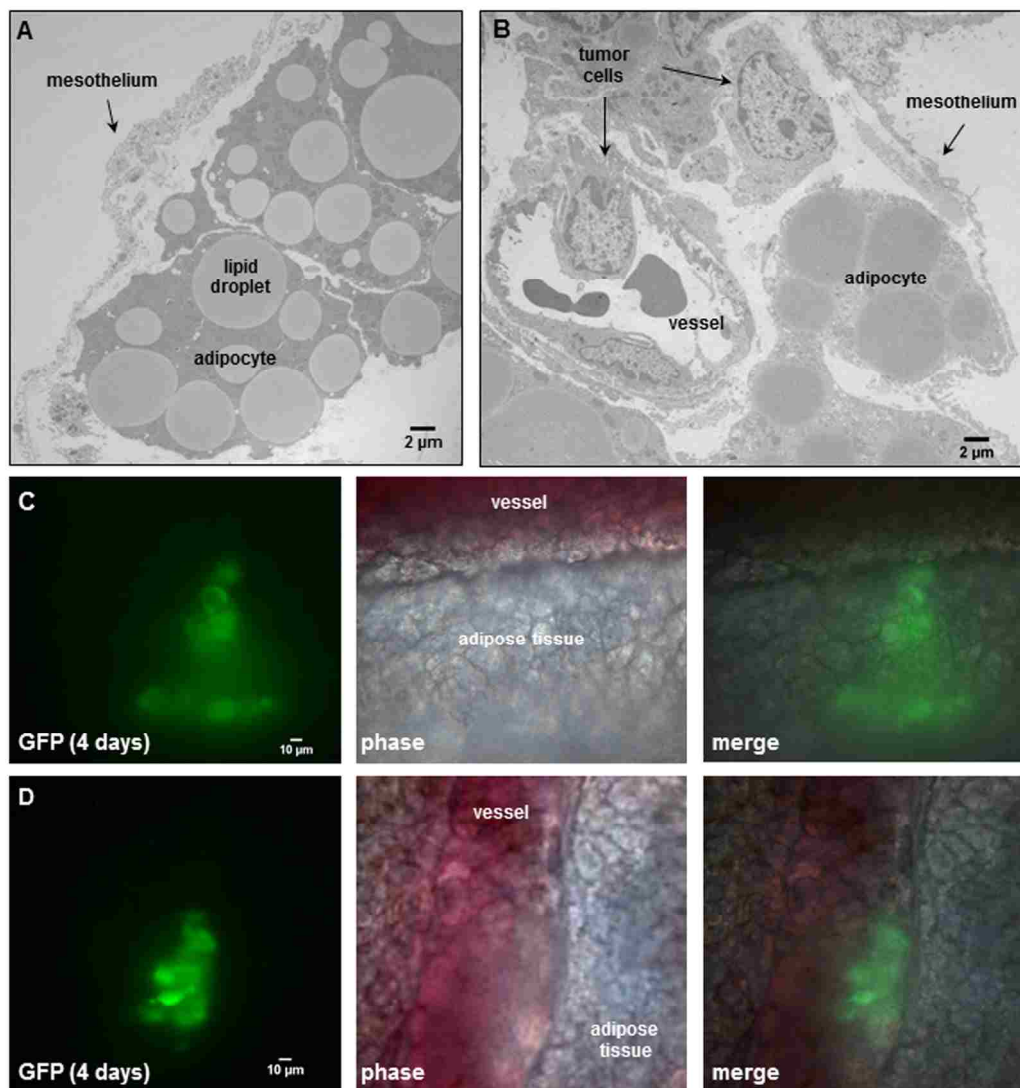


Figure 4. Four days post-injection, tumor cells have invaded the mesentery and migrated through adipose tissue to approach mesenteric blood vessels. (A) Transmission electron micrograph of the edge of the mesentery from a nude mouse. The mesentery architecture is open with loosely connected adipose cells below the mesothelium. Adipocytes are identified by their large lipid droplets. (B) Transmission electron micrograph of mesentery excised four days post-injection of SKOV3.ip1 cells. Arrows mark the locations of probable tumor cells. The tumor cells lie close to a blood vessel. (C) Tumor cells invading mesenteric adipose tissue adjacent to a vessel. On the right, GFP fluorescence of the tumor cells; middle, brightfield; left, composite image. (D) Tumor cells closely opposed to a mesenteric vessel. Panels are arranged as in C.

We next used OvTM to evaluate the conditions necessary for tumor cells to migrate to mesenteric vessels within this short time period. The cellular Potts model is particularly well suited for this type of modeling, since it specifically represents cell-cell interactions and cell movement, which is governed by local contacts and chemotactic gradients. The three-dimensional stochastic model was populated with heterogeneous cell types (tumor cells, adipocytes, endothelial cells, and mesothelium) and geometric features (shape, location, organization and thickness of tissue layers) based on TEM images. Extracellular factors, such as chemokines and oxygen, are described by diffusion equations with sources and sinks. In each case, tumor cells push through the mesothelial layer and degrade the underlying extracellular matrix, as shown experimentally (Sodek et al., 2008). Simulations can then demonstrate the extent of tumor invasion in response to different chemotactic environments.

Figure 5 shows results from three scenarios that were considered in these simulations. Movies for representative simulations are provided in Supplementary Data (Supplementary Movies M1-3). For each case, a spheroid of seven tumor cells was initially positioned on a 3D geometrical model of the mesentery. Mesothelial cells form the boundary with the peritoneum; adipocytes are dispersed within the interior, and a single vessel transverses the tissue.

In the first scenario, there is no local production of chemotactic factors imposed. The spheroid is positioned such that it is in contact with the ECM. In the absence of chemotactic factors, the spheroid dissolves the ECM and presses into the adipose tissue

after two days (Figure 5A). This progression is too slow to explain tumor cell localization near mesenteric blood vessels in the mouse model.

SKOV3.ip1 cells have been shown to home towards chemokine-producing adipocytes and upregulate the IL-8 receptor (CXCR1) when co-cultured with adipocytes (Nieman et al., 2011). Therefore, in the second scenario, simulation parameters were modified such that all adipocytes within the mesentery secrete IL-8 at a rate of  $2.2 \times 10^{-4}$  pg/min/cell (Bruun et al., 2004), which diffuses at  $1.5 \times 10^4$   $\mu\text{m}^2/\text{min}$  (Li Jeon et al., 2002). Tumor cells are then allowed to chemotax up the resulting IL-8 gradient. In our model, spheroid invasion of the ultra-thin mesothelium is rapid, occurring at a rate of 10  $\mu\text{m}/\text{hr}$  based upon the *in vitro* experiments of Iwanicki et al. (Iwanicki et al., 2011). The pseudo-colored image in Figure 5B shows the predicted distribution of IL-8 in the mesenteric tissue at steady state, illustrating the initial conditions experienced by the tumor spheroid. Simulated IL-8 concentrations within the peritoneum agree with those measured experimentally (Barcz et al., 2002). When IL-8 chemotaxis is included in the simulation, the spheroid moves past the mesentery barrier and pushes between adipocytes to settle near the center of the adipose layer where the IL-8 concentration is greatest (Figure 5D). This occurs within 500 minutes after initialization. In this case, rapid chemotaxis occurs, but the tumor cells do not localize near the vessel.

In the final case, both adipose and endothelial cells are assumed to produce chemotactic factors that attract tumor cells. We introduce a new chemotactic factor (Chemotactic Factor 2) that originates from the mesenteric vessel. Steady state values represented in

the pseudo-colored profile in Figure 5C show that a significant gradient can be established by endothelial cell secretion of Chemotactic Factor 2 at a rate of  $1.8 \times 10^{-4}$  pg/min/cell, which is comparable to that of IL-8 secretion from the adipocytes, and assuming diffusion and decay rates similar to VEGF. When cells are arranged in this geometry, the presence of both chemotactic gradients causes spheroids to penetrate the mesothelial layer, move by chemotaxis through the loose adipose layer towards the vessel, and halt at the tightly-adherent barrier of the vessel wall (Figure 5E). Together with the experimental data, these results support the conclusion that both adipocytes and endothelial cells are likely sources of chemokines that attract ovarian tumor cells.

Figure 5

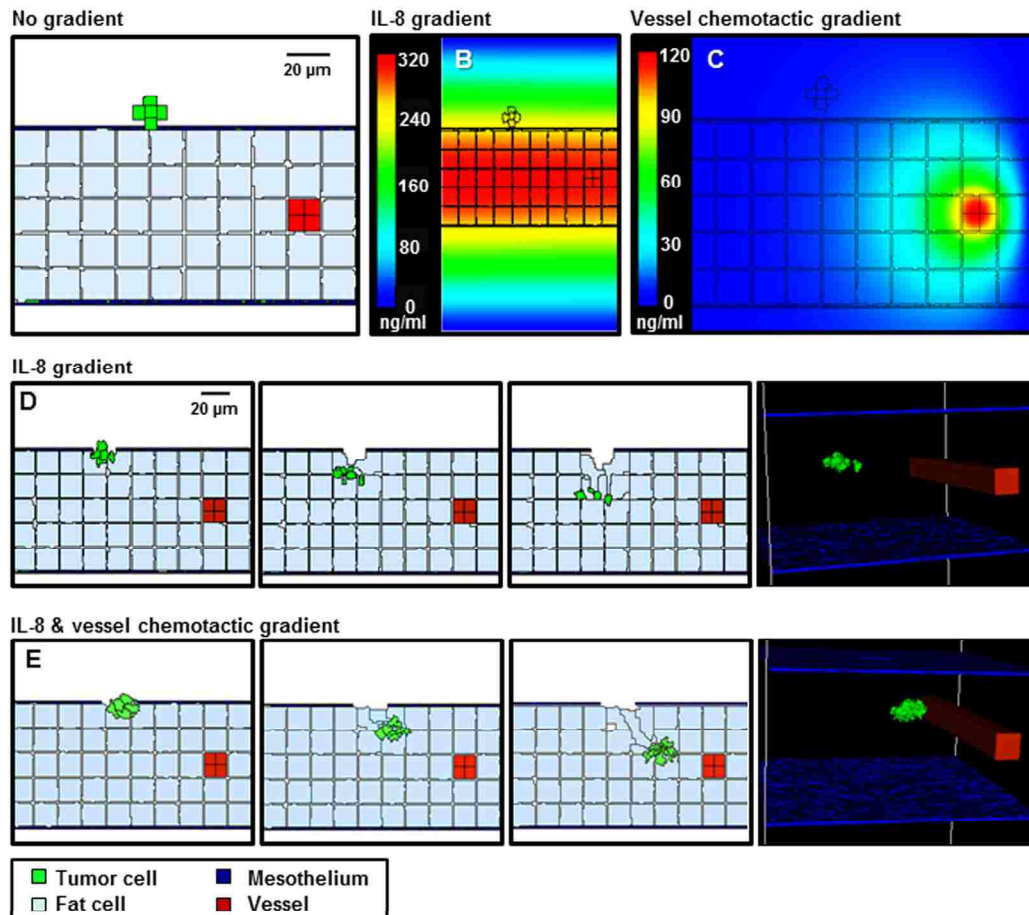


Figure 5. 3-D simulations of tumor cell attachment and migration to the mesenteric vessel. (A) The initial configuration of the simulation has a seven-cell spheroid attached to the surface of the mesentery. To model this environment,  $170 \times 170 \times 263 \mu\text{m}$  lattice ( $7.6 \text{ mm}^3$ ) is partitioned into five layers of adipocytes (light blue) sandwiched between single layers of mesothelium (dark blue) and ECM (teal) creating a  $2.6 \text{ mm}^3$  tissue layer surrounded by peritoneal fluid. A blood vessel on the right is represented by a solid rod (red). In the absence of chemotactic signals, the spheroid penetrates only the thin mesothelial layer at 1 to 2 minutes of simulation. (B and C) Steady-state distributions of chemotactic factors tested in these simulations. The color scale represents variation in factor concentrations in ng/ml. (B) The IL-8 gradient created by secretion of IL-8 from adipocytes. (C) A chemotactic gradient based on secretion of a hypothetical chemotactic factor (Chemotactic Factor 2) from mesenteric vessels. (D) Sequences in the simulation where a chemotactic gradient based on IL-8 is originating from the adipocytes. The spheroid migrates towards the center of the adipose layer. (E) Sequences of a simulation where chemotactic signals originate from both the adipocytes and the vessel. The spheroid migrates through the adipose layer towards the vessel.

### **Small SKOV3.ip1 tumors attached to surfaces of the stomach or small intestine are non-invasive and initiate angiogenesis.**

We next focused on explanations for the distinct morphology of tumors attached to the stomach or small intestine, which do not invade the tissue and instead grow outward into the peritoneal cavity (Figure 6A). We again sought insight from high resolution TEM images. As shown Figures 6C (mesentery) and 6D (stomach), the outer mesothelial layer remains relatively thin over these organs (typically 0.5 microns thick). The next layer is distinguished by dense collagen deposits. Prominent smooth muscle layers can be seen in both the small intestine and stomach, where the muscle cells are closely opposed and connected by gap junctions (Friend and Gilula, 1972) (arrows, Fig. 6B).

The morphology of a tumor attached to the outer rim of the lower intestine is seen at a lower magnification in Figure 6E, which shows a representative section from a formalin-fixed, paraffin block stained with H & E (hematoxylin and eosin). The smooth muscle of the small intestine remains intact at the tumor/tissue interface. Thus, tumors attached to the exterior of the gut are presented with a discrete barrier and adapt by growth into the available and flexible space between organs. The intestine has a capillary bed that provides oxygen to the mesothelium and contributes to the oxygenated peritoneal environment (Figure 6F). Because of the lack of a smooth muscle barrier, these vessels may provide a more accessible endothelial source for neoangiogenesis critical to tumor success.

Microscopic evaluations provide support for this hypothesis (Figure 6B and 6E). Fluorescence imaging shows the remarkable extent of tumor vascularization, even in young GFP-positive tumors attached to the intestinal wall at 2 weeks post-engraftment

(Figure 6B). A red arrowhead in Figure 6E points to a vessel visible within the tumor cross-section. This evidence led us to conduct simulations to explain the rapid onset of neovascularization in the absence of invasion.

Figure 6

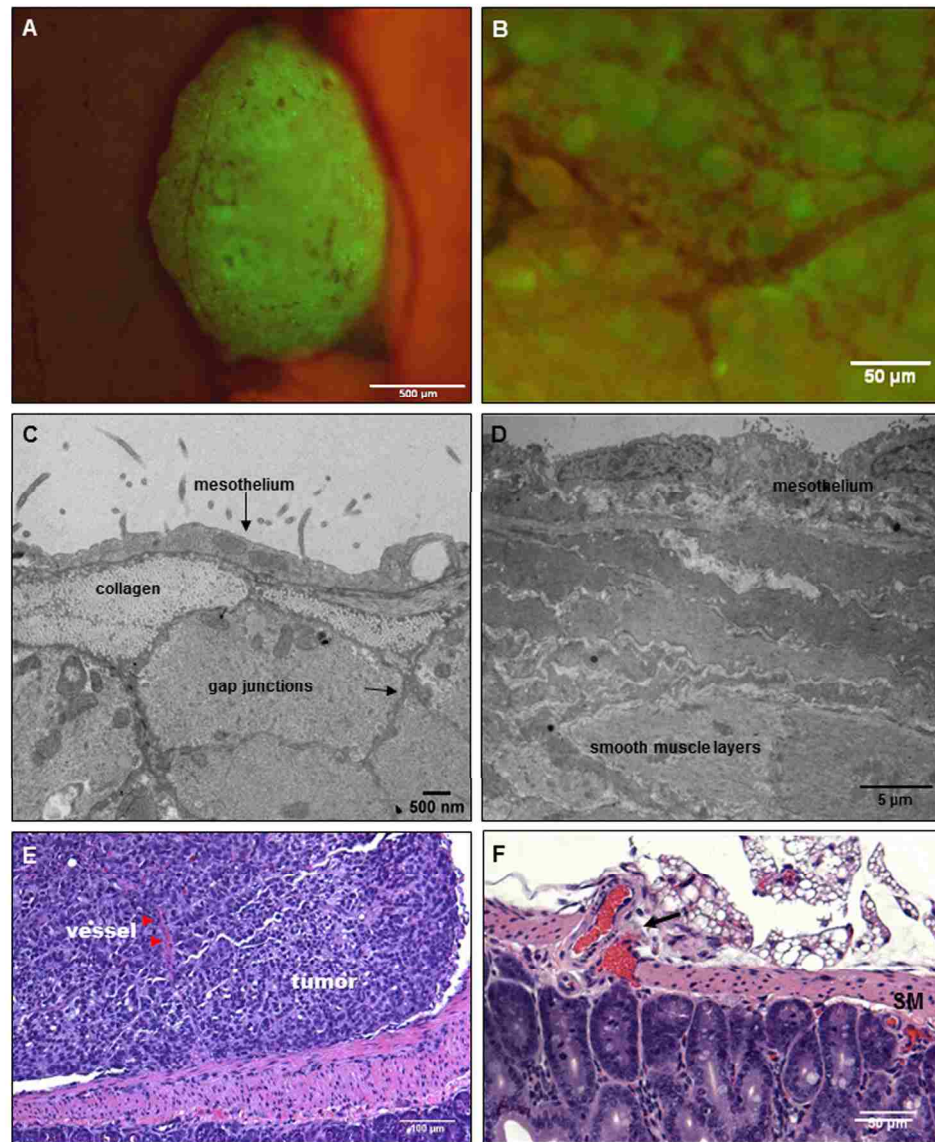


Figure 6. Tumors that adhere to the walls of the small intestine are spherical and non-invasive. (A) An SKOV3.ip1-GFP tumor adhering to the wall of the small intestine two weeks post-injection in an RFP nude mouse. Shown is a composite GFP/RFP image. Small vessels are visible on the surface of the tumor. (B) Higher magnification image of the vascular tree infiltrating a green fluorescent tumor on the intestine. (C) Transmission electron micrograph of the small intestine wall. Tissue was collected from a nude mouse four days post-injection with SKOV3.ip1-GFP cells. The wall of the small intestine consists of a thin layer of mesothelium overlaying bundles of smooth muscle fibers. (D) TEM image of stomach ultrastructure, illustrating the distinct cellular layers. (E) An H&E-stained section of a tumor attached to the small intestine. There is a clear delineation between the intestine and the tumor. The tumor is vascularized (red arrowhead). (F). An H&E-stained section of the surface of a mouse intestine. Arrow points to vessels at the intestine-mesentery junction.



**SKOV3.ip1 tumor spheroids are initially well oxygenated and likely induce neovascularization via constitutive secretion of angiogenic factors.**

For the *in silico* model of angiogenesis, micron-scale geometric parameters for the tissue surface architecture were again determined from TEM images. For the gut, adhesion between smooth muscle cells is set sufficiently high as to prevent spheroid penetration below the mesothelial and collagen layers. Under these constraints, simulations of tumor adhesion and growth result in the formation of spherical tumors that are consistent with the morphology of engrafted tumors on mouse intestine (compare Figures 6A and 7C). Since these simulations incorporate published values for oxygen content in the peritoneal fluid and oxygen diffusion rate (Macdougall and McCabe, 1967; Kizaka-Kondoh et al., 2009), it is possible to calculate the distribution of oxygen in all locations during tumor growth. By coarse-graining the model (1 voxel=1 cell), we were able to determine the oxygen concentration gradients for large spheroids suspended in the peritoneal fluid. In spheroids of varying sizes, oxygen concentration decreased within the core. However, spheroids up to 336  $\mu\text{m}$  in diameter (58,000 cells) approach the hypoxic threshold of 19 mm Hg of  $\text{O}_2$  (Höckel and Vaupel, 2001), but are not yet hypoxic at their core (Figure 7A). Continued growth to 364  $\mu\text{m}$  in diameter (74,000 cells) results in a hypoxic core with an oxygen concentration of 0.5 mm Hg (Figure 7B), leading to the prediction that the hypoxic threshold is reached when the spheroid is between these two sizes. Tumor sizes in mouse samples were compared based on the cross-sectional area of tumors in H&E-stained sections. Mesenteric tumor vascularization with respect to tumor area is

shown as scatter dot plots in Figure 7E. Of the 76 tumors measured, all tumors above the predicted hypoxic threshold (red) were vascularized. However, 57% of small tumors with an area of  $<104,000 \mu\text{m}^2$  (below the predicted hypoxic threshold) were also vascularized. These results suggest that angiogenesis is not solely hypoxia-driven in the SKOV3.ip1 model.

In the next series of simulations, we examined how angiogenesis might originate from these spheroids in the absence of hypoxic signaling. There is experimental evidence that SKOV3.ip1 cells constitutively express VEGF *in vivo* and *in vitro* even when maintained in well-oxygenated tissue culture conditions (Yoneda et al., 1998). Secretion of VEGF by the tumor cells was therefore incorporated into these simulations. Small spheroids attached to the gut penetrate the mesothelial layer, permitting VEGF secreted from tumor cells to initiate chemotactic gradients and attract endothelial cells that line blood vessels in the sub-mesothelial layer. The process of angiogenesis is driven by endothelial cell chemotaxis toward VEGF, and adhesive interactions between endothelial sprout cells and tumor cells. To produce vasculature visually similar to that in very small xenograft tumors, latent endothelial cells must begin to proliferate and migrate as soon as the spheroid comes close enough to the vessel to allow diffusion of low concentrations of VEGF. Given spheroid VEGF production of  $3.82 \times 10^{-7}$  pg/min/SKOV3.ip1 cell, the threshold for the switch from latent to sprouting endothelial cells was set at  $2.08 \times 10^{-8}$ , to initiate angiogenesis when the spheroid is ~5 microns from the vessel.

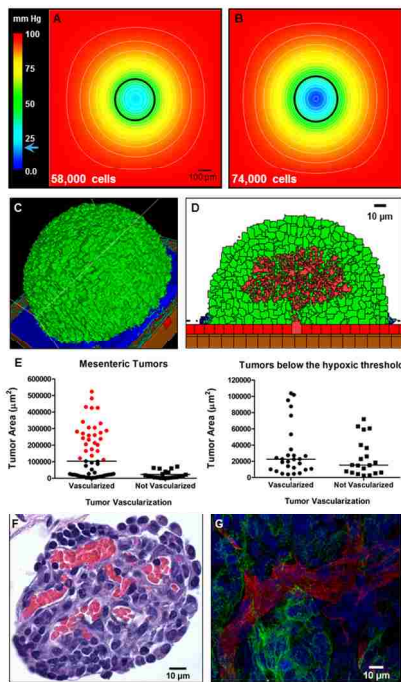


Figure 7

Figure 7. Vasularization of tumors is rapid and can be attributed to constitutive release of angiogenic factors by SKOV3.ip1 cells. (A and B) Representations of the steady-state oxygen gradients from coarse-grained simulations of spheroids suspended in peritoneal fluid. The color scale indicates the range of oxygen concentrations in mm Hg. Black circles mark the perimeter of the spheroids. (A) The oxygen gradient through the middle of a spheroid 336  $\mu\text{m}$  in diameter (58,000 cells). At this size, all cells are well oxygenated with an oxygen partial pressure above the hypoxic threshold of 19 mm Hg (indicated on the color scale as a blue arrow). The lowest oxygen concentration at the core of the spheroid is 21.6 mm Hg. (B) The oxygen gradient through the middle of a spheroid 364  $\mu\text{m}$  in diameter (74,000 cells). By the time a spheroid has reached this size, the core is hypoxic (0.5 mm Hg). (C and D) OvTM simulations of angiogenesis in a tumor attached to the intestinal wall, assuming constitutive release of VEGF from cancer cells. (C) 3D image of the simulation after 7.8 days when the tumor has grown to 6,400 cells. (D) 2D slice through the middle of the tumor in D to show vessel tree morphology. (E) Scatter dot plots of mesenteric tumor vascularization with respect to cross-sectional tumor area as determined from H&E-stained sections of mouse intestine and mesentery collected three weeks post-injection. Tumor areas of all mesenteric tumors measured are plotted on the left. Tumors with areas above the predicted hypoxic threshold are in red. All non-vascularized tumors fall below the hypoxic threshold. The right plot shows the area and vascularization status of small tumors that fall below the hypoxic threshold. A majority of these small tumors (57%) are also vascularized. Lines indicate the median value. (F) Cross-sectional view of a small mesenteric tumor after H&E staining. Red blood cells (red) can be seen populating vessels within the tumor (blue). (G) Confocal image of ovarian tumor removed from the surface of the gut and labeled with anti-CD31 antibody (endothelial cell marker, red fluorescence) to distinguish tumor vasculature. An anti-GFP antibody with a FITC-labeled secondary antibody marks GFP-expressing tumor cells; Hoechst (blue fluorescence) labels the nuclei of all cells in the field of view.

Angiogenesis in the OvTM model follows validated methods that treat VEGF as diffusible molecules whose gradient, together with the biophysical environment, drives endothelial migration and proliferation, and eventually morphogenesis of vessel sprouts (Bauer et al., 2007; Shirinifard et al., 2009). Parameters and model assumptions are described in Materials and Methods. Simulation results show that constitutive production of VEGF from even a small spheroid of SKOV3.ip1 cells should be capable of initiating vascular outgrowths that penetrate the spheroid within 12 hours of attachment (Figure 7D, Supplementary Movie M4). Results of the computational model are consistent with our experimental observations that even very small tumors, comprised of less than 20,000 SKOV3.ip1 cells, are fully vascularized (Figure 7F). They are also consistent with 3-D images of tumor slices stained for confocal fluorescence imaging that show extensive tumor vascularization three weeks post-injection (Figure 7G). In this final image, an anti-CD31 antibody (red) marks endothelial cells, Hoechst (blue) stains the cell nuclei and an anti-GFP antibody (green) labels the GFP-positive tumor cells. A rotating 3D view of this tumor section is found in Supplementary Movie M5.

## **DISCUSSION**

In this work, we combine a murine xenograft model with a computational model, OvTM, to evaluate critical factors governing the dissemination and growth patterns of ovarian cancer in the peritoneum. These models best represent ovarian cancer relapse after debulking surgery, where disease progression initiates from microscopic residual disease in the peritoneal chamber.

In cellular Potts models, the variety of constraints placed on cells must be properly balanced to produce biologically reasonable cellular and tissue structure and movement. We quantitatively modeled oxygenation in a simple spheroid to estimate at what diameter the tumor center would become hypoxic, for comparison with diameters of vascularized tumors observed in the mouse xenografts. Tumor cell homotypic and heterotypic adhesions on smooth muscle were then tuned to regenerate the spheroidal morphology of SKOV3.ip1 xenograft tumors on small intestine or stomach (Figure 6A). To simulate the depth to which spheroids penetrate in soft tissue due to a chemotactic motive force, the underlying tissue structure was adjusted to represent a fatty section of the mesentery. In the simulations, tumors remain on the surface of smooth muscle, a tissue with many underlying tight junctions (Figure 6C and D), and invade soft tissues with space between cells, such as the mesentery (Figure 4A).

Finally, we simulated VEGF-driven angiogenic morphogenesis borrowing from previous methods using cellular Potts models for tumor-driven angiogenesis (Bauer et al. 2007, Bauer et al, 2009, Shirinifard et al. 2010), in which endothelial cell chemotaxis towards soluble VEGF leads to angiogenic sprouting and branching. These models treated VEGF as a diffusible molecule whose gradient, together with the biophysical environment, drives endothelial migration and proliferation, and eventually morphogenesis of vessel sprouts. We did not include other angiogenesis dynamics from Bauer et al. 2009, which considered endothelial cell interactions with ECM to further drive sprouting morphogenesis, nor does our model assess tumor growth as in Shirinifard et al. 2010, which modeled tumor growth in response to a growing network of surrounding vessels

providing nutrients. Instead, angiogenesis was modeled as a simple morphogenetic process driven by chemotaxis and differential adhesion that penetrates a 3-dimensional tumor. The sprouting vessel's base cell (or cells) has a semi-permanent elastic bond to the existing vessel, describing the labile adhesion interactions between them. Otherwise, differential adhesions between tumor and endothelial cells facilitate endothelial sprouting up the VEGF gradient.

The basic OvTM model and parameter set remain the same for all three groups of simulations (spheroids on muscle, spheroids invading mesenteric fat, and angiogenic sprouts in spheroids on muscle), except for the following. Between the cases of spheroid growth in different niches, the tissue surface is comprised of different cell types with their associated parameters. In angiogenesis simulations, the volume constraint for cancer cells was increased to help prevent cell fragmentation during migration. Constraints on endothelial cells in the angiogenesis model (proliferating endothelial, non-proliferating endothelial, and permanent vessel) include elastic labile adhesion bonds between each type of vascular cell and its neighbors. The CC3D simulation code will be available upon request to the authors.

We show that, for the aggressive SKOV3.ip1 cell line, homotypic adhesion between tumor cells is a defining feature that favors the aggregation of tumor cells into small spheroids. The spheroid morphology may promote adhesion-mediated cell survival signals and allow tumor cells to evade anoikis, a cell death program usually triggered by loss of cell adhesion to the extracellular matrix (Kim et al., 2012). We speculate that

these strong homotypic interactions may help to explain the typical clinical presentation where ovarian cancer is largely confined to the peritoneum and often accompanied by ascites. It is notable that others have shown spheroids are less susceptible to chemotherapeutic agents and may therefore contribute to relapse (Shield et al., 2009).

While some treatment regimens have focused on reducing metastatic spread through limiting tumor cell adhesion to the mesothelium (Sawada et al., 2012), we were interested in whether interactions between tumor cells might also be an important target. Using serial injections of green-fluorescent and red-fluorescent cells, we demonstrated that newly introduced tumor cells preferentially adhere to existing tumors. Strong cell-cell adhesion between tumor cells that stabilizes tumor clusters in the simulations could explain this observation. However, autocrine factors may also contribute to tumor cell homing, similar to the release of IL-6 and IL-8 from breast tumors that draws circulating tumor cells back to the primary tumor site (Kim et al., 2009). Although the mechanism is not well understood, therapies targeting ovarian tumor cell-cell homotypic adhesion may be worth consideration. In addition to limiting tumor mass, such drugs might be administered in combination with conventional chemotherapy to improve drug penetration.

Distinct niches within the peritoneal microenvironment also help to restrict tumor cells to the peritoneum and limit metastatic spread to other anatomical sites. Based upon the animal and mathematical models, colonization and growth is favored in loosely organized tissues. There are similarities between the open architectures of the mesentery and

omentum, two organs that are colonized by SKOV3.ip1 cells and share rich beds of adipose tissue known to secrete cytokines and growth factors attractive to tumor cells (Collins et al., 2009; Klopp et al., 2012). The adipocyte-rich omentum has a slightly thicker mesothelial layer than the mesentery, but has stomata or openings in the mesothelium above the milky spots that expose the underlying layers (Cui et al., 2002). The open architecture of these organs offers few barriers to tumor cells that undergo chemotaxis in response to local chemokine production. In contrast, even the aggressive SKOV3.ip1 tumor line is largely blocked by physical barriers such as the smooth muscle layers in the GI tract.

Our work is consistent with recent studies by Nieman et al., who showed that SKOV3.ip1 cells adhere to the omentum as early as 20 minutes post injection and migrate in response to IL-8 and other chemotactic agents produced by adipocytes (Nieman et al., 2011). In addition, we provide new evidence suggesting that SKVO3.ip1 cells migrate through the mesothelium and adipose tissue towards mesenteric vessels. Chemotaxis of tumor cells towards existing vessels has been observed in rodent models injected subcutaneously with mammary carcinoma cells (Li et al., 2000). Based on results from OvTM simulations, we propose that a chemotactic factor originating from the vessel may mediate this process. Although the identity of the factor is unknown, it is possible that vessels also produce an IL-8 gradient that attracts tumor cells, since activated vascular smooth muscle cells are capable of producing IL-8 (Wang et al., 1991). Growth factors secreted by perivascular tumor-associated macrophages, such as the epidermal growth



factor (EGF), could also promote local survival and proliferation of tumors that take up residence near vessels (Lewis and Pollard, 2006).

Interestingly, rodent models that showed tumor migration to blood vessels also exhibited early angiogenesis in tumors consisting of fewer than 300 cells (Li et al., 2000). The constitutive expression of angiogenic factors by SKOV3.ip1 cells may be the single most important feature contributing to the aggressive growth of this tumor cell line after engraftment. In preliminary data not shown, microarray studies showed that VEGF mRNA levels differ less than 2-fold in cultured SKOV3.ip1 cells versus *in vivo*. In OvTM simulations, this modest level of constitutive production is sufficient for even minute tumor spheroids to recruit endothelial cells from nearby vessels (Figure 7). This result is in contrast to the classical solid tumor situation, where angiogenesis is initiated only after the interior tumor cells become hypoxic and upregulate VEGF production (Shweiki et al., 1992;Pugh and Ratcliffe, 2003). In patients, however, it is important to note that the balance of constitutive and induced production of angiogenic factors by tumor cells may vary widely. Therefore, assessment of angiogenic factor transcriptional profiles or direct measurement of angiogenic factor levels in serum/cystic fluid may be critical to identify patients at risk for relapse, a concept that has also been proposed by others (Harlozinska et al., 2004;Li et al., 2004).

**CONFLICT OF INTEREST STATEMENT:** The authors disclose no potential conflicts of interest.

## ACKNOWLEDGEMENTS

Use of the UNM Electron Microscopy, Fluorescence Microscopy and Flow Cytometry Shared Resource Centers at the UNM SOM and Cancer Center, and NIH support for these cores, is gratefully acknowledged. Angela Welford and Rachel Grattan collected the EM images for this work. The authors thank Dr. James Glazier and other members of the CompuCell3D development team. Dr. Hoffman is the founding director of AntiCancer Inc. This work was supported by NIH R01CA119232 (BW), NIH P50GM065794 (BW) and NIH R25CA153825 (J Oliver).

## REFERENCES

- Arakelyan, L., Merbl, Y., and Agur, Z. (2005). Vessel maturation effects on tumour growth: validation of a computer model in implanted human ovarian carcinoma spheroids. *European Journal of Cancer* 41, 159-167.
- Ausprunk, D.H., and Folkman, J. (1977). Migration and proliferation of endothelial cells in preformed and newly formed blood vessels during tumor angiogenesis. *Microvasc Res* 14, 53-65.
- Bagley, R.G., Walter-Yohrling, J., Cao, X., Weber, W., Simons, B., Cook, B.P., Chartrand, S.D., Wang, C., Madden, S.L., and Teicher, B.A. (2003). Endothelial Precursor Cells As a Model of Tumor Endothelium. *Cancer Research* 63, 5866-5873.
- Barcz, E., Skopinska Rózewska, E., Kaminski, P., Demkow, U., Bobrowska, K., and Marianowski, L. (2002). Angiogenic activity and IL-8 concentrations in peritoneal fluid and sera in endometriosis. *International Journal of Gynecology & Obstetrics* 79, 229-235.
- Bast, R.C., Hennessy, B., and Mills, G.B. (2009). The biology of ovarian cancer: new opportunities for translation. *Nat Rev Cancer* 9, 415-428.
- Bauer, A.L., Jackson, T.L., and Jiang, Y. (2007). A Cell-Based Model Exhibiting Branching and Anastomosis during Tumor-Induced Angiogenesis. *Biophysical Journal* 92, 3105-3121.
- Bauer, A.L., Jackson, T.L., and Jiang, Y. (2009). Topography of Extracellular Matrix Mediates Vascular Morphogenesis and Migration Speeds in Angiogenesis. *PLoS Comput Biol* 5, e1000445.
- Bruun, J.M., Lihn, A.S., Madan, A.K., Pedersen, S.B., Schiøtt, K.M., Fain, J.N., and Richelsen, B. (2004). Higher production of IL-8 in visceral vs. subcutaneous adipose tissue. Implication of nonadipose cells in adipose tissue. *American Journal of Physiology - Endocrinology And Metabolism* 286, E8-E13.
- Burleson, K.M., Boente, M.P., Pambuccian, S.E., and Skubitz, A.P. (2006). Disaggregation and invasion of ovarian carcinoma ascites spheroids. *J Transl Med* 4, 6.

Casciari, J.J., Sotirchos, S.V., and Sutherland, R.M. (1992). Variations in tumor cell growth rates and metabolism with oxygen concentration, glucose concentration, and extracellular pH. *J Cell Physiol* 151, 386-394.

Casey, R.C., Burleson, K.M., Skubitz, K.M., Pambuccian, S.E., Oegema Jr, T.R., Ruff, L.E., and Skubitz, A.P.N. (2001).  $\beta$ 1-integrins regulate the formation and adhesion of ovarian carcinoma multicellular spheroids. *The American Journal of Pathology* 159, 2071-2080.

Chauviere, A.H., Hatzikirou, H., Lowengrub, J.S., Frieboes, H.B., Thompson, A.M., and Cristini, V. (2010). Mathematical Oncology: How Are the Mathematical and Physical Sciences Contributing to the War on Breast Cancer? *Curr Breast Cancer Rep* 2, 121-129.

Cickovski, T., Aras, K., Alber, M.S., Izaguirre, J.A., Swat, M., Glazier, J.A., Merks, R.M., Glimm, T., Hentschel, H.G., and Newman, S.A. (2007). From Genes to Organisms Via the Cell A Problem-Solving Environment for Multicellular Development. *Comput Sci Eng* 9, 50-60.

Collins, D., Hogan, A., O'shea, D., and Winter, D. (2009). The Omentum: Anatomical, Metabolic, and Surgical Aspects. *Journal of Gastrointestinal Surgery* 13, 1138-1146.

Cui, L., Johkura, K., Liang, Y., Teng, R., Ogiwara, N., Okouchi, Y., Asanuma, K., and Sasaki, K. (2002). Biodefense function of omental milky spots through cell adhesion molecules and leukocyte proliferation. *Cell and Tissue Research* 310, 321-330.

Evans, S.M., Schrlau, A.E., Chalian, A.A., Zhang, P., and Koch, C.J. (2006). Oxygen Levels in Normal and Previously Irradiated Human Skin as Assessed by EF5 Binding. *J Invest Dermatol* 126, 2596-2606.

Freyer, J.P., and Sutherland, R.M. (1985). A reduction in the in situ rates of oxygen and glucose consumption of cells in EMT6/Ro spheroids during growth. *J Cell Physiol* 124, 516-524.

Friend, D.S., and Gilula, N.B. (1972). VARIATIONS IN TIGHT AND GAP JUNCTIONS IN MAMMALIAN TISSUES. *The Journal of Cell Biology* 53, 758-776.

Gerber, S.A., Rybalko, V.Y., Bigelow, C.E., Lugade, A.A., Foster, T.H., Frelinger, J.G., and Lord, E.M. (2006). Preferential Attachment of Peritoneal Tumor Metastases to Omental Immune Aggregates and Possible Role of a Unique Vascular Microenvironment in Metastatic Survival and Growth. *Am J Pathol* 169, 1739-1752.

Giverso, C., and Preziosi, L. (2012). Modelling the compression and reorganization of cell aggregates. *Mathematical Medicine and Biology* 29, 181-204.

Giverso, C., Scianna, M., Preziosi, L., Buono, N.L., and Funaro, A. (2010). Individual cell-based model for in-vitro mesothelial invasion of ovarian cancer. *Math. Model. Nat. Phenom.* 5, 203-223.

Graner, F., and Glazier, J.A. (1992). Simulation of biological cell sorting using a two-dimensional extended Potts model. *Phys Rev Lett* 69, 2013-2016.

Harlozinska, A., Sedlacek, P., Kulpa, J., Grybos, M., Wojcik, E., Van Dalen, A., and Einarsson, R. (2004). Vascular endothelial growth factor (VEGF) concentration in sera and tumor effusions from patients with ovarian carcinoma. *Anticancer Res* 24, 1149-1157.

Höckel, M., and Vaupel, P. (2001). Tumor Hypoxia: Definitions and Current Clinical, Biologic, and Molecular Aspects. *Journal of the National Cancer Institute* 93, 266-276.

- Howdieshell, T.R., Mcguire, L., Maestas, J., and Mcguire, P.G. (2011). Pattern recognition receptor gene expression in ischemia-induced flap revascularization. *Surgery* 150, 418-428.
- Huang, S., Robinson, J.B., Deguzman, A., Bucana, C.D., and Fidler, I.J. (2000). Blockade of nuclear factor-kappaB signaling inhibits angiogenesis and tumorigenicity of human ovarian cancer cells by suppressing expression of vascular endothelial growth factor and interleukin 8. *Cancer Res* 60, 5334-5339.
- Iwanicki, M.P., Davidowitz, R.A., Ng, M.R., Besser, A., Muranen, T., Merritt, M., Danuser, G., Ince, T., and Brugge, J.S. (2011). Ovarian Cancer Spheroids Use Myosin-Generated Force to Clear the Mesothelium. *Cancer Discovery* 1, 144-157.
- Jain, H., Nör, J., and Jackson, T. (2008). Modeling the VEGF-Bcl-2-CXCL8 Pathway in Intratumoral Angiogenesis. *Bulletin of Mathematical Biology* 70, 89-117.
- Jiang, Y., Pjesivac-Grbovic, J., Cantrell, C., and Freyer, J.P. (2005). A Multiscale Model for Avascular Tumor Growth. *Biophysical Journal* 89, 3884-3894.
- Kenny, H.A., Kaur, S., Coussens, L.M., and Lengyel, E. (2008). The initial steps of ovarian cancer cell metastasis are mediated by MMP-2 cleavage of vitronectin and fibronectin. *The Journal of Clinical Investigation* 118, 1367-1379.
- Khan, S., Funk, H., Thiolloy, S., Lotan, T., Hickson, J., Prins, G., Drew, A., and Rinker-Schaeffer, C. (2010). In vitro metastatic colonization of human ovarian cancer cells to the omentum. *Clinical and Experimental Metastasis* 27, 185-196.
- Khanna, R., and Krediet, R.T. (eds.). (2009). *Nolph and Gokal's Textbook of Peritoneal Dialysis*. Springer.
- Kim, M.-Y., Oskarsson, T., Acharyya, S., Nguyen, D.X., Zhang, X.H.F., Norton, L., and Massagué, J. (2009). Tumor self-seeding by circulating cancer cells. *Cell* 139, 1315-1326.
- Kim, Y.-N., Koo, K.-H., Sung, J.Y., Yun, U.-J., and Kim, H. (2012). Anoikis Resistance: An Essential Prerequisite for Tumor Metastasis. *International Journal of Cell Biology* 2012.
- Kizaka-Kondoh, S., Itasaka, S., Zeng, L., Tanaka, S., Zhao, T., Takahashi, Y., Shibuya, K., Hirota, K., Semenza, G.L., and Hiraoka, M. (2009). Selective Killing of Hypoxia-Inducible Factor-1-Active Cells Improves Survival in a Mouse Model of Invasive and Metastatic Pancreatic Cancer. *Clinical Cancer Research* 15, 3433-3441.
- Klopp, A.H., Zhang, Y., Solley, T., Amaya-Manzanares, F., Marini, F., Andreeff, M., Debeb, B., Woodward, W., Schmandt, R., Broaddus, R., Lu, K., and Kolonin, M.G. (2012). Omental Adipose Tissue-Derived Stromal Cells Promote Vascularization and Growth of Endometrial Tumors. *Clinical Cancer Research* 18, 771-782.
- Levine, H.A., Pamuk, S., Sleeman, B.D., and Nilsen-Hamilton, M. (2001). Mathematical modeling of capillary formation and development in tumor angiogenesis: penetration into the stroma. *Bull Math Biol* 63, 801-863.
- Lewis, C.E., and Pollard, J.W. (2006). Distinct Role of Macrophages in Different Tumor Microenvironments. *Cancer Research* 66, 605-612.
- Li, C.-Y., Shan, S., Huang, Q., Braun, R.D., Lanzen, J., Hu, K., Lin, P., and Dewhirst, M.W. (2000). Initial Stages of Tumor Cell-Induced Angiogenesis: Evaluation Via Skin Window Chambers in Rodent Models. *Journal of the National Cancer Institute* 92, 143-147.

Li Jeon, N., Baskaran, H., Dertinger, S.K.W., Whitesides, G.M., Van De Water, L., and Toner, M. (2002). Neutrophil chemotaxis in linear and complex gradients of interleukin-8 formed in a microfabricated device. *Nat Biotech* 20, 826-830.

Li, L., Wang, L., Zhang, W., Tang, B., Zhang, J., Song, H., Yao, D., Tang, Y., Chen, X., Yang, Z., Wang, G., Li, X., Zhao, J., Ding, H., Reed, E., and Li, Q.Q. (2004). Correlation of serum VEGF levels with clinical stage, therapy efficacy, tumor metastasis and patient survival in ovarian cancer. *Anticancer Res* 24, 1973-1979.

Macdougall, J.D.B., and McCabe, M. (1967). Diffusion Coefficient of Oxygen through Tissues. *Nature* 215, 1173-1174.

Macklin, P., Edgerton, M.E., Thompson, A.M., and Cristini, V. (2012). Patient-calibrated agent-based modelling of ductal carcinoma in situ (DCIS): From microscopic measurements to macroscopic predictions of clinical progression. *Journal of Theoretical Biology* 301, 122-140.

Mcguire, W.P., Hoskins, W.J., Brady, M.F., Kucera, P.R., Partridge, E.E., Look, K.Y., Clarke-Pearson, D.L., and Davidson, M. (1996). Cyclophosphamide and cisplatin compared with paclitaxel and cisplatin in patients with stage III and stage IV ovarian cancer. *N Engl J Med* 334, 1-6.

Milliken, D., Scotton, C., Raju, S., Balkwill, F., and Wilson, J. (2002). Analysis of Chemokines and Chemokine Receptor Expression in Ovarian Cancer Ascites. *Clinical Cancer Research* 8, 1108-1114.

Mombach, J.C., Glazier, J.A., Raphael, R.C., and Zajac, M. (1995). Quantitative comparison between differential adhesion models and cell sorting in the presence and absence of fluctuations. *Phys Rev Lett* 75, 2244-2247.

Morton, C.I., Hlatky, L., Hahnfeldt, P., and Enderling, H. (2011). Non-stem cancer cell kinetics modulate solid tumor progression. *Theor Biol Med Model* 8, 48.

Nieman, K.M., Kenny, H.A., Penicka, C.V., Ladanyi, A., Buell-Gutbrod, R., Zillhardt, M.R., Romero, I.L., Carey, M.S., Mills, G.B., Hotamisligil, G.S., Yamada, S.D., Peter, M.E., Gwin, K., and Lengyel, E. (2011). Adipocytes promote ovarian cancer metastasis and provide energy for rapid tumor growth. *Nat Med* 17, 1498-1503.

Pugh, C.W., and Ratcliffe, P.J. (2003). Regulation of angiogenesis by hypoxia: role of the HIF system. *Nat Med* 9, 677-684.

Rejniak, K.A., and Mccawley, L.J. (2010). Current trends in mathematical modeling of tumor–microenvironment interactions: a survey of tools and applications. *Experimental Biology and Medicine* 235, 411-423.

Sawada, K., Ohyagi-Hara, C., Kimura, T., and Morishige, K.-I. (2012). Integrin Inhibitors as a Therapeutic Agent for Ovarian Cancer. *Journal of Oncology* 2012.

Schneider, C.A., Rasband, W.S., and Eliceiri, K.W. (2012). NIH Image to ImageJ: 25 years of image analysis. *Nat Methods* 9, 671-675.

Serini, G., Ambrosi, D., Giraudo, E., Gamba, A., Preziosi, L., and Bussolino, F. (2003). Modeling the early stages of vascular network assembly. *EMBO J* 22, 1771-1779.

Shield, K., Ackland, M.L., Ahmed, N., and Rice, G.E. (2009). Multicellular spheroids in ovarian cancer metastases: Biology and pathology. *Gynecologic Oncology* 113, 143-148.

Shirasawa, T., Izumizaki, M., Suzuki, Y.-I., Ishihara, A., Shimizu, T., Tamaki, M., Huang, F., Koizumi, K.-I., Iwase, M., Sakai, H., Tsuchida, E., Ueshima, K., Inoue, H., Koseki, H., Senda, T., Kuriyama, T., and Homma, I. (2003). Oxygen Affinity of Hemoglobin

Regulates O<sub>2</sub> Consumption, Metabolism, and Physical Activity. *Journal of Biological Chemistry* 278, 5035-5043.

Shirinifard, A., Gens, J.S., Zaitlen, B.L., Poplawski, N.J., Swat, M., and Glazier, J.A. (2009). 3D multi-cell simulation of tumor growth and angiogenesis. *PLoS One* 4, e7190.

Shweiki, D., Itin, A., Soffer, D., and Keshet, E. (1992). Vascular endothelial growth factor induced by hypoxia may mediate hypoxia-initiated angiogenesis. *Nature* 359, 843-845.

Sodek, K.L., Brown, T.J., and Ringuette, M.J. (2008). Collagen I but not Matrigel matrices provide an MMP-dependent barrier to ovarian cancer cell penetration. *BMC Cancer* 8, 223.

Strobel, T., and Cannistra, S.A. (1999).  $\beta$ 1-Integrins partly mediate binding of ovarian cancer cells to peritoneal mesothelium *in vitro*. *Gynecologic Oncology* 73, 362-367.

Swat, M.H., Hester, S.D., Balter, A.I., Heiland, R.W., Zaitlen, B.L., and Glazier, J.A. (2009). Multicell simulations of development and disease using the CompuCell3D simulation environment. *Methods Mol Biol* 500, 361-428.

Wang, J.M., Sica, A., Peri, G., Walter, S., Padura, I.M., Libby, P., Ceska, M., Lindley, I., Colotta, F., and Mantovani, A. (1991). Expression of monocyte chemotactic protein and interleukin-8 by cytokine-activated human vascular smooth muscle cells. *Arterioscler Thromb* 11, 1166-1174.

Yamauchi, K., Yang, M., Jiang, P., Xu, M., Yamamoto, N., Tsuchiya, H., Tomita, K., Moossa, A.R., Bouvet, M., and Hoffman, R.M. (2006). Development of Real-time Subcellular Dynamic Multicolor Imaging of Cancer-Cell Trafficking in Live Mice with a Variable-Magnification Whole-Mouse Imaging System. *Cancer Research* 66, 4208-4214.

Yang, M., Reynoso, J., Bouvet, M., and Hoffman, R.M. (2009). A transgenic red fluorescent protein-expressing nude mouse for color-coded imaging of the tumor microenvironment. *J Cell Biochem* 106, 279-284.

Yoneda, J., Kuniyasu, H., Crispens, M.A., Price, J.E., Bucana, C.D., and Fidler, I.J. (1998). Expression of angiogenesis-related genes and progression of human ovarian carcinomas in nude mice. *J Natl Cancer Inst* 90, 447-454.

Yu, D., Wolf, J.K., Scanlon, M., Price, J.E., and Hung, M.C. (1993). Enhanced c-erbB-2/neu expression in human ovarian cancer cells correlates with more severe malignancy that can be suppressed by E1A. *Cancer Res* 53, 891-898.

**Chapter 3: Spatial model of drug delivery route for treatment of disseminated  
ovarian cancer**

Kimberly Kanigel Winner<sup>1,2</sup>, Mara P. Steinkamp<sup>3,5</sup>, Rebecca Lee<sup>5</sup>, Maciek Swat<sup>6</sup>, Yi  
Jiang<sup>7</sup>,  
Carolyn Muller<sup>4,5</sup> Melanie Moses<sup>1,2</sup> and Bridget S. Wilson<sup>\*3,5</sup>

<sup>1</sup> Department of Biology, University of New Mexico, Albuquerque, NM USA

<sup>2</sup> Department of Computer Science, University of New Mexico, Albuquerque, NM USA

<sup>3</sup> Department of Pathology, University of New Mexico, Albuquerque, NM USA

<sup>4</sup> Department of OB/GYN, University of New Mexico, Albuquerque, NM USA

<sup>5</sup> Cancer Center, University of New Mexico, Albuquerque, NM USA

<sup>6</sup> Department of Physics and Institute of Biocomplexity, University of Indiana,  
Bloomington, IN USA

<sup>7</sup> Department of Mathematics and Statistics, Georgia State University, Atlanta GA USA

*Keywords:* ovarian cancer, cellular Potts, cisplatin, pertuzumab

*\*Correspondence:*

*Bridget S. Wilson, MSC08-4640, Cancer Research Facility, Room 201, University of New Mexico Health Sciences Center, Albuquerque, NM 87131-0001, USA.*

*e-mail: bwilson@salud.unm.edu*

*^ Kimberly Kanigel Winner and Mara P. Steinkamp have contributed equally to this work.*

Prepared for submission to *Frontiers in Oncology*



## ABSTRACT

In ovarian cancer, metastasis is typically confined to the peritoneum. Surgical removal of the primary tumor and macroscopic secondary tumors is a common practice. More effective strategies are needed to target microscopic spheroids that persist in the peritoneal fluid after debulking surgery. To treat this residual disease, therapeutic agents can be administered by either intravenous (IV) or intraperitoneal (IP) infusion. We use a cellular Potts model to compare tumor penetration of two classes of drugs when delivered by these two alternative routes. We model cisplatin, representative of small molecule chemotherapeutic agents that penetrate cells and vessels readily. We also consider delivery of therapeutic monoclonal antibodies, such as pertuzumab that targets ErbB2 receptors expressed on ~35% of ovarian tumors. Experimental measurements included fluorescence recovery after photobleaching (FRAP) to measure penetration of non-specific antibodies infiltrating into cultured human ovarian cancer (SKOV3.ip1) spheroids and two-photon imaging of spheroids and explanted tumors from orthotopic xenografts in nude mice. Stereology analysis was used to estimate the range of vascular densities in disseminated tumors from patients. The model considers both the primary route when drug is administered IV or IP, as well as the subsequent exchange into the other delivery volume as a secondary route. By accounting for these dynamics, the model shows that IP delivery is the markedly better route for small, avascular tumors typical of patients with ascites. Small tumors attached to peritoneal organs, ranging from vascularity of 2-10%, also show superior drug delivery via the IP route even though

tumor vessels can act as sinks during the dissemination of small molecules. Wave fronts of antibody binding are observed both *in silico* and in *in vivo*, indicating that optimization of antibody delivery is an important criteria in the efficacy of these and other biologic therapeutics. Use of both delivery routes may provide the best total coverage of tumors, particularly when there is a significant burden of avascular spheroids suspended in the peritoneal fluid as well as larger, neo-vascularized secondary tumors.

## INTRODUCTION

Ovarian cancer is the tenth most common and sixth most deadly cancer in the United States <sup>1</sup>. Because it is largely asymptomatic during the early stages of disease, 61% of patients present with cancer already disseminated throughout the abdominal cavity. As a consequence of late-stage diagnosis, the five-year survival rate is only 44% <sup>2</sup>. Intraperitoneal (IP) administration of cisplatin has been shown to correlate with improved overall survival <sup>3-5</sup> and combined IV/IP chemotherapy has been recommended by the National Cancer Institute as the standard of care for optimally-debulked, FIGO stage 3 ovarian cancer patients <sup>6</sup>. In this work, we explore the effectiveness of IP vs IV therapy for residual disease as a function of attachment and vascularity. We predict that improved outcomes may result from pathologic assessment of peritoneal tumor characteristics after cytoreduction, potentially leading to individualized decisions on the routes of drug administration. We tested this hypothesis through simulations delivering both small molecule and antibody therapies, using a spatially discrete, cellular automaton computational model.

Disseminated ovarian tumors often exist as two distinct types: 1) avascular cell aggregates (“spheroids”) that are loosely attached to organs within the peritoneal cavity or free floating in the ascites fluid and 2) vascularized tumors colonizing peritoneal organs. For optimal treatment, drugs must be effective against both types of tumors. Furthermore, route of drug delivery will likely have an effect on drug penetration, binding and accumulation. We focus here on strategies for post-surgery treatment of

microscopic residual tumors, where debulking has removed both the primary tumor and larger secondary tumors (>1 cm in diameter).

Drug movement between the peritoneal and the blood plasma compartments is a key feature of the pharmacokinetics affecting abdominal tumors. In healthy individuals, the volume of peritoneal fluid is small (10-30ml). This fluid resides in the interstitial spaces and is secreted by mesothelial cells [reviewed in <sup>7</sup>]. The fluid circulates through the cavity and enters the blood circulation via adjunct capillaries (40-50%) or stomata on the underside of the diaphragm. The stomata can admit particles up to 25  $\mu\text{m}$  in diameter into the diaphragmatic lymphatics, which connect to the greater lymphatic system. Fluid ultimately drains back into the venous circulation. Because the blood and intraperitoneal compartments are intimately connected, our model accounts for the initial drug infusion into the primary peritoneal or blood compartment as well as the delayed appearance of drug into the secondary compartment.

Mathematical modeling of drug delivery was pioneered in the 1960s<sup>8</sup>. Recent reviews have summarized current strategies used to model anti-cancer drug penetration at different temporal and spatial scales<sup>9,10</sup>. Of particular note, Sinek *et al.* created a 2-dimensional multi-scale model of cisplatin and doxorubicin intravascular delivery<sup>11</sup>. For ovarian cancer, mathematical models have addressed the penetration of doxorubicin through multiple cell layers<sup>12</sup>, the effects of transcriptional and regulatory networks<sup>13-15</sup>, long-term recurrence predictions and prognostic value of CA-125<sup>16-18</sup> or other novel markers<sup>19,20</sup> detected in blood, assessment of diagnostics and prognostics<sup>21-26</sup>,

effectiveness of theoretical or established treatments<sup>16,27-30</sup> and survival rates of patients after surgical or drug treatment<sup>31</sup>. The metabolic and spatial characteristics of cancer cell spheroids have been considered<sup>32</sup>, including studies of ovarian cancer spheroids<sup>33</sup>.

Few spatially explicit models of ovarian cancer exist aside from our own<sup>34</sup>. Giverso *et al.* built a 2-dimensional cellular Potts model of ovarian cancer that explores the interaction of ovarian cancer cells with the mesothelial layer and underlying extracellular matrix during invasion<sup>35</sup>. More common are models of drug penetration in the peritoneal cavity. El-Kareh *et al.* modeled the penetration distance of cisplatin into the rat peritoneum with and without hyperthermia<sup>36</sup>. This model and others, as well as experimental measures for penetration into tissues in the peritoneal cavity, suggest absorption of small-molecule drugs by vessels can be a barrier to drug delivery<sup>37</sup>. Here, we report results of a 3-D spatial model of drug delivery. Based upon the CompuCell3D cellular Potts simulation environment, the model was parameterized for ovarian cancer spheroid behavior and drug dynamics for two delivery compartments<sup>34</sup>. Results show that, for avascular spheroids and small, vascularized tumors in the process of seeding peritoneal organs, the IP route is superior for drug delivery.

## **METHODS AND MATERIALS**

### **DRUG PENETRATION INTO SPHEROIDS**

2000 SKOV3.ip-GFP cells were seeded into each well of a Lipidure-coated 96 well plate and incubated for 48 hours to allow the formation of spheroids. Pertuzumab was

conjugated to Pacific Blue 410 succinimidyl ester (Life Technologies). Spheroids were incubated in pertuzumab-Pacific Blue at a final concentration of 3.5  $\mu\text{g/ml}$  and imaged on a Leica 510 confocal microscope with a META detector.

## **OVARIAN CANCER XENOGRAFT MODEL**

Details of the human xenograft model in Nu/nu mice were previously described<sup>34</sup>. In brief, nude mice were engrafted by IP injection with 100  $\mu\text{l}$  of a single cell suspension containing five million SKOV3.ip1 cells expressing GFP. Tumors develop within 1-3 weeks. Where specified, recipient mice were injected with 20mg/kg perzutumab; antibody was purchased from UNM Pharmacy and conjugated to Pacific Blue per manufacturer's guidelines (Life Technologies, Grand Island NY). Mice were humanely sacrificed after specified time intervals. Tumors were excised and imaged on a Zeiss 510 confocal microscope equipped for 2-photon imaging. All experiments using mice were approved by the UNM Animal Care and Use Committee, in accordance with NIH guidelines for the Care and Use of Experimental Animals.

## **QUANTIFICATION OF VASCULATURE DENSITY AND VESSEL DIAMETER IN PATIENT TUMORS**

Specimens from ten ovarian cancer patients were obtained from the UNM Human Tissue Repository. Patient samples were identified for which both bowel and omentum were available. Adjacent sections were stained with H&E to identify higher-chromatin tumor cells or processed for immunohistochemistry (IHC) with anti-CD31 antibodies (BD

Biosciences, San Jose, CA) to identify endothelial cells. Confocal montages of each specimen were generated using Stereo Investigator image analysis software at 4x magnification. A board-certified pathologist distinguished tumor tissue from other tissues and drew contours of tumor tissue on a printed contact sheet of the section montages. The contours were re-drawn at 20x using Stereo Investigator and the confocal microscope to set a probe area. Vessel area density was calculated using the Stereo Investigator Area Fractionator Probe with sampling grids tailored to each of the 18 samples. Grid points were counted as vessel if the triangle defined by the upper right-hand quadrant of “cross-hairs” contained pixels darkly stained for CD-31. Structure of the overall tissue and relative darkness of stain were taken into account. A minimum of 200 points in the sub-region (vessel) provides best probe coverage; where this coverage was not achieved, the sample was reprocessed over a different coverage area in the grid. Additional controls avoided re-analysis of overlaid areas or analysis of tissue of poor quality. Vessel diameter was calculated using Stereo Investigator Line Measure or Circle Measure tools. Multiple vessels (10-20) were chosen per tumor and 3-5 vessels were measured per quadrant (236 vessels measured in 18 tumors).

## **CELLULAR POTTS MODEL**

The cellular Potts model of ovarian cancer was initially developed for dynamic simulations of cell growth, migration and response to chemical fields. Here, the model is reduced to a cellular automaton and penetration model with no growth or motility. Each cell is considered a single agent, occupying one voxel on a 3-dimensional lattice. In

CompuCell3D, lattices representing chemicals are layered onto the cellular lattice. The amount of chemical accumulated by each cell is reported at each time step.

For a chemical concentration  $C_I$ , the effective diffusion coefficient ( $D_{CI}$ ), decay ( $\gamma_I$ ), source ( $\alpha_I$ ), and sinks ( $\zeta_I$ ) in the PDE solvers in CC3D are described by:

$$\frac{\partial C_1}{\partial t} = D_{C_1} \nabla^2 C_1 - \gamma_1 C_1 + \alpha_1 [1 - \delta(\tau(S), vessel)] - \zeta_1 [1 - \delta(\tau(S), tumor)]$$

For the concentration of each drug in blood plasma after IV delivery, or intraperitoneal fluid after IP delivery, at each time step, we use a constant concentration in the vessels (constant boundary condition) as fitted to patient data (Table 1). Antibody available at the vessel surface is described by

$$C_{VesselSurface}(t) = C_{Plasma}(t) * B$$

where  $C_{plasma}$  is the concentration in blood,  $t$  = time, and  $B$  = the Biot number. The Biot value is the ratio of capillary extravasation to the free diffusion coefficient in tumor tissue, an approach pioneered by Thurber<sup>37-39</sup> to address passage of proteins across the vascular wall as the rate-limiting step of delivery.

Our simulation environment represents small tumors of 30 cells in diameter (volume =13,997 cells), suspended in peritoneal fluid or attached to the thin mesentery where most of the tumor surface is exposed to fluid. Drug infusion (5-15 min, as specified in figure legends) was delivered from intratumoral vessels or the peritoneal cavity.



Simulation volume was 35,937 ( $33^3$ ) voxels. Each vascular tumor contained a simulated vascular meshwork generated in Matlab by randomly placed cylinders of specified radii and lengths.

One voxel's volume was equivalent to one SKOV3.ip1 cancer cell, or  $179.4 (5.64^3) \mu\text{m}^3$ <sup>34</sup>. One time step was equivalent to 1/1500 real minutes in cisplatin models, and 1/1132 hrs in pertuzumab models. Each Monte Carlo Step (MCS) was then equal to the time for molecules to diffuse the distance of one cell diameter for each drug.

We implement drug modeling simplification guidelines outlined by Thurber, which considers only the primary rate-limiting step for drug diffusion in tumor tissue as determined by the molecular weight, shape, and lipophilicity of a drug<sup>39</sup>. For easily penetrating, low-molecular-weight cisplatin, there are no explicit barriers within blood or tissue in the model. Penetration of antibody from the IP fluid into tumor tissues is considered a passive process, parameterized from our own FRAP measurements, as well as *in vivo* effective penetration lengths<sup>39</sup>, rather than accounting for discrete pressure or convective velocity of the interstitial fluid.

Fits for drug concentrations in the primary delivery compartments were derived from patient data in the literature (Table 1). Optimal fits were based on the best R-square statistics, plots of residuals, and knowledge of the biological system's behavior. All plots were >0.8 R-square, and most were >0.95. Primary compartment concentration was calculated for the time step from the fit, and set as a constant concentration (constant

boundary condition) in either the intraperitoneal fluid or the blood. Simultaneous drug concentration in the secondary compartment was also included. Data for simultaneous IP and IV concentrations during drug delivery in human patients (cisplatin) and rats (IgG) were extracted from plots found in the literature, and used to calculate the ratios of IP to IV concentration after IV delivery, or IV to IP concentration after IP delivery (see Figure 3). The concentration in the secondary compartment was calculated as the product of the fit for the ratio at the current time step, multiplied by the current concentration in the initial delivery compartment, and then set as a constant concentration (constant boundary condition) in the fluid of the secondary compartment for the duration of the time step. For instance, for each time step during IV delivery of cisplatin ( $t = \text{mins}$ ):

$$[IP_{post-IV}(t)] = [IV(t)] * (-1.154E - 06 * t^3 + 5.737E - 04 * t^2 + 0.09922 * t + 5.973)$$

The accumulation of drug in each cell was recorded in a text file during each simulation, and plotted and analyzed in Matlab.

## **MODELING TUMOR VASCULAR NETWORKS**

Vascular radii from the ovarian cancer tumor samples were characterized by fitting a Gaussian distribution to vessels with radii ranging from 1 to 40  $\mu\text{m}$  (this excluded a small number of larger vessels that were rarely present in the small tumors we model here). The resulting distribution had a mean of 19.22 $\mu\text{m}$  and standard deviation of 11.2 $\mu\text{m}$ .

We integrated these values into our cellular Potts model by discretizing values to voxel dimensions, resulting in vessels 1 to 3 cells in diameter. A Matlab script generated a randomized distribution of vessels with these radii within spheroids of 13,997 cells. The distributions were designed to generate variable vascular area corresponding to the variation we observed empirically in tumor samples. We generated in simulated tumors in which central slice varied from 0 to 10% vascular area. Figure 2H illustrates this important feature of our simulation strategy.

## **RESULTS**

### **DRUG PENETRATION AND ACCUMULATION IN AVASCULAR TUMORS**

In Figure 1, we first experimentally consider drug delivery to avascular, three-dimensional cancer cell aggregates by passive penetration. SKOV3.ip1 ovarian cancer cells were grown as spheroids (~2000 cells), incubated for defined intervals with fluorescent small molecules or antibodies and then imaged by confocal microscopy. Naturally fluorescent doxorubicin (MW 543 Da) was used to represent the class of low molecular weight, highly lipophilic chemotherapeutic compounds; it is used here as a surrogate for the behavior of cisplatin (MW 300 Da), a first line therapy for ovarian cancer. Results for doxorubicin are shown in Figure 1A, where the fluorescence intensity plot below the 10 minute image shows the drug well distributed across the spheroid. Note

that the fluorescence intensity continued to rise over the incubation period of 90 min, attributed to drug accumulation in cell nuclei as doxorubicin intercalated into DNA. The data are consistent with the fast penetration of small molecular weight drugs in tumors<sup>40</sup>. These results validate the use of a fast diffusion rate for cisplatin ( $640 \mu\text{m}^2/\text{sec}$ ;<sup>41</sup>) in our simulations.

We next experimentally evaluated the uptake of therapeutic antibodies into cultured spheroids. The passive diffusion coefficient for these large proteins (~150 kDa) was determined by Fluorescence Recovery after Photobleaching (FRAP). The spheroids were incubated with fluorescently-tagged, non-specific IgG for one hour. As shown in Figure 1B, this is a sufficient period for IgG to diffuse through the intercellular spaces to the spheroid interior. A  $14 \mu\text{m}$  diameter spot was photobleached and diffusion of fluorescent antibodies within the interstitial space in the absence of binding was estimated based upon fluorescence recovery. As shown in Figure 1C, an estimated diffusion coefficient of  $13 \mu\text{m}^2/\text{sec}$  for non-specific IgG was comparable to that of control (70kDa dextran). We interpret this as evidence that the cell-cell junctions in these spheroids are insufficient barriers to strongly limit protein penetration. Moreover, these values are consistent with *in vivo* estimates of antibody diffusion in tumor tissues by others<sup>42,43</sup>.

Figure 1

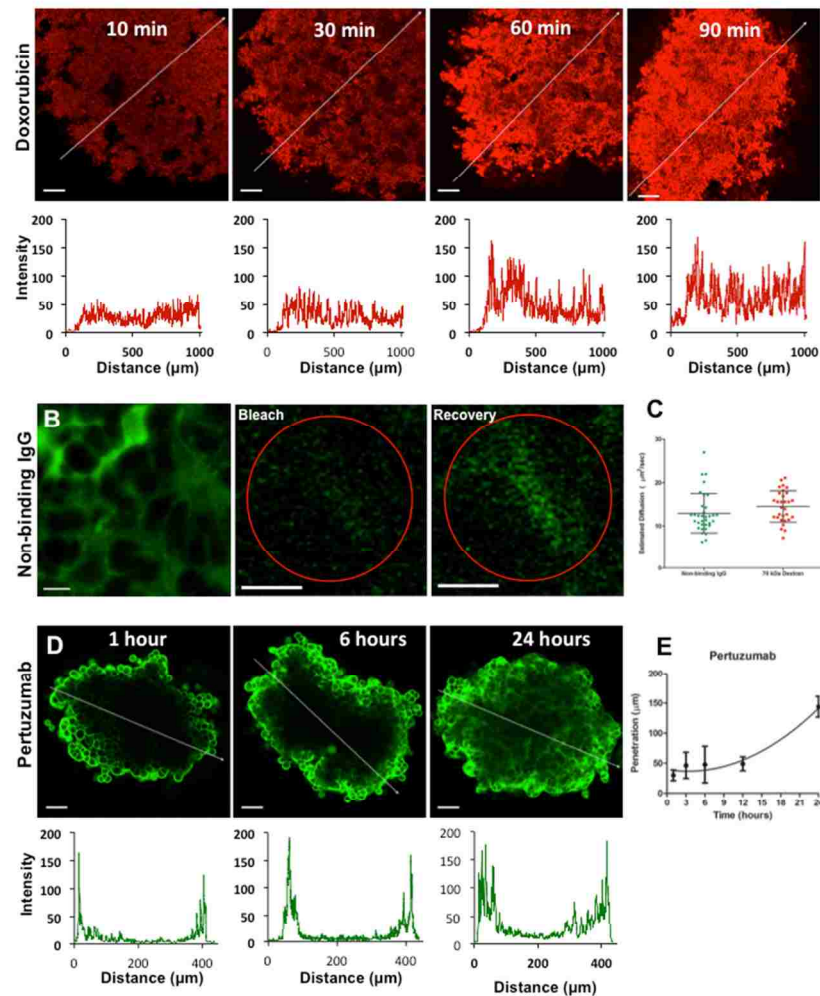


FIGURE 1. Diffusion in Spheroids. A) SKOV3.ip1-GFP spheroids of  $\sim 2000$  cells were incubated with 3.5  $\mu\text{g/ml}$  doxorubicin for 10-90 minutes as shown. Graphs below confocal images indicate fluorescent intensity measured across the spheroid along the specified line (white arrow). B) SKOV3.ip1-RFP spheroids were incubated with 350  $\mu\text{g/ml}$  non-binding FITC-conjugated IgG for 1 hour to allow homogeneous distribution of the IgG throughout interstitial spaces in the spheroid. Regions of interest were bleached (red circles) and fluorescence recovery was measured over time. The rate of recovery of fluorescence ( $\tau$ ) was determined by single component fitting of FRAP curves. C) Graph of diffusion estimated from  $\tau$  based on the radius of the circular ROI. Diffusion was estimated for non-binding IgG in the spheroids. Diffusion of IgG in the spheroid was comparable to that of 70 kDa FITC-Dextran. D) SKOV3.ip1-RFP spheroids were incubated with 3.5  $\mu\text{g/ml}$  Alexa488-conjugated pertuzumab for 1-24 hours, washed, and imaged live. Graphs indicate fluorescence intensity across the spheroid along the specified line (white arrow). E) Penetration depth of ErbB2-binding antibody (pertuzumab) measured in 2 or more spheroids per time point.

Next, the penetration of specific antibody was evaluated by incubating spheroids with subclinical levels (3.5 $\mu$ g/ml) of Alexa 488-conjugated pertuzumab that binds ErbB2 abundantly expressed on the surface of SKOV3 cells. Note that ErbB2 expression is a feature of only ~35% of ovarian tumors<sup>44</sup>; it is reasonable to assume that our results should apply to antibodies directed at other surface receptors on ovarian tumor cells, such as ErbB3 and MET<sup>44</sup>. Images in Figure 1D and accompanying intensity plots show that there is a “wave front” of antibody binding as it penetrates into the tumor spheroid. Under these conditions, saturation of antibody binding is not achieved within the center of the spheroids even following an incubation period of 24 hours (Fig. 1E). Based upon these data, the effective penetration rate of antibodies with high affinity for tumor surface antigens is three orders of magnitude slower than predicted based upon non-specific antibody diffusion. One of the intents of our model is to explore the relationship between binding rates, antibody concentration and tumor penetrance.

## **VESSEL DENSITY OF HUMAN OVARIAN TUMORS AS PARAMETERS FOR MATHEMATICAL MODELING**

Vascularization of tumors will also affect drug penetration. The range of vascular densities was evaluated by immunohistochemistry methods for disseminated ovarian tumors from nine cancer patients. Samples were stained with anti-CD31 antibodies as a vascular endothelial cell marker. For each patient, paired samples of omentum and bowel

metastases were evaluated. As shown in Figure 2, vessel density in these samples was measured and reported as percent of total area. The mean value was 4.80%, with a range of 2 to 10%. Measurement of vascular size gave a mean diameter of 19.2  $\mu\text{m}$  with a range from 5.4 to 135.4  $\mu\text{m}$ . This data is similar to that reported for xenograft models<sup>45-47</sup>

Figure 2

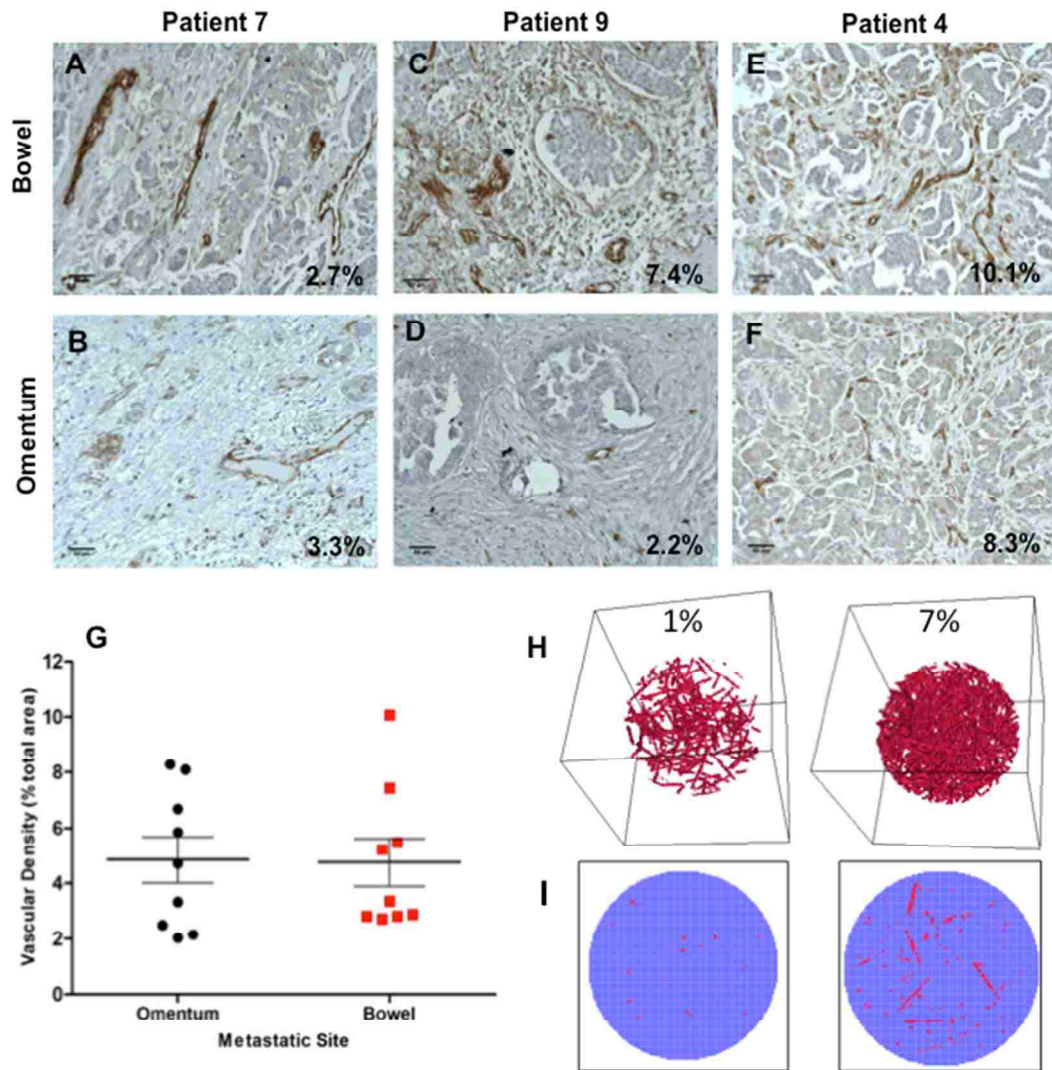


FIGURE 2. Measured vascular density in patient bowel and omentum tumors as parameters for simulation. Sections of matched bowel and omentum metastases from 9 ovarian cancer patients (UNM Human Tissue Repository) were labeled with anti-CD31 antibody (brown) to detect vascular endothelial cells. A,B) Low-vascular-density sections (4  $\mu$ m thick) from bowel (A, 2.8% vessel area) and omentum (B, 3.3%) of patient 7. C,D) Variable-vascular-density sections from bowel (C, 7.4%) and omentum (D, 2.2%) of patient 9. E,F) High-vascular-density sections from bowel (E, 10.1%) and omentum (F, 8.3%) of patient 4. G) Average vascular density (% area) is comparable in omentum (4.847%) and bowel (4.753%). H) Matlab-based simulation of vascular tree in a 65-cell-radius spheroid generating 1% and 7% vascular area (I) in the spheroid central plane.



## **SCHEMATIC OF THE MODELING APPROACH**

The flow chart outlining the integration of experimental and modeling results in this work is summarized in Figure 3. A critical aspect of the model is that, once drugs are administered by intravenous or intraperitoneal routes, there is a secondary accumulation and transient delivery in the other compartment. Our parameters for exchange of cisplatin between the two compartments are based on results of Casper et al, who measured concentrations of platinum in plasma and ascites after administration of cisplatin by either route<sup>48</sup>. The time course reproducing fits of these parameters in our model are plotted in Figure 3 (Pharmacokinetics Box). The time courses for levels of antibody in these compartments, when introduced by either route, were fit to data from Pai and colleagues<sup>49</sup>, as well as FDA document (#125409) on pertuzumab<sup>50</sup>. As indicated in the flow chart, the model also explicitly integrates measured levels of vascularity (Figure 2), as well as measured parameters for penetration, binding and cellular accumulation as listed in Table 1 and references therein.

Figure 3

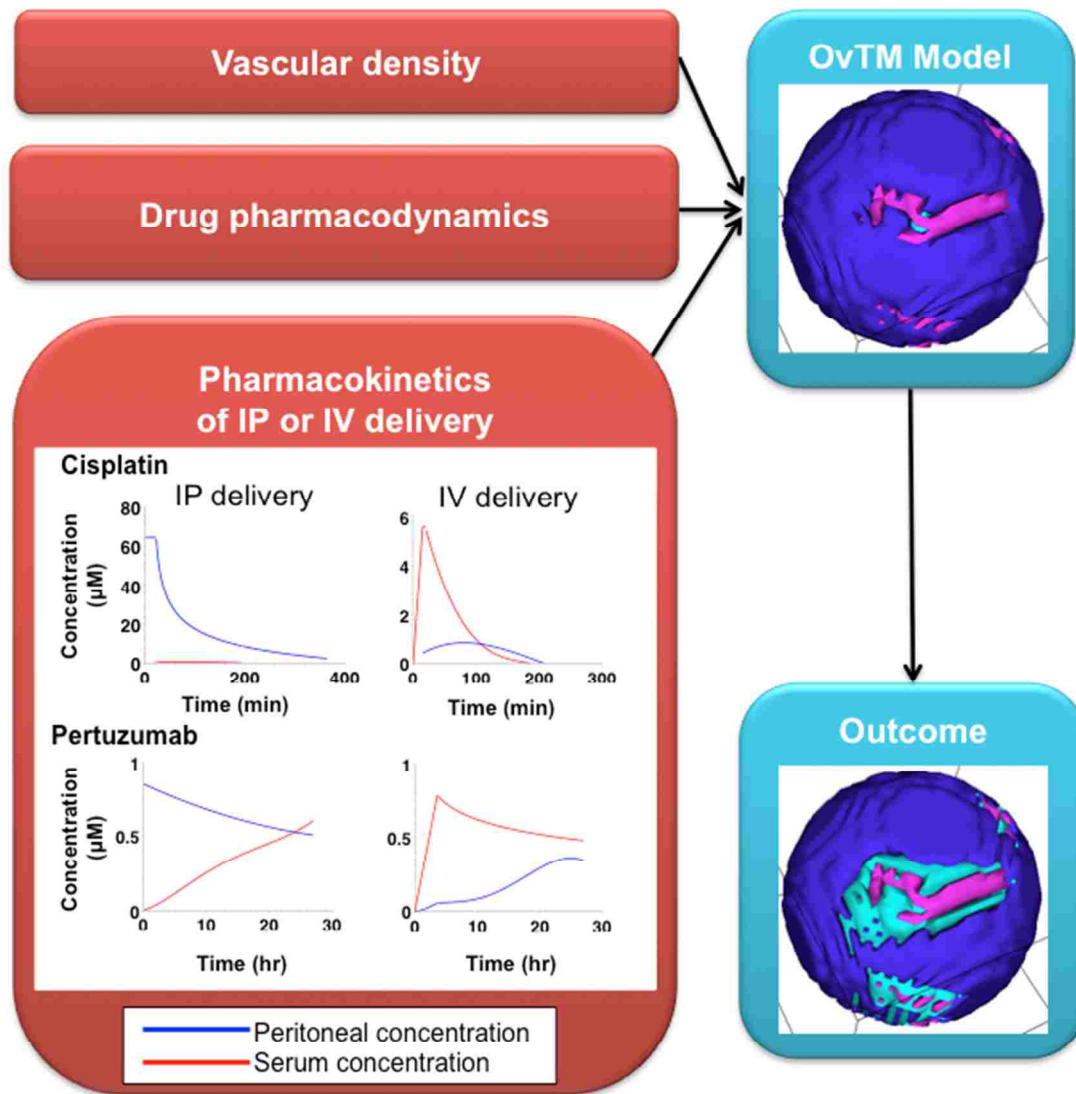


FIGURE 3. Flow chart of drug delivery model inputs and output. The 3-D OvTM model integrates pharmacodynamic data, tumor vascular densities, and in vivo pharmacokinetic time course data from clinical and experimental studies. Pharmacokinetic data shown are fits of cisplatin concentrations in the serum and peritoneal compartments during and after IP (left) or IV infusion (right) [45] (top) and fits of pertuzumab concentrations after IP dosing from the peritoneal fluid (left), and IV infusion (right). Available pertuzumab from the blood is shown before accounting for the vascular endothelial barrier (concentration is scaled with the Biot number; see Methods). IP and IV doses are 5mg/kg. IP antibody concentration time course was calculated as 1446 times the fit for an IP-delivered immunotoxin conjugate administered at 5ng/kg [46].

## **CISPLATIN ACCUMULATION IN TUMOR CELLS AFTER IP OR IV DELIVERY IS INFLUENCED BY VASCULAR DENSITY**

In Figures 4 and 5, we present results for cisplatin uptake in this model. Cellular accumulation of drug was compared, using route of delivery and vascularity as variables. Results are expressed in molecules cisplatin/cell. Note that prior work estimated the IC50 for cellular cytotoxicity to be  $\sim 5.6 \times 10^6$  cisplatin molecules/cell<sup>51</sup>. In order to reach this level, cultured cells were exposed to 38  $\mu\text{M}$  cisplatin for 2 hrs. Importantly, this provides a target level of drug accumulation to be achieved in our cell-based tumor model.

Simulation conditions began with infusion of cisplatin by either route for 15 minutes (total 60 mg/m<sup>2</sup>), followed by tracking of drug accumulation until cisplatin levels in both compartments dropped to negligible levels ( $\sim 180$  min). Figure 4 reports results for avascular spheroids with a 30 cell diameter ( $\sim 14,000$  cells). Results show that, for the same drug dose, the IP route is clearly superior. Direct infusion of cisplatin in the peritoneum at this dose results in substantial and uniform drug levels across the avascular tumor (Figure 4A), reaching a predicted level of almost 5.7 million molecules/cell (Figure 4B, inset).

Figure 4

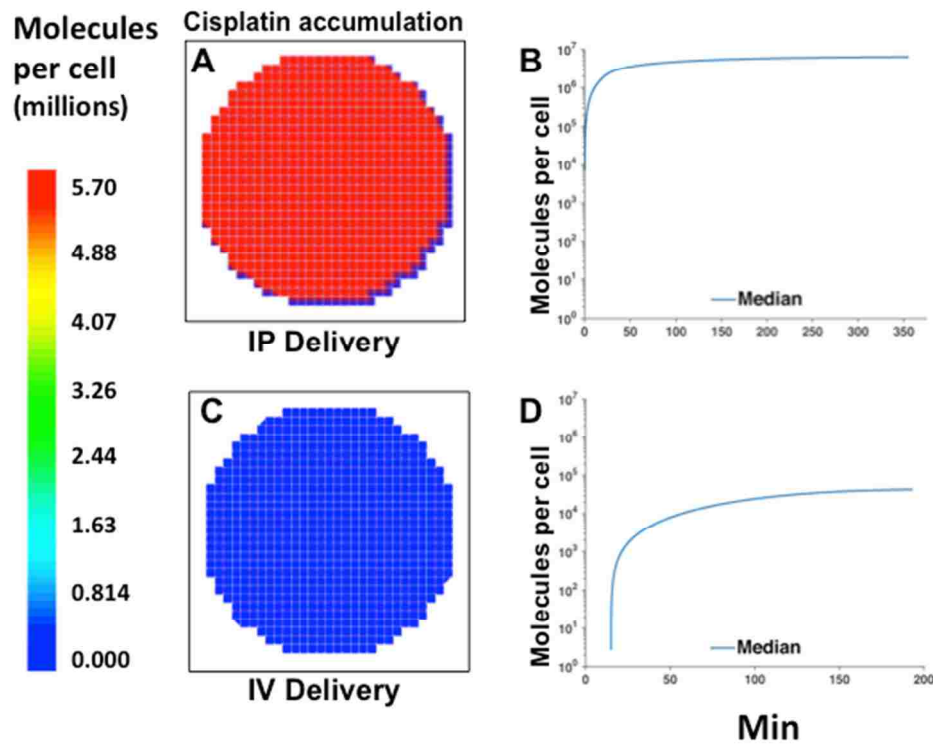


FIGURE 4. Simulation of cisplatin accumulation in avascular spheroids of  $\sim 14,000$  cells. A,B) Intravenous delivery of  $60 \text{ mg/m}^2$  (diluted by blood volume,  $\sim 5\text{L}$  per female patient). C,D) Intraperitoneal delivery of  $60 \text{ mg/m}^2$  (diluted by  $\sim 1060\text{ml}$  saline). A,C) Central cross-sections of 3-D simulations of IV (A) or IP (C) delivery of  $60\text{mg/m}^2$  cisplatin to a  $0.01\text{mm}$  avascular tumor (30 cells in diameter) show marked differences in accumulation. B,D) Plots of minimum, maximum, and median report accumulation of drug over time, expressed in molecules per cell. Where max and min are small, only the median plot line is visible.

In contrast, intravenous delivery of cisplatin is predicted to have poor response. In this case, cisplatin reaches the avascular tumor solely by secondary delivery to the peritoneal fluid. Cellular accumulation is very low (Figure 4C,D), peaking at estimates of ~42,000 cisplatin molecules/cell. There is again little cell-cell variability in drug uptake in this avascular setting. Importantly, cisplatin delivery to avascular tumors via the IV route results in accumulation far below the IC50 value.

Plots in Figure 5 report results for cisplatin accumulation in the same tumor volume, but with vascular densities of either 2% or 10%. Despite the advantage of vessels for entry of drug from the blood, the IP route is again superior for these small tumors (Figure 5A,E). The cell-to-cell variability of cisplatin accumulation in vascularized ovarian tumors is one of the most striking results of these simulations. The uptake of drug is highly heterogeneous, as indicated by the large spread around the mean values plotted in each case. The marked spatial gradients in drug accumulation following IP delivery to vascularized tumors (Figure 5A,E) is surprising. As accompanying plots in Figure 5B,F show, accumulation across the tumor is much less uniform than for the same size of avascular tumor (Figure 4). This result indicates that vessels are a sink for drug when cisplatin is infused directly into the peritoneum. The inverse relationship between the vascular density of the tumor and IP delivery of drug may be an unappreciated factor in chemotherapy regimens.

Figure 5

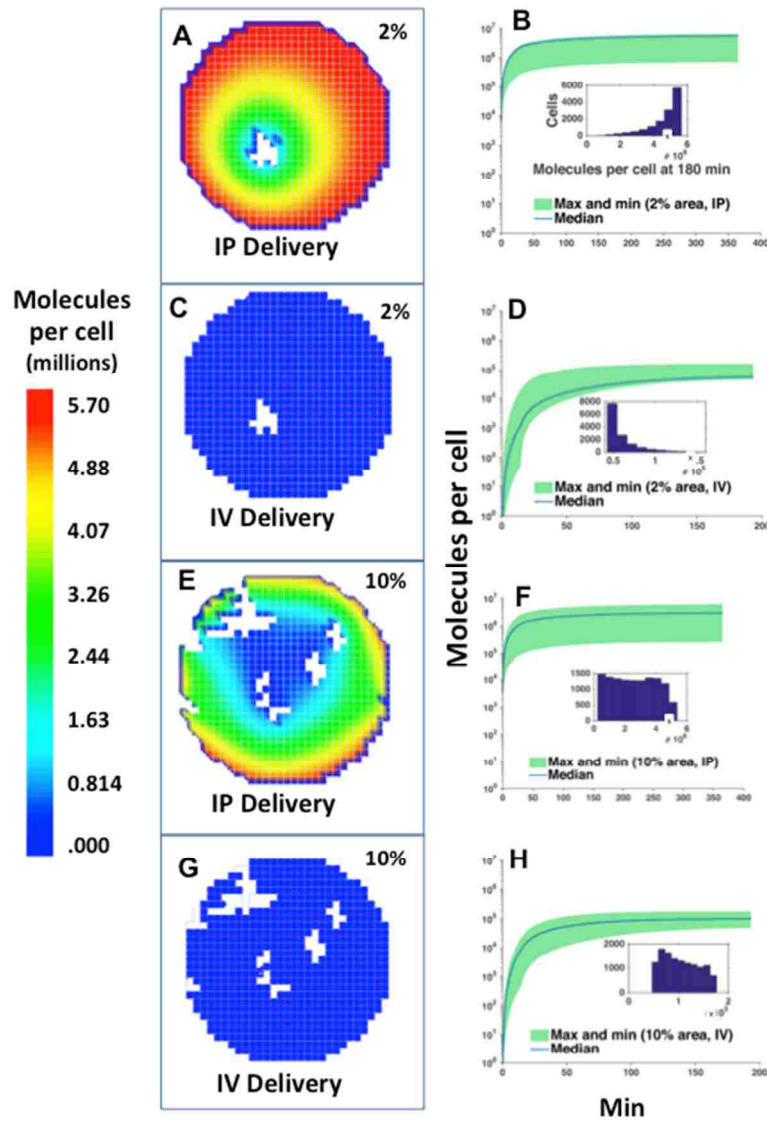


FIGURE 5. Heterogeneity of cisplatin accumulation is increased during IP and IV delivery to small, vascularized tumors. A-F) Time courses of median, minimum and maximum drug accumulation in 0.01mm tumors with either 2% or 10% vascular density, as indicated by labels. The simulation totals 12,000-13,000 cells (slightly fewer than Figure 4 due to voxels occupied by vascular elements). Intraperitoneal delivery was 60 mg/m<sup>2</sup>, diluted by ~1060ml of saline; intravenous delivery was also 60 mg/m<sup>2</sup>, diluted by blood volume of ~5L per female patient. *Insets*: Distribution of accumulated cisplatin, showing heterogeneous accumulation across cells in the vascularized tumors at 180 minutes. Color panels represent central cross-sections of 3-D simulations of IP or IV delivery, with the color bar at left indicating scale.

As shown in Figure 5D, IV drug delivery to the 2% vascular tumor accumulates a median value (solid blue line) of only ~40,000 molecules per cell. As shown by the green shading, accumulation can reach up to 140,000 molecules, which occurs in the cells nearest the vessels. For the 10% vascular tumor, these values reach a median of ~90,000 molecules/cell, with a range of 50,000-180,000. This represents only a small improvement in delivery to the tumors over the avascular tumor (compare plots in Figure 4D and Figure 5H).

## **INTRAPERITONEAL DELIVERY OFFERS ADVANTAGES FOR THERAPEUTIC ANTIBODIES**

Therapeutic antibodies have evolved as critical options for the targeted treatment of cancer<sup>52</sup>, motivating our inclusion of these high molecular weight biologics in our model. *In vivo*, the passage across the vascular endothelium is the first step to intravenous delivery of antibody. In the model, this is represented by the Biot value (see Appendix)<sup>38</sup>. Effectively, this translates to an available pool of IgG that is only 2% of that inside the vessel. This applies equally to circulating antibody that is introduced by either primary infusion or secondary exchange from the peritoneum. Other important considerations include the affinity and expression levels of target receptors in the tumor tissue. SKOV3 cells express over 2 million ErbB2/Her2 receptors per cell; the affinity of pertuzumab for ErbB2 is 9.1 nM (Table 1).

Results in Figure 6 show predictions from the model for clinically-relevant doses of pertuzumab (5 mg/kg), when administered by either IP (top) or IV (bottom) routes. For the case of IP delivered antibody, simulation parameters were fit to the data of Pai et al.<sup>49</sup>, where infusion of 1 liter saline was followed by a 50ml injection of antibody and a second infusion of saline. For the case of IV delivered antibody, parameters were fit to data in FDA bulletin 125409, with an infusion period of 3 hours<sup>50</sup>.

Results of simulations in Figure 6 show the early appearance of a wave front of antibody binding (red). Peritoneal delivery to both the avascular tumor in Figure 6A or the 2% vascular tumor in Figure 6B results in a rapidly advancing front and saturation of receptors within 0.4 hr. Note that the wave front is faster than experimental results in Figure 1 with subclinical doses of antibody, as expected for the higher clinical dose. For the 10% vascular tumor, some heterogeneity is seen near the center of the tumor, which is attributed to physical barriers of vessels that block antibody penetration within the tumor geometry. The median values for each of these simulations is plotted at right.



Figure 6

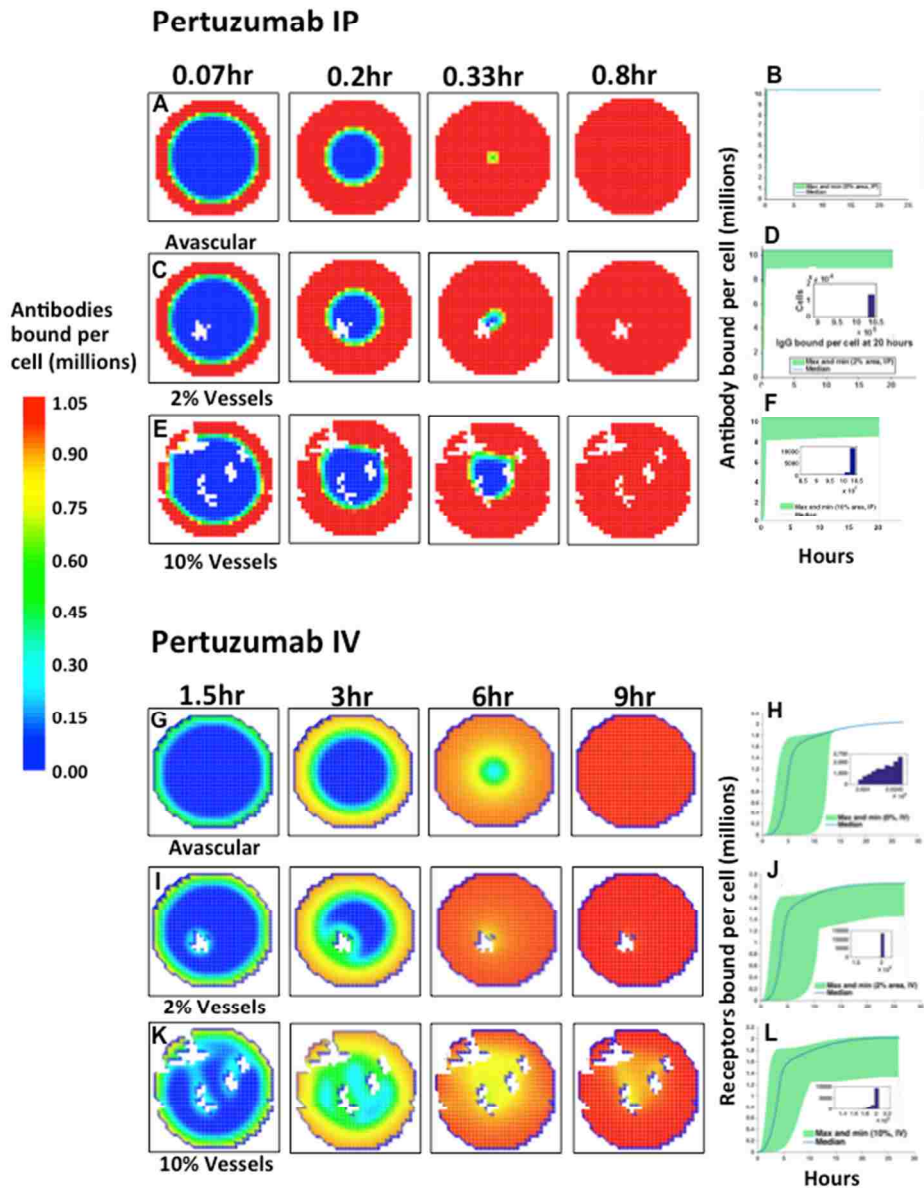


FIGURE 6. Antibody binding exhibits “wave front” behavior when administered by either IV or IP route. As labeled, binding of antibody within 0.01mm tumors (avascular, 2% vascular density or 10% vascular density) is compared for IP and IV delivery (A,C,E,G,I,K). Reflecting the faster accumulation values, IP delivery is reported for multiples of 4.2 min in a 0.8 hour simulation. Simulated IV delivery is shown over 1.5-9 hours. Simulated IP delivery of pertuzumab predicts at least 2-fold improvement over IV route. B,D,F,H,J,L) Plots of minimum, maximum, and median accumulation over time, expressed as antibody bound bivalently to receptors per cell. A,C,E) Intravenous delivery of  $5 \text{ mg/m}^2$  (diluted by blood volume,  $\sim 5\text{L}$  per female human). G,I,K) Intraperitoneal delivery of  $5 \text{ mg/m}^2$  (diluted by  $\sim 2050 \text{ ml}$ ). *Insets*: Distribution of antibody bound bivalently to receptors in all tumor cells at 20 or 24 hours.

As shown in Figure 6D-F, simulation results for IV infusion of antibody are particularly striking and highlight the limitations of antibody transport across normal endothelium, represented by the low Biot number<sup>39</sup>. Under these stringent conditions, there is a marked delay in antibody binding, with the wave front initiating at the border of the spheroid. This indicates that most of the antibody entering the tumors comes from the intraperitoneal fluid, having arrived there after exchange from blood. Half-maximal saturation is seen many hours after IV introduction of drug. Even in the tumors with 2% and 10% vascularity, there is negligible contribution from antibody entering the tissue via vessels. Plots to the right demonstrate that vascularized tumors have much greater heterogeneity in antibody binding.

Since vessels in tumors are often “leaky”<sup>53</sup>, we considered it important to report results of simulations with a higher Biot value based on experimental evidence<sup>54,55</sup>. For IV delivery of antibody, increasing the Biot number by 3.5 or 10 fold resulted in a proportional improvement in accumulation rate (Figure 7). Saturation of all cells occurred at 4 or 3.25 hours respectively compared to 20 hours with normal vasculature. However, even with leaky vasculature, IV delivery was still inferior to IP delivery where saturation occurred in under an hour (Figure 6F). As seen in Figure 7B and D, leaky vessels also reduced the heterogeneity in drug accumulation.

Figure 7

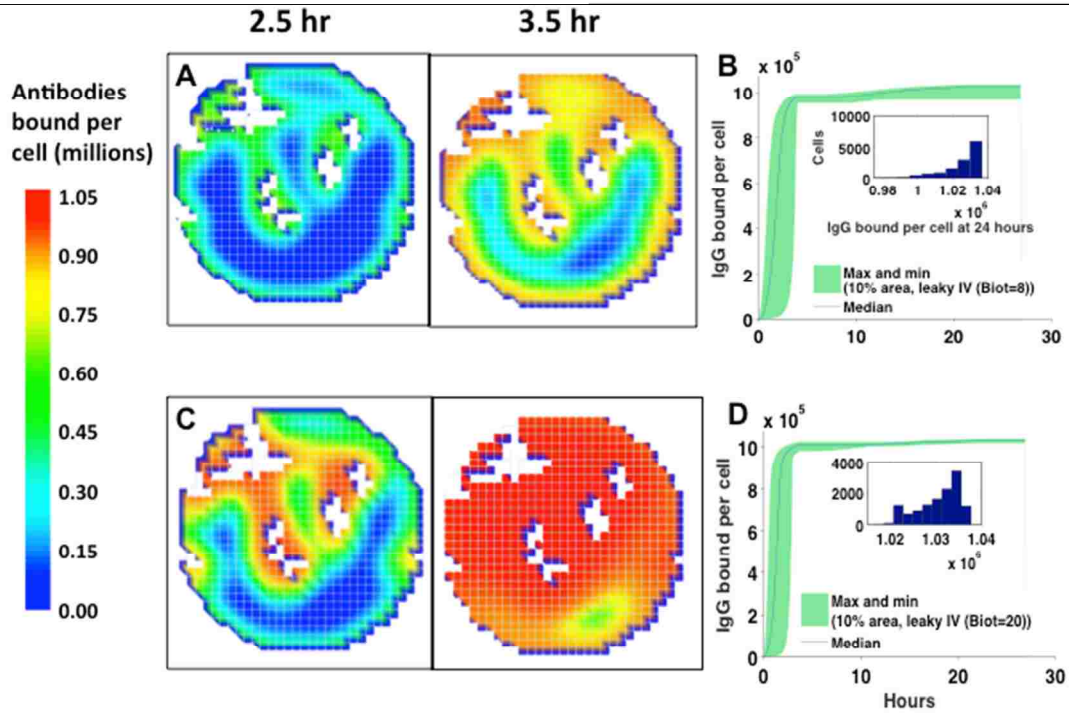


FIGURE 7. Simulated IV delivery of pertuzumab in tumors with leaky vessels of 10% vascular area predicts reduced drug heterogeneity compared to IV and IP, and better delivery than IV but not IP. Delivery from leaky vessels corresponded with increased Biot numbers of 8 (A,B; 3.5 times that of normal vasculature) and 22.5 (C,D, 10 times higher) at 2.5 and 3.5 hours (B,D). Plots of minimum, maximum, and median accumulation over time, expressed as receptors bound bivalently to antibody per cell. *Insets*: Distribution of antibody bound bivalently to receptors in all tumor cells at 24 hours.

Figure 8 provides experimental validation of our predictions that direct delivery of antibody to the peritoneum is the superior route. Here, we took advantage of our human xenograft animal model. GFP-expressing SKOV3.ip cells were injected into nude mice, followed by 2 weeks of tumor cell proliferation in the mice. Fluorescently-tagged pertuzumab was injected either IV or IP, followed by humane sacrifice of recipient mice at time points indicated in this figure. Tumors were excised from the mesentery or omentum and imaged by two-photon microscopy. As shown in Figure 8A, IP injection resulted in near uniform binding of antibody to ErbB2 on tumor cells within 3 hours. In contrast, IV injection resulted in variable levels of drug binding within the first 3 hours after administration (Figure 8B). As shown in Figure 8C, there was little improvement in drug binding even at 24 hours after IV delivery. At 72 hours post-IV injection, binding of tagged antibody to cells in the tumor is markedly diminished in the center of the tumors, possibly due to internalization and degradation. Antibody at the tumor periphery at late time points after IV injection may be principally due to delayed secondary delivery from the peritoneal compartment.

Figure 8

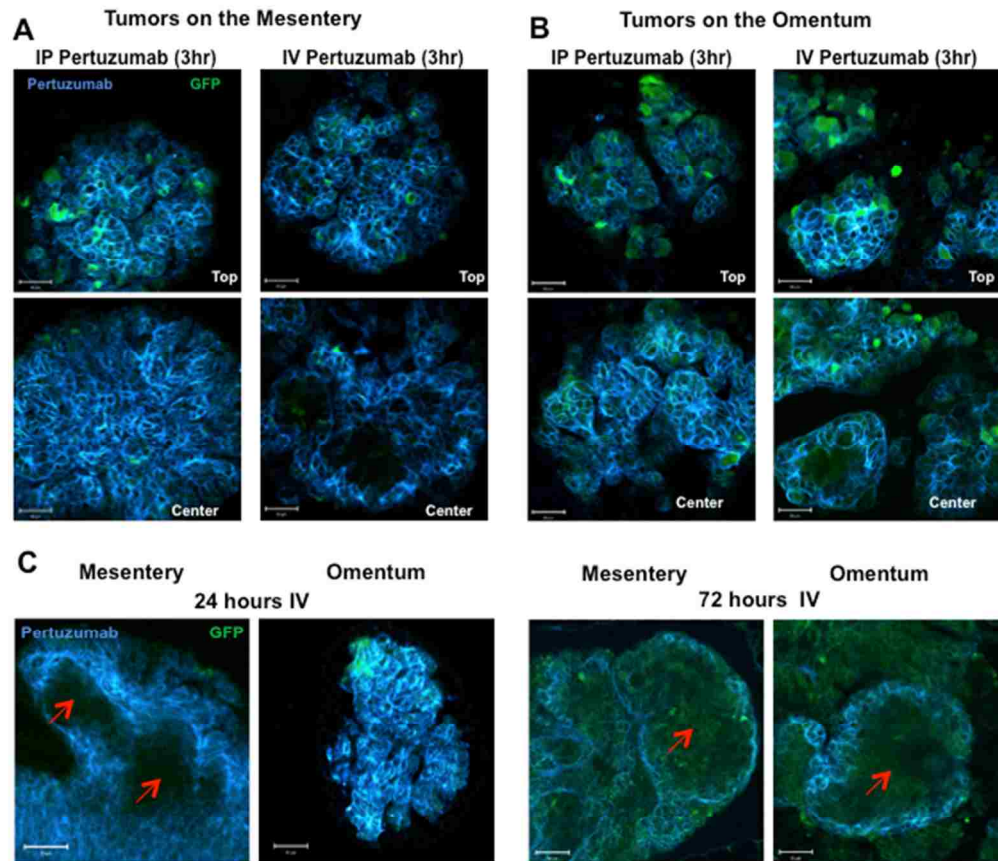


FIGURE 8. *In vivo* validation of IP as optimal route for therapeutic antibody. Penetration of pertuzumab (blue) into tumors on the mesentery (A) and omentum (B) of nude mice engrafted 2 weeks prior with human SKVO3.ip cells. Images were acquired 3, 24 or 72 hours after IP or IV delivery of 100  $\mu$ l containing 0.4 mg Pacific-Blue conjugated pertuzumab (20 mg/kg). A) Comparison of fluorescent antibody binding in mesentery tumors 24 hours after IP or IV injection. B) Comparison of fluorescent antibody binding in omental tumors 24 hours after IP or IV injection. C) Limited labeling of omental or mesentery tumors with fluorescent antibodies 24 or 72 hours after IV injection.

## DISCUSSION

Here, we use a spatially explicit model to represent the delivery of soluble therapies to microscopic ovarian tumors disseminated in the abdominal cavity (Figure 3). Others have advocated the usage of *in silico* models to clarify the complex process of drug delivery both in ovarian cancers<sup>33</sup> and for therapeutic antibodies<sup>37,38,56</sup>. We incorporate pharmacokinetic parameters from tumor tissue *in vivo* and *in vitro* and vascular densities derived from human patients to help us understand how the interplay of drug dynamics at the molecular, cellular, and tissue scales impacts delivery to tumor cells. Our model is well integrated with experimental data, including measurements in cultured spheroids and xenograft models.

In our simulations we chose to focus on treatment strategies for minimal residual disease after debulking surgery. Clinical evidence suggests a survival advantage for IP over IV chemotherapy in optimally debulked patients<sup>4,5,57-59</sup>. However, there is still reluctance in many hospitals to administer IP therapy, due to the expertise required to implant peritoneal ports and to monitor for the potential complications of cytokine storms and other toxicities. A recent study presented at the 2014 ASCO meeting reports that less than half of eligible patients receive IP chemotherapy<sup>59</sup>. Our model was able to assess the effect of delivery route on drug penetration into tumors, showing that the impact of the IP route on efficacy may be underappreciated. Results emphasize the importance of direct drug delivery to the peritoneum for superior penetration into microscopic avascular tumors, which likely comprise the majority of residual tumors in optimally debulked patients. We show that the same dose of cisplatin delivered IP leads to uniformly higher accumulation

within tumor cells. The platinum accumulation levels throughout a small tumor exceed the IC50 concentration as predicted *in vitro*<sup>51</sup>. IV delivery leads to much less accumulation of cisplatin, with levels far below the IC50 for cytotoxicity. Because drug must reach avascular tumors from the peritoneal fluid, IV delivery increases the time it takes for the drug to enter the peritoneal cavity. The concentration of cisplatin reaching the peritoneum is limited, this secondary delivery markedly limits accumulation in tumor cells.

Ovarian cancer cells also grow as vascularized tumors attached to peritoneal organs and our previous studies in the SKOV3.ip xenograft model indicate that even small tumors (30-40 cells in diameter) may be well vascularized. Therefore, we went on to test how vascular density will alter drug penetration using our model. Surprisingly the advantage of IP delivery persists for small vascularized tumors. Even in tumors with the 10% vascular density, IP delivery improved the accumulation of cisplatin in small tumors by 100 fold (Fig. 5) and provide one explanation for improved survival. This underscores the need for IP chemotherapy in cases where patients have been optimally debulked. An interesting finding from the simulations is that, as vascular density of the tumor increases, the drug accumulation after IP delivery becomes much less uniform. After IP delivery of cisplatin, drug concentration in the vessels is always lower than in the peritoneal fluid. Therefore, the vessels act as a sink, absorbing small molecular weight drugs and reducing cisplatin accumulation in a small number of cells in proximity to the vessels. These cells could be those that survive therapy and lead to relapse.

Although patients initially respond well to platinum/taxol regimens, many will relapse. Novel treatment strategies, including therapeutic antibodies, are being considered to limit recurrence<sup>60</sup>. Previous trials with anti-EGFR and anti-ErbB2 antibodies had limited success<sup>61</sup>. These disappointing results may be due to two factors: 1) ineffective delivery and 2) poor stratification of patients based upon receptor expression patterns. Based upon IHC results for a tumor microarray representing 200 ovarian tumor patients, we recently determined that only a limited subset of ovarian tumors express significant levels of either ErbB1/EGFR or ErbB2/Her2<sup>44</sup>. The SKOV3.ip cell line used in our studies here is an example of this ErbB2 positive subset, since they express over 2 million ErbB2 per cell. With this as a model system, we examined the penetration of the anti-ErbB2 therapeutic antibody, pertuzumab, to determine whether the advantage of IP delivery extends to this class of therapies. Antibodies, being larger molecules than chemotherapeutic agents, have more limited exchange between compartments. Simulations predicted a significant difference in IP vs IV delivery, again attributed to lower penetration from the blood into tumors. Our results suggest that intraperitoneal delivery, possibly in combination with delivery through the IV route, will yield optimal results for this class of therapeutics.

Our model is a powerful predictive tool that can be used to test optimal dosing of both small molecule drugs and therapeutic antibodies. The benefits of peritoneal delivery likely applies to antibodies now in the pharmaceutical pipeline or in clinical trials that target other surface receptors more commonly expressed on ovarian tumor cells. Examples include intact antibodies targeting ErbB3 and Met, as well as antibody-toxin



conjugates where low doses may be required to limit toxicity. In addition to new receptor targets, antibody affinity, receptor expression levels and vascular leakiness will be factors in the success of the antibodies in the pipeline for this disease. The OvTM model will be useful to predict outcomes taking in these new variables.

## **ACKNOWLEDGEMENTS**

We acknowledge the following: Dr. Michael Wester for algorithm development and runtime estimates; Scalenet Lab members Neal Holtschulte and Joshua Hecker for help with Python and Git; Dr. Tim Thomas for offering a computing “cluster in a box” to run simulations; the CC3D development group, particularly Dr. Maciek Swat and Julio Belmonte; Dr. Susan Atlas and the Center for Advanced Research Computing (CARC); pathologist Dr. Lesley Lomo for scoring human ovarian tumor sections; Drs. Ashput Rajut, Meghan Pryor and Francois Asperti-Boursin for valuable discussion; Dr. Sarah Adams for conceptual contributions to OvTM model development; Human Tissue Repository, Flow Cytometry and Microscopy Core Facilities at the UNM Cancer Center; Anna Holmes for technical assistance with IHC.

## **AUTHOR CONTRIBUTIONS**

KW contributed writing, computer models and microscopic analysis of vasculature; MS contributed writing and performed *in vivo* and *in vitro* experiments; RL contributed to Stereo Investigator measurements; and YJ, MM, BW contributed to writing, experimental design and integration of biologic and *in silico* experiments.

## SUPPLEMENTAL MATERIAL

The Supplemental Material for this article can be found at [http://www.frontiers.org/Molecular\\_and\\_Cellular\\_Oncology/Article #](http://www.frontiers.org/Molecular_and_Cellular_Oncology/Article#).

### Model Assumptions

**Tissues:** For simulations, we initialized a tumor model that would run in 5-6 days, of 30 cells in diameter.

Time simulated depended on the length of patient data sets, even if these were not long with respect to the drug half-life, as in the case of therapeutic antibodies. Time simulated was also limited by the diffusion rates of drugs. Measurement of any molecule coming into contact with a cell required a time step in which diffusion length of the drug was one cell diameter, which created a rigidly set number of steps to simulate a drug time course, requiring 7 to 8 days per simulation.

Because our biological model is of SKOV3.ip1 cells, wherever possible, parameters experimentally derived from this cell line were used in the model. If, in a given paper, data for SKOV3 or SKOV3.ip1 cells was not included, but SKOV3.ip1 was described as similarly resistant or in the same class as another cell line, and no explicit SKOV3.ip1 data was available, then data for the similar cell line was used.

Fits of Cisplatin extracellular exposure to cancer cell lines from El-Kareh, 2003 match the IC50 for the most sensitive cell line tested by Mistry et al., 1992. For 180 or more minutes, cells in the simulations are within Cisplatin concentrations found to be necessary for accumulation and damage in the data fits constructed by El-Kareh *et al.*<sup>62</sup>.

Factors affecting drug distribution in peritoneal fluid, blood, and tissue (pharmacokinetics)

We used data for unbound concentration of drug rather than total drug, as "the action exerted by drugs is generally more closely related to unbound than total concentration of drugs." <sup>63</sup>.

"Effective" penetration rates in tumor tissue or spheroids, which include all processes that might decrease penetration from the rate found in water, were used to parameterize diffusion for Cisplatin and Pertuzumab. We parameterized diffusion from empirically derived effective diffusion coefficients for non-binding molecules in tumor tissue *in vivo*. Sodium fluorescein (molecular weight 376 Da, <sup>41</sup>) was used to represent Cisplatin (molecular weight 300.5Da). Pertuzumab effective diffusion in avascular tumors was represented by non-binding IgG either measured directly by FRAP in SKOV3.ip1 spheroids *in vitro*, or penetration in vascularized tumors by non-binding IgG measured *in vivo* <sup>39, 43</sup>. These coefficients are affected by unmeasured events of convection, binding by target and non-target molecules, tortuosity of interstitial space, inhibition by the fiber mesh of the extracellular matrix (antibodies are ~20nm at their widest <sup>64</sup>, and other barriers to penetration. We found the rough FRAP estimate of 13  $\mu\text{m}^2/\text{sec}$  to be nearly identical to the *in vivo* estimate of 10  $\mu\text{m}^2/\text{sec}$  <sup>39</sup> to 13  $\mu\text{m}^2/\text{sec}$  [5].

We add the physical barrier of low-permeability vascular endothelium to the penetration of antibodies, as recommended by Thurber, *et al.*, 2011 [4]. We decrease the percentage of IV antibody available at the vessel surface from the plasma concentration by the ratio called the Biot number by Thurber *et al.* (Biot number = 0.0225 for the average diameter of vessels found in this paper, 0.024 in [4]). This number concurs with

a reflection coefficient of 0.95-0.98 for antibodies inside of vessels [Wang, 2008], and will likely be higher for “leaky” vessels often found in tumors. We therefore assume relatively intact, non-leaky vessels in simulations, unless explicitly stated for our leaky simulations.

We use effective penetration and cell uptake as the sole barriers to small-molecule drug penetration on the assumption that tumor vessels are well-perfused, again as discussed by Thurber et al., 2011 [Thurber, 2011].

Penetration rates and patterns of drugs in spheroids grown in vitro can be significantly different depending on the drug [Nederman 1981]. We use penetration rates of therapeutic antibodies in SKOV3.ip1 spheroids to calculate effective passive diffusion coefficients from the IP surface of ovarian tumors, and compare these to rates derived for tumor tissue in the literature. The difference between target-specific antibody penetration of trastuzumab and pertuzumab in SKOV3.ip1 spheroids and non-specific IgG, measured by FRAP in SKOV3.ip1 spheroids (which was equivalent to *in vivo* penetration rates in the literature), was 1000-fold lower ( $6.2 \text{ E}10 \text{ cm}^2/\text{sec}$  vs.  $1.33 \text{ E}07 \text{ cm}^2/\text{sec}$ ), implicating a slow-down of penetration caused solely by binding to target.

We assume that an IV injection does not significantly increase the blood volume; we conversely assume that IP treatment is initially at 100% of the original concentration. However, this may not be the case for patients with ascites.

Drugs have a half-life in the body that is affected by binding to the total cell population, to soluble components in the plasma, and filtering in the liver and kidneys. We do not add any further decay processes in blood or peritoneal fluid, using only empirically measured concentrations.

In 2 of the 4 delivery combinations (IP, IV, Cisplatin), we have simultaneous concentration data in patients for both compartments. Where we do not have such simultaneous data (IV delivery of Pertuzumab, or in mathematically elevated dosing of Pertuzumab) we a. use IP/IV and IV/IP ratios from antibodies delivered IV and IP to rats [Wahl, 1988], and b. assume that ratios of drug in the secondary compartment to the primary compartment are dose-independent.

IP and IV administration time courses for Cisplatin are fit to curves for 60mg/m<sup>2</sup> dosage (Casper, 1984).

IP administration time course of antibody is fit to a curve for 5 mg/kg of immunotoxin conjugate in 2l of saline [Pai, 1991], and IV is fit to a curve for 5 mg/kg Pertuzumab [FDA Clinical Pharmacology Review, BLA 125409 (Pertuzumab)].

Cisplatin threshold for 50% SKOV3 cell death (IC<sub>50</sub>) is 52.1  $\mu$ M accumulated per cell during a 38.3 $\mu$ M solution 2-hour exposure [Mistry, 1992]. Accumulation is treated as linear [Mistry, 1992] and occurs in each time step as a proportion of what would have accumulated at the current concentration at the cell over 2 hours. Accumulation is calculated from a fit of total accumulated platinum in SKOV-3 cells during 2-hour exposures to a range of concentrations. Other values for Cisplatin IC<sub>50</sub> in ovarian cancer cell lines include 12.6  $\mu$ M [Yu, 2011], (“cisplatin-resistant subline HKESC-1/cis“), 79.8 $\mu$ M (EC<sub>50</sub> in SKOV3 cells, [Scoles, 2007]), 33 $\mu$ M (10 $\mu$ g/ml, in OVCAR cells, [Royer, 2005]) and 0.99 $\mu$ M (0.3  $\mu$ g/ml, [Nakano, 1997]).

Pertuzumab binding to ErbB2 is considered irreversible, as observed in our experiments with multiple SKOV3.ip1 samples (data not included), and as in [Mattes, 1994] (via [Thurber, 2011], [Thurber, 2008]). This “irreversible” binding may partly be

the result of rapid internalization of antibody-tagged ErbB2, as tagged ErbB is internalized in minutes [Thurber, 2008b].

Aside from the calculation of antibody bound at each time step using  $K_d$ , we do not explicitly model release of antibodies from ErbB2 ([Thurber, 2011], m).

The  $K_d$  (equilibrium coefficient, or inverse affinity) of Trastuzumab is 0.12nM, and Pertuzumab is 9.1nM; both are considered high-affinity antibodies (<=low nanomolar; AbCam.com: “KD value: A quantitative measurement of antibody affinity;” [Thurber, 2008]). Antibody bound after each time step is calculated as:

$$\begin{aligned}
 & IgG_{Newly\ Bound} \\
 &= \left( (ErbB2_T + 2 * IgG_T + K_d\ Pertuzumab) \right. \\
 &\quad \left. - \left( \sqrt{((ErbB2_T + 2 * IgG_T + K_d\ Pertuzumab)^2 - 8 * (ErbB2_T * IgG_T))} \right) \right) \\
 &\quad /4
 \end{aligned}$$

where  $ErbB2_T$  = total receptors (bound and unbound),  $IgG_T$  = total pertuzumab (bound and unbound) after the influx of new, unbound pertuzumab, but before binding, and  $K_{dPertuzumab}$  is the dissociation constant for pertuzumab (9.1nM).

Thresholds for tumor cell color changes in the model for Pertuzumab are 100,000 receptors bound for initiation of antibody-dependent cell-mediated cytotoxicity, and 95% of 2 million total on the cell surface, to mark near-complete saturation.

A simultaneous data set of IP-post-IV antibody with units of concentration (as opposed to radioactivity or other measure) was not available for humans. Analysis of IV-

post-IP dynamics in rats shows that the ratio of concentrations has a 20-times higher slope (0.04429 vs. 0.001922) than for humans. IP-post-IV curves in humans for Cisplatin show a similar shape to that in rats (cubic fit in which the ratio drops slightly as drug in the two compartments nears zero or becomes nearly equilibrated), albeit over 2 hours instead of 26. Therefore in this model we compare drug dynamics based upon IP-post-IV and IV-post-IP rates from rats for consistency of pharmacokinetic environment, with a drug dosage proportionately 6 times that in humans [Nau, 1986]. We use these ratios in conjunction with human data for primary IP or IV delivery.

**Table 1: model parameters**

Parameter	Model Value	Model Units	Value	Common Units	Source
Cisplatin effective diffusion coefficient in tumor tissue	1	cell diam <sup>2</sup> / time step*	6.40E-06	cm <sup>2</sup> /s	Nugent, 1984
Cisplatin intraperitoneal concentration fitted curve (dosage = 60 mg/m <sup>2</sup> )	$163.3*t^{(-0.2859)} - 28.31$	μM, t=min			Casper, 1983
Initial cisplatin intraperitoneal concentration	64.63	μM, t=min			Casper, 1984
Cisplatin IV-post-IP concentration ratio fitted curve	$[IP(t)]*(-7.245e-09*t^4 + 2.772e-06*t^3 - 0.0003881*t^2 + 0.02126*t + 0.1941)$	μM, t=min			Casper, 1984
Cisplatin intravenous concentration fitted curve after 5 minutes (dosage = 60mg/m)	$-0.000001154*t^3 + 0.0005737*t^2 - 0.09922*t + 5.973$	μM, t=min			Casper, 1984
Cisplatin intravenous infusion concentration	$0.3725*t$	μM, t=min			Casper, 1984
Cisplatin constant concentration between end of infusion and first data point	5.59	μM, t=min			Casper, 1984



**Table 1 continued: model parameters**

Cisplatin IP-post-IV concentration ratio fitted curve	$[IV(t)] * (-1.154e-06 * t^3 + 0.0005737 * t^2 - 0.09922 * t + 5.973)$	$\mu\text{M}$ , t=min			Casper, 1984
Cisplatin (Pt) accumulation at current concentration in SKOV3 cell 2Hrs	$(0.4755 * \text{cisplatin} ** 1.289) * \text{MCSFractionOf}$	$\mu\text{M}$ accumulated per cell per time step**			Fig.3, Mistry, 1992
Cisplatin accumulated at IC50 (50% viability of control) for SKOV-3, 2h exposure	52.71	$\mu\text{M}$	251	pmol/mg protein	Mistry, 1992
Non-specific IgG FRAP-derived effective diffusion coefficient in SKOV3.ip1 spheroids	1	cell diam <sup>2</sup> / time step**	1.33E-07	cm <sup>2</sup> /s	m
Pertuzumab K <sub>d</sub> (binding percentage)	981.68	molecules/cell volume	9.1	nM	Li, 2013
Pertuzumab effective diffusion coefficient in SKOV3.ip1 in vitro spheroids	5.37	cell diam <sup>2</sup> / hr	6.20E-10	cm <sup>2</sup> /s	m
Pertuzumab binding *** reversal half-life	$\infty$	hr <sup>-1</sup>			m, Mattes 1994
Pertuzumab decay rate***	0	hr <sup>-1</sup>			Leveque, 2008

**Table 1 continued: model parameters**

Pertuzumab (immunotoxin conjugate) intraperitoneal concentration fitted curve (dosage = 5 mg/kg)***	$0.02679*t^2 + -2.1*t + 92.16$	molecules/ cell volume, t=hr			Pai, 1991
Pertuzumab IV-post-IP concentration ratio fitted curve (rats)***	$[IP(t)]*(3.913e-06*t^4 - 0.0002103*t^3 + 0.003897*t^2 + 0.01503*t + 0.0004171)$	molecules/ cell volume, t=hr			Wahl, 1988
Pertuzumab intravenous concentration fitted curve (dosage =5 mg/kg)	$200700*t^{-0.1025} - 91370$	molecules/ cell volume, t=hr			FDA Clinical Pharmacology Review, BLA 125409 (Pertuzumab)
Pertuzumab intravenous concentration prior to 3.68 hours (first time point)	$2.358e+04*t + 147.8$	molecules/ cell volume, t=hr			
Pertuzumab IP-post-IV concentration ratio fitted curve (rats) ***	$[IV(t)]*(-0.00001042*t^4 + 0.0004965*t^3 - 0.006146*t^2 + 0.0355*t + 0.0005605)$	molecules/ cell volume, t=hrs			Wahl, 1988
Biot number for Pertuzumab in ovarian tumor ***	0.0225	ratio of plasma conc. to vessel surface conc.			Thurber, 2011
ErbB2 receptor count on SKOV3.ip1	2,100,000	receptors			m

**Table 1 continued: model parameters**

Radius of SKOV3.ip1 cell	3.5	$\mu\text{m}$			Steinkamp, 2013
Vascular area in human secondary tumors from bowel and omentum	2-10	% area of central slice			m
Mean length of tumor vessel segment in breast cancer xenograft	40 +/- 5	$\mu\text{m}$			Savage, 2013
Mean radius of tumor vessel segment in breast cancer xenograft	18.46 +/- 0.54	$\mu\text{m}$			Stamatelos, 2014, Fig. 5
Mean radius of tumor vessel segment in human ovarian tumors	19.2 +/- 16	$\mu\text{m}$			m
mg protein per SKOV-3 cell	0.21	mg protein/ $\mu\text{l}$			Mistry, 1992

\*Time step for cisplatin = 1/1207.183 min.

\*\* Time step for pertuzumab =1/1500.679 hr.

\*\*\* Value estimated based on data obtained with other IgGs.

m= measured

## References for the Supplement

1. El-Kareh AW, Secomb TW (2003) A Mathematical Model for Cisplatin Cellular Pharmacodynamics. *Neoplasia* (New York, NY) 5: 161-169.
2. Henningsson A, Karlsson MO, Viganò L, Gianni L, Verweij J, et al. (2001) Mechanism-based pharmacokinetic model for paclitaxel. *Journal of clinical oncology* 19: 4065-4073.
3. Nugent LJ, Jain RK (1984) Extravascular diffusion in normal and neoplastic tissues. *Cancer Res* 44: 238-244.
4. Thurber GM, Weissleder R (2011) A systems approach for tumor pharmacokinetics. *PLoS One* 6: e24696.
5. Berk DA, Yuan F, Leunig M, Jain RK (1997) Direct in vivo measurement of targeted binding in a human tumor xenograft. *Proc Natl Acad Sci U S A* 94: 1785-1790.
6. Kienberger F, Mueller H, Pastushenko V, Hinterdorfer P (2004) Following single antibody binding to purple membranes in real time. *EMBO reports* 5: 579-583.

## REFERENCES

1. Howlader, N., *et al.* SEER Cancer Statistics Review, 1975-2011, . in [http://seer.cancer.gov/csr/1975\\_2011/](http://seer.cancer.gov/csr/1975_2011/), Vol. based on November 2013 SEER data submission posted to the SEER web site, April 2014. (National Cancer Institute. Bethesda, MD, ).
2. Baldwin, L.A., *et al.* Ten-year relative survival for epithelial ovarian cancer. *Obstetrics and gynecology* **120**, 612-618 (2012).
3. Kyrgiou, M., Salanti, G., Pavlidis, N., Paraskeva, E. & Ioannidis, J.P. Survival benefits with diverse chemotherapy regimens for ovarian cancer: meta-analysis of multiple treatments. *Journal of the National Cancer Institute* **98**, 1655-1663 (2006).
4. Jaaback, K. & Johnson, N. Intraperitoneal chemotherapy for the initial management of primary epithelial ovarian cancer. *The Cochrane database of systematic reviews*, Cd005340 (2006).
5. Elit, L., *et al.* Intraperitoneal chemotherapy in the first-line treatment of women with stage III epithelial ovarian cancer: a systematic review with metaanalyses. *Cancer* **109**, 692-702 (2007).
6. NCI. Clinical Announcement on Intraperitoneal Chemotherapy in Ovarian Cancer Available from: [http://ctep.cancer.gov/highlights/20060105\\_ovarian.htm](http://ctep.cancer.gov/highlights/20060105_ovarian.htm) (2006).
7. Khanna, R. & Krediet, R.T. Textbook of Peritoneal Dialysis **Springer Science and Business Media, Publisher** (2009).
8. Bellman, R.E., Jacquez, J.A. & Kalaba, R. Mathematical Models of Chemotherapy. in *Proceedings of the Fourth Berkeley Symposium on Mathematical Statistics and Probability, Volume 4: Contributions to Biology and Problems of Medicine* 57-66 (University of California Press, Berkeley, Calif., 1961).
9. Kim, M., Gillies, R.J. & Rejniak, K.A. Current advances in mathematical modeling of anti-cancer drug penetration into tumor tissues. *Frontiers in oncology* **3**, 278 (2013).
10. Byrne, H.M. Dissecting cancer through mathematics: from the cell to the animal model. *Nat Rev Cancer* **10**, 221-230 (2010).
11. Sinek, J.P., *et al.* Predicting drug pharmacokinetics and effect in vascularized tumors using computer simulation. *Journal of mathematical biology* **58**, 485-510 (2009).
12. Evans, C.J., *et al.* A mathematical model of doxorubicin penetration through multicellular layers. *Journal of Theoretical Biology* **257**, 598-608 (2009).
13. Bilsland, A.E., *et al.* Mathematical model of a telomerase transcriptional regulatory network developed by cell-based screening: analysis of inhibitor effects and telomerase expression mechanisms. *PLoS computational biology* **10**, e1003448 (2014).
14. Cheng, F.H., *et al.* A Mathematical Model of Bimodal Epigenetic Control of miR-193a in Ovarian Cancer Stem Cells. *PloS one* **9**, e116050 (2014).

15. Khalil, H.S. Quantitative analysis of NRF2 pathway reveals key elements of the regulatory circuits underlying antioxidant response and proliferation of ovarian cancer cells. (2014).
16. Wilbaux, M., *et al.* Dynamic modeling in ovarian cancer: an original approach linking early changes in modeled longitudinal CA-125 kinetics and survival to help decisions in early drug development. *Gynecologic oncology* **133**, 460-466 (2014).
17. You, B., *et al.* The strong prognostic value of KELIM, a model-based parameter from CA 125 kinetics in ovarian cancer: data from CALYPSO trial (a GINECO-GCIG study). *Gynecologic oncology* **130**, 289-294 (2013).
18. Hori, S.S. & Gambhir, S.S. Mathematical model identifies blood biomarker-based early cancer detection strategies and limitations. *Science translational medicine* **3**, 109ra116 (2011).
19. Bayraktar, S., *et al.* Predictive factors for BRCA1/BRCA2 mutations in women with ductal carcinoma in situ. *Cancer* **118**, 1515-1522 (2012).
20. Nikas, J.B., Boylan, K.L., Skubitz, A.P. & Low, W.C. Mathematical prognostic biomarker models for treatment response and survival in epithelial ovarian cancer. *Cancer informatics* **10**, 233-247 (2011).
21. Becker, K., *et al.* Patterns of p73 N-terminal isoform expression and p53 status have prognostic value in gynecological cancers. *International journal of oncology* **29**, 889-902 (2006).
22. Kaijser, J., *et al.* Presurgical diagnosis of adnexal tumours using mathematical models and scoring systems: a systematic review and meta-analysis. *Human reproduction update* **20**, 449-462 (2014).
23. Lambert, H.E., Gregory, W.M., Nelstrop, A.E. & Rustin, G.J. Long-term survival in 463 women treated with platinum analogs for advanced epithelial carcinoma of the ovary: life expectancy compared to women of an age-matched normal population. *International journal of gynecological cancer : official journal of the International Gynecological Cancer Society* **14**, 772-778 (2004).
24. Newby, J.A., Busby, C.C., Howard, C.V. & Platt, M.J. The cancer incidence temporality index: an index to show temporal changes in the age of onset of overall and specific cancer (England and Wales, 1971-1999). *Biomedicine & pharmacotherapy = Biomedecine & pharmacotherapie* **61**, 623-630 (2007).
25. Rosner, B.A., Colditz, G.A., Webb, P.M. & Hankinson, S.E. Mathematical models of ovarian cancer incidence. *Epidemiology (Cambridge, Mass.)* **16**, 508-515 (2005).
26. Roupa, Z., *et al.* Serum CA 125 combined with transvaginal ultrasonography for ovarian cancer screening. *In vivo (Athens, Greece)* **18**, 831-836 (2004).
27. Jain, H.V. & Meyer-Hermann, M. The molecular basis of synergism between carboplatin and ABT-737 therapy targeting ovarian carcinomas. *Cancer research* **71**, 705-715 (2011).
28. Kohandel, M., Sivaloganathan, S. & Oza, A. Mathematical modeling of ovarian cancer treatments: sequencing of surgery and chemotherapy. *J Theor Biol* **242**, 62-68 (2006).
29. Pereira, A., *et al.* Defining the optimal lymphadenectomy cut-off value in epithelial ovarian cancer staging surgery utilizing a mathematical model of

- validation. *European journal of surgical oncology : the journal of the European Society of Surgical Oncology and the British Association of Surgical Oncology* **39**, 290-296 (2013).
30. Varma, R., *et al.* Platinum drug effects on the expression of genes in the polyamine pathway: time-course and concentration-effect analysis based on Affymetrix gene expression profiling of A2780 ovarian carcinoma cells. *Cancer chemotherapy and pharmacology* **59**, 711-723 (2007).
  31. Sigal, B.M., Munoz, D.F., Kurian, A.W. & Plevritis, S.K. A simulation model to predict the impact of prophylactic surgery and screening on the life expectancy of BRCA1 and BRCA2 mutation carriers. *Cancer epidemiology, biomarkers & prevention : a publication of the American Association for Cancer Research, cosponsored by the American Society of Preventive Oncology* **21**, 1066-1077 (2012).
  32. Jiang, J., *et al.* Epidermal growth factor-independent transformation of Ba/F3 cells with cancer-derived epidermal growth factor receptor mutants induces gefitinib-sensitive cell cycle progression. *Cancer research* **65**, 8968-8974 (2005).
  33. Loessner, D., Flegg, J.A., Byrne, H.M., Clements, J.A. & Huttmacher, D.W. Growth of confined cancer spheroids: a combined experimental and mathematical modelling approach. *Integrative biology : quantitative biosciences from nano to macro* **5**, 597-605 (2013).
  34. Steinkamp, M.P., *et al.* Ovarian tumor attachment, invasion, and vascularization reflect unique microenvironments in the peritoneum: insights from xenograft and mathematical models. *Frontiers in oncology* **3**, 97 (2013).
  35. Giverso, C., Scianna, M., Preziosi, L., Lo Buono, N. & Funaro, A. Individual Cell-Based Model for In-Vitro Mesothelial Invasion of Ovarian Cancer. *Math. Model. Nat. Phenom.* **5**, 203-223 (2010).
  36. El-Kareh, A.W. & Secomb, T.W. A Theoretical Model for Intraperitoneal Delivery of Cisplatin and the Effect of Hyperthermia on Drug Penetration Distance. *Neoplasia (New York, N.Y.)* **6**, 117-127 (2004).
  37. Thurber, G.M., Schmidt, M.M. & Wittrup, K.D. Antibody tumor penetration: Transport opposed by systemic and antigen-mediated clearance. *Advanced drug delivery reviews* **60**, 1421 (2008).
  38. Thurber, G.M., Schmidt, M.M. & Wittrup, K.D. Factors determining antibody distribution in tumors. *Trends in pharmacological sciences* **29**, 57-61 (2008).
  39. Thurber, G.M. & Weissleder, R. A systems approach for tumor pharmacokinetics. *PloS one* **6**, e24696 (2011).
  40. Swabb, E.A., Wei, J. & Gullino, P.M. Diffusion and Convection in Normal and Neoplastic Tissues. *Cancer research* **34**, 2814-2822 (1974).
  41. Nugent, L.J. & Jain, R.K. Extravascular diffusion in normal and neoplastic tissues. *Cancer research* **44**, 238-244 (1984).
  42. Clauss, M.A. & Jain, R.K. Interstitial transport of rabbit and sheep antibodies in normal and neoplastic tissues. *Cancer research* **50**, 3487-3492 (1990).
  43. Berk, D.A., Yuan, F., Leunig, M. & Jain, R.K. Direct in vivo measurement of targeted binding in a human tumor xenograft. *Proceedings of the National Academy of Sciences of the United States of America* **94**, 1785-1790 (1997).

44. Davies, S., *et al.* High Incidence of ErbB3, ErbB4, and MET Expression in Ovarian Cancer. *Int J Gynecol Pathol* **33**, 402-410 (2014).
45. Hashizume, H., *et al.* Openings between defective endothelial cells explain tumor vessel leakiness. *The American journal of pathology* **156**, 1363-1380 (2000).
46. Stamatelos, S.K., Kim, E., Pathak, A.P. & Popel, A.S. A bioimage informatics based reconstruction of breast tumor microvasculature with computational blood flow predictions. *Microvascular research* **91**, 8-21 (2014).
47. Yuan, F., *et al.* Vascular permeability and microcirculation of gliomas and mammary carcinomas transplanted in rat and mouse cranial windows. *Cancer research* **54**, 4564-4568 (1994).
48. Casper, E.S., Kelsen, D.P., Alcock, N.W. & Lewis, J.L., Jr. Ip cisplatin in patients with malignant ascites: pharmacokinetic evaluation and comparison with the iv route. *Cancer treatment reports* **67**, 235-238 (1983).
49. Pai, L.H., *et al.* Clinical evaluation of intraperitoneal Pseudomonas exotoxin immunoconjugate OVB3-PE in patients with ovarian cancer. *Journal of clinical oncology : official journal of the American Society of Clinical Oncology* **9**, 2095-2103 (1991).
50. Song, P., Krudys, K. & Grimstein, C. BLA 125409 Clinical Pharmacology Review - Pertuzumab. (eds. Liu, Q., Garnett, C. & Zineh, I.) (2011).
51. Mistry, P., *et al.* Comparison of cellular accumulation and cytotoxicity of cisplatin with that of tetraplatin and amminedibutyratodichloro(cyclohexylamine)platinum(IV) (JM221) in human ovarian carcinoma cell lines. *Cancer research* **52**, 6188-6193 (1992).
52. Scott, A.M., Wolchok, J.D. & Old, L.J. Antibody therapy of cancer. *Nat Rev Cancer* **12**, 278-287 (2012).
53. Trédan, O., Galmarini, C.M., Patel, K. & Tannock, I.F. Drug Resistance and the Solid Tumor Microenvironment. *Journal of the National Cancer Institute* **99**, 1441-1454 (2007).
54. Pink, D.B., Schulte, W., Parseghian, M.H., Zijlstra, A. & Lewis, J.D. Real-time visualization and quantitation of vascular permeability in vivo: implications for drug delivery. *PloS one* **7**, e33760 (2012).
55. McDonald, D.M. & Baluk, P. Significance of Blood Vessel Leakiness in Cancer. *Cancer research* **62**, 5381-5385 (2002).
56. Jain, H.V., Richardson, A., Meyer-Hermann, M. & Byrne, H.M. Exploiting the Synergy between Carboplatin and ABT-737 in the Treatment of Ovarian Carcinomas. *PloS one* **9**, e81582 (2014).
57. Howell, S.B., *et al.* Long-term survival of advanced refractory ovarian carcinoma patients with small-volume disease treated with intraperitoneal chemotherapy. *Journal of Clinical Oncology* **5**, 1607-1612 (1987).
58. Markman, M., *et al.* Impact on survival of surgically defined favorable responses to salvage intraperitoneal chemotherapy in small-volume residual ovarian cancer. *Journal of Clinical Oncology* **10**, 1479-1484 (1992).
59. Wright, A.A., *et al.* Effect of intraperitoneal chemotherapy on survival for ovarian cancer in clinical practice and frequency of use. *Journal of clinical oncology : official journal of the American Society of Clinical Oncology* **32**, Abstr 5576 (2014).



60. Sheng, Q. & Liu, J. The therapeutic potential of targeting the EGFR family in epithelial ovarian cancer. *British journal of cancer* **104**, 1241-1245 (2011).
61. Siwak, D.R., *et al.* Targeting the epidermal growth factor receptor in epithelial ovarian cancer: current knowledge and future challenges. *Journal of oncology* **2010**, 568938 (2010).
62. El-Kareh, A.W. & Secomb, T.W. A Mathematical Model for Cisplatin Cellular Pharmacodynamics. *Neoplasia (New York, N.Y.)* **5**, 161-169 (2003).
63. Henningsson, A., *et al.* Mechanism-based pharmacokinetic model for paclitaxel. *Journal of clinical oncology* **19**, 4065-4073 (2001).
64. Kienberger, F., Mueller, H., Pastushenko, V. & Hinterdorfer, P. Following single antibody binding to purple membranes in real time. *EMBO reports* **5**, 579-583 (2004).

**Chapter 4: Mesoscopic tumor models show correlations between vascular volume,  
vessel morphology, and heterogeneity of drug delivery**

Kimberly Kanigel Winner<sup>1,2</sup>, Mara P. Steinkamp<sup>3,5</sup>, Yi Jiang<sup>6</sup>, Carolyn Muller<sup>4,5</sup>, Bridget  
S. Wilson\*<sup>3,5</sup>, and Melanie Moses<sup>1,2,7</sup>

Departments of <sup>1</sup>Biology, <sup>2</sup>Computer Science, <sup>3</sup> Pathology and <sup>4</sup>OB/GYN and <sup>5</sup>Cancer  
Center, University of New Mexico, Albuquerque NM USA,

<sup>6</sup>Department of Mathematics and Statistics, Georgia State University, Atlanta GA USA,

<sup>7</sup>External Faculty of the Santa Fe Institute, Santa Fe NM USA

## ABSTRACT

Drug delivery drives the dominance of drug-resistant phenotypes among the genetically varied cells in tumors<sup>1,2</sup>. Non-uniform delivery of cancer-targeting drugs may drive evolution toward drug resistance at a faster pace<sup>2</sup>. Here, we compare the uniformity of concentrations of two drugs when delivered to vascularized tumor tissue by three vascular architectures. We use cellular automaton models of 3-dimensional vascularized tumors to explore heterogeneity in drug delivery given different distributions of vessel radii. We deliver two drugs intravenously, and at intravenous concentrations after intraperitoneal delivery: cisplatin, a small-molecule chemotherapeutic, and pertuzumab, a large-molecule monoclonal therapeutic antibody targeted at cancer cells overexpressing the ErbB2 receptor. We initialize vessel radii distributions for a) normal tissue, with the theoretically predicted allometric scaling exponent of  $\frac{1}{3}$  which assumes optimal energy-minimizing and space-filling vasculature, b) the empirical distribution of vessel radii from ovarian cancer metastases donated by patients, and c) a Gaussian distribution around the mean of the empirical data, which removes the largest vessels. The vessel radii generated by the three distributions result in different tumor vessel volume distributions. For cisplatin delivery, small *in silico* tumor tissue samples show little dependence on vessel volume, with accumulation correlating only with the concentration in the vessels. For pertuzumab, however, although drug delivery increases with increasing vascular volume, even at the highest concentration during delivery, highly heterogeneous delivery occurs. A sub-population of cells in poorly vascularized volumes accumulates sub-therapeutic levels of antibody, possibly allowing them to survive as the

progenitors of a new, potentially drug-resistant tumor. This result underscores previously discussed caveats of the usage of targeted therapies<sup>2</sup>. Finally, the Empirical distribution gives the poorest drug delivery.

## INTRODUCTION

In a previous work<sup>3</sup>, we addressed delivery of drugs to tumors exposed to the peritoneal cavity, from which drug could diffuse into the tumor surface, as well as from any vessels within the tumor. We noted that different vascular densities affected how uniformly drug was delivered to the tumor volume. In this modeling study, we address how tumor morphology and environment affect delivery of two drugs: cisplatin, a low-molecular-weight platinum-based chemotherapy, and pertuzumab, a high-molecular-weight therapeutic antibody. First, we model drug accumulation in tumor tissue too far from the peritoneal compartment to receive intraperitoneal drug, such as in the center of a large tumor, or in distant metastases. Second, we analyze our anatomical data on ovarian secondary tumor vasculature to see whether the distribution of vessel radii in ovarian tumors differs from normal tissue. Third, we compare the efficiency of delivery by the IV vs. the IP route. Fourth, we test whether the vascularity generated by three distributions of vessel radii resulted in three measurably different levels of maximum drug accumulation. Fifth, we test the effect of different vessel radii distributions and vascular volumes on drug delivery across tumor cells. We measure the maximum drug accumulation and heterogeneity of drug accumulation in all of the cells of a sample of simulated tumor, and use the third, fourth, and fifth studies to test the hypotheses that accumulation and heterogeneity are affected by a. the mode of delivery (IV vs IP), b. the distribution of vessel radii, and c. the vessel volume.

At the scale of the tumor, at least two types of spatial heterogeneity contribute to drug resistance. First, genetic heterogeneity exists across the tumor volume, providing a multitude of templates for drug resistance, rather than a clonal population in which each cell would have equal drug sensitivity<sup>4</sup>. Second, there can be heterogeneity of drug delivery, in which some cells receive cytotoxic levels of drug, while others experience sub-therapeutic exposures, increasing the probability of low-level drug accumulations leading to survival, mutation, and resistance. In combination, this means that a tumor is a library of genomes, any cell of which, if not delivered enough drug to kill it, may be selected for survival because of its intrinsically efficient resistance mechanisms, or may be optimally mutated to resist later drug deliveries.

After intravenous injection, drug immediately diffuses from vasculature into surrounding tissue. Drug delivery from the blood is dependent on the distribution of blood vessels in tissues. In previous models, we show that the percent vascular area in a cross-section of a tumor correlates with the amount of drug delivered<sup>3</sup>.

During drug delivery, drug accumulation inside or on the surface of each cell determines its fate. Cells may die either by the action of the immune system when a cell is tagged with antibodies (antibody-dependent cell-mediated cytotoxicity (ADCC)), or by apoptosis (self-programmed death) when the drug damages the cell. However, intrinsic resistance to the drug will also be activated, and the cell may survive. Cellular resistance to cisplatin has a multitude of mechanisms that may operate simultaneously, including the up-regulation of DNA repair factors that reverse drug damage, inactivation of the

drug, advantageous epigenetic changes, and efflux by active pumping<sup>5</sup>. Cisplatin is itself mutagenic; if the cell survives, it may develop mutations, including some that may contribute to drug resistance<sup>5</sup>. If a drug-exposed, resistant cell is intact enough to divide, it can become the seed of a new, drug-resistant cell population, either carrying its initial qualities that make it drug resistant, and/or new resistant mutations caused by treatment.

In ovarian cancer and other abdominally disseminated cancers, intraperitoneal (intra-abdominal) (IP) injection and intravenous (IV) injection are both commonly used to administer therapy. During IP delivery, different drugs have different penetration distances into the tissue. If the tumor is greater in radius or thickness than this penetration distance (about 0.5 mm in the case of cisplatin<sup>6</sup>, and about 1.2 mm for antibody (pertuzumab)<sup>7</sup>), delivery in the deeper parts of the tumor is dependent on the distribution and permeability of vessels. If an equal amount of drug is delivered per unit surface area of blood vessel, the spatial distribution and morphology of vessels will determine the uniformity of drug delivery.

Concentration inside of the vessels is determined by the dose and route of delivery. In both IV and IP delivery, as drug in the primary delivery compartment (either IP or IV) mixes throughout the body, the secondary compartment (either IV or IP, respectively) experiences a secondary concentration curve related to the primary concentration curve (for concentration curve fits, see<sup>3</sup>). During IP delivery, a tumor that is larger than the drug's penetration distance, or in another part of the body, will only receive this secondary, low concentration via the vessels.

Here we test the hypotheses that a. the mode of delivery (IV vs IP), b. the distribution of vessel radii, and c. the vessel volume may affect both the maximum drug accumulation and the heterogeneity of drug accumulation in cells of a tumor. We initialize vessels selected from three distributions of radii into spatially explicit mesoscopic-scale cellular automaton models: 1) the radius distribution as theoretically scaled in normal tissue (here called Theoretical), 2) the distribution found empirically in ovarian cancer (Empirical), and 3) a Gaussian distribution around the mean of the empirical data (Gaussian). We then simulate IP or IV drug delivery via these three vessel distributions and quantify the effect upon drug heterogeneity. Within each distribution, we run simulations for samples within a range of vessel volumes. The results are then applied to the distribution of vessel volumes in the complete tumor, to generate a histogram of the approximate drug delivery across the whole tumor volume.

In normal tissue, allometric scaling theory has predicted parameters for vessel morphology that allow the vascular network to efficiently fill space, thereby evenly delivering chemicals (oxygen, nutrients, cell-signaling factors, etc.) to terminal tissue volumes<sup>8</sup>. If vasculature were consistent with this idealized model, and drug was only delivered by the terminal branch (the thin-walled capillaries), this would result in drug delivery from small and terminal uniformly spaced vessels of similar size, as was assumed in <sup>3</sup>. A distribution without larger vessels could represent tumor vasculature that has been normalized with anti-angiogenic therapies, such as bevacizumab. However,



often, larger vessels and venules in tumors are “leaky--” hyper-permeable to proteins in the blood<sup>9</sup> -- thereby allowing greater saturation by larger-molecule therapies.

We account for the possibility of drug delivery from large vessels by allowing large, normally non-leaky vessels to deliver drug in two ways: first we assume that all empirically measured vessels deliver drug in our Empirical model; second we test drug delivery from the distribution of vessel sizes described by the West *et al.* , again with all vessels of all sizes delivering drug. These two models assume complete leakiness of large vessels, while our Gaussian model assumes the other extreme: no leakiness from large vessels so that drug is only delivered by the smallest vessels (the capillaries) in the tumor.

We hypothesize that for cisplatin, due to its relatively long penetration length relative to the spaces between vessels, penetration will not be affected by a lack of large vessels (a non-leaky vasculature), nor the morphology changes due to changes in distribution of radii, and that overall concentration will be affected most by the route of delivery (IP will be low and IV will be higher) and the vascular volume in the sample. For pertuzumab, the monoclonal antibody, we hypothesize that because the penetration distance can be limited due to the “stickiness” of the antibody, which creates a moving wave-front of accumulation, vascular density, and possibly vascular morphology, will correlate with heterogeneity of drug delivery.

## METHODS

### INITIALIZATION DATA SETS

We received nine patient ovarian cancer tumor sets from the UNM Tissue Repository, comprised of two tumors from each patient, with one tumor that had disseminated to the bowel and one to the omentum. We then used Stereo Investigator circle or line measure tools to measure vessel radii in the roundest vessels, which were most likely to have been cut transversely. (Detailed methods are provided in <sup>3</sup>.)

Among the assumptions of West *et al.*<sup>8</sup> are that the size of the terminal unit, the capillary, is invariant, and that a constant branching ratio from mother to daughter vessel is maintained at each branch node. To make comparisons between the morphology of the empirical vessel distribution and that predicted by scaling theory in normal tissue, we used radii from the lowest level (smallest vessels) of the empirical data to generate sets of vessel radii in two theoretical bifurcating vascular trees. Real vessel radii in the lowest level (capillary) were considered to be any vessel radius  $\leq 10\mu\text{m}$ . The empirical capillary count was 134. Using the count and average capillary radius, we calculated the bottom-level area of the cross-section of all real capillaries, and used this value to represent the area at the bottom of the tree for the theoretical cases. We then generated a vessel count and radius at each increasing level of the tree, using:

$$\frac{r_1}{r_2} = 2^{-\alpha} \quad (1)$$

where  $r_2$  = vessel radius of the current, larger branch of the tree,  $r_1$  = vessel radius of the next smallest branch of the vascular tree, and  $\alpha = \frac{1}{3}$  representing the vessel distribution of normal tissue. The ratio of the radii between the vessels in each branch level of the tree was scaled as  $2^{-\frac{1}{3}}$  from the previous (larger) level.

The distributions (empirical and  $\alpha = \frac{1}{3}$  (normal tissue)) were non-normal even after log transformation, so we compared the empirical data to the theoretical case using the Kolmogorov-Smirnov non-parametric test for comparison of two distributions, with a significance level of 5%, and the Mann-Whitney test.

The vessel generator used to build tissue for our previous models<sup>3</sup> was used to initialize a vascular web into a sphere using radii drawn from one of the three distributions (Fig. 2). Because tumor vasculature is disorganized<sup>10,11</sup> no attempt was made to reconstruct an organized vascular tree or mesh. For each model, radii were drawn at random from the vessels in the corresponding distribution. The first distribution, “Empirical,” was the complete data set of experimentally determined radii, which is a long-tailed distribution with a small number of large vessels. The second was a Gaussian distribution (3.01 to 14.21  $\mu\text{m}$  (mean = 8.61 +/- 5.60 $\mu\text{m}$ )), which truncated the original long-tailed distribution, removing the largest vessels, and therefore representing “non-leaky” larger vessels by discluding them. The third draw, “Theoretical,” was from Equation (1), with  $\alpha = \frac{1}{3}$ .

Spheres for simulations had a radius of 65 SKOV3.ip1 ovarian cancer cells, and were initialized at random with a range of 1 to 200 vessels in the volume. The final models were chosen so that the central z plane had a vascular area of ~10%, the maximum of the range measured in secondary human ovarian tumors<sup>3</sup>. 10x30x30-cell rectangular solids (shown in Fig. (2)) were sampled at random from the sphere volume. Samples corresponding to 1%, 3%, 5%, 10%, 15%, and 25% (24% for Theoretical) vascular volume were selected to model. The remaining volume of the 10x30x30-cell rectangular solid was filled in with tumor cells. These are the tumor samples used to simulate drug delivery, using the modeling platform OvTM, a cellular Potts model built in CompuCell3D which explicitly models individual cells, different cell types, and the diffusion and cellular accumulation drugs, as described in <sup>3</sup>. Models in this work differ from prior models only in the tissues morphology initialized.

To recreate a larger tumor and calculate the distribution of sample volumes in each morphology type, spheres 140 cells in radius were initialized at random with a range of 100 to 1000 vessels in the volume. To sample the distribution of volumes, 10x30x30-cell samples were drawn with replacement (potentially overlapping or oversampled) from a cube inscribed inside of each sphere of vessels, derived from the relationship

$$r^2 = 3 \left( \frac{1}{2} L^2 \right) \quad (2)$$

where  $r$  = radius of the sphere and  $L$  = length of the cube edge. Samples were drawn at random such that no part of their volume would fall outside of the cube inscribed in the tumor sphere.

Drug delivery simulations were run for the antibody pertuzumab, and the low-molecular-weight chemotherapeutic cisplatin. Drugs were delivered as though the tumor sample was far from the peritoneal cavity (greater than the penetration distance by small molecules (0.5mm) or large molecules (1.2mm)), and receiving drug via the plasma (blood volume compartment). Drug arrival via blood occurred after either an IP infusion or an IV infusion, as modeled in <sup>3</sup>. The code used was identical to the drug models in <sup>3</sup>, except *i*) the IP and IV compartments received equal initial concentrations instead of equal initial dosages (the IP dose was 69% that of the IV dose) and *ii*) tissues were initialized as described above.

Analysis of the heterogeneity of pertuzumab accumulation included a histogram of the accumulation for every cell at a single time point, and the calculation of the Shannon Entropy for the distribution of accumulations:

$$S = -\sum_i p_i * \log_2(p_i) \quad [3]$$

where  $S$  = Shannon Entropy, and  $p_i$  = the probability of each event. In this case the event is the radius at each branch  $i$  of the tree; the probabilities are the percentage of the tree vessels of the radius at each branch of the tree, since the entire sample is known.

The following steps generate a large tumor corresponding to our three vessel models. Six histograms approximating the simulation of IP or IV delivery in each of the three vascular distributions were generated. These were constructed by binning the

comprehensive samples (from the oversampled sphere with radius = 140 cells) into low (<10%), medium (10 to 23%) and high (>23%) classes. The samples in each accumulation simulation (1%, 3%, 5%, 10%, and 24 or 25% vessel volume) were then added to the full tumor distribution a number of times equal to the count of samples for low, medium, and high. For instance, in the Gaussian tumor, 25% of samples had less than 10% vessel volume. To comprise the “low” bin for accumulation in the complete Gaussian tumor at 9.86 hours, the complete list of drug accumulations in each individual cell of the 1% model at 9.86 hours was added to the bin enough times in order to comprise 25% of the tumor cells. 3% and 5% will be added to the “low” bin in future work, as well as a 50% case to be modeled and included.

## RESULTS

We analyzed the distribution of radii in the Empirical distribution vs. that Theoretical distribution (Fig. (1)). The Empirical (purple) and Theoretical (green, “Theoretical”) distributions are overlaid in Fig. 1 (intersections between the distributions are dark blue), showing the greater number of large-radius vessels in the Empirical distribution. Both are long-tailed, and the Empirical has more large vessels than expected from a normal distribution. Both log-transformed and non-transformed data were rejected for normality by the Jarque-Bera test at 5% significance in Matlab. Statistical analyses showed that the Empirical distribution is different from the Theoretical distribution. The Kolmogorov-Smirnov non-parametric test for 2 samples coming from the same distribution rejected that they were from the same distribution, ( $p < 0.001$ ). The Mann-Whitney test rejected

that the medians of the Empirical and Theoretical distributions were the same ( $p < 0.0001$ ).

Figure 1.

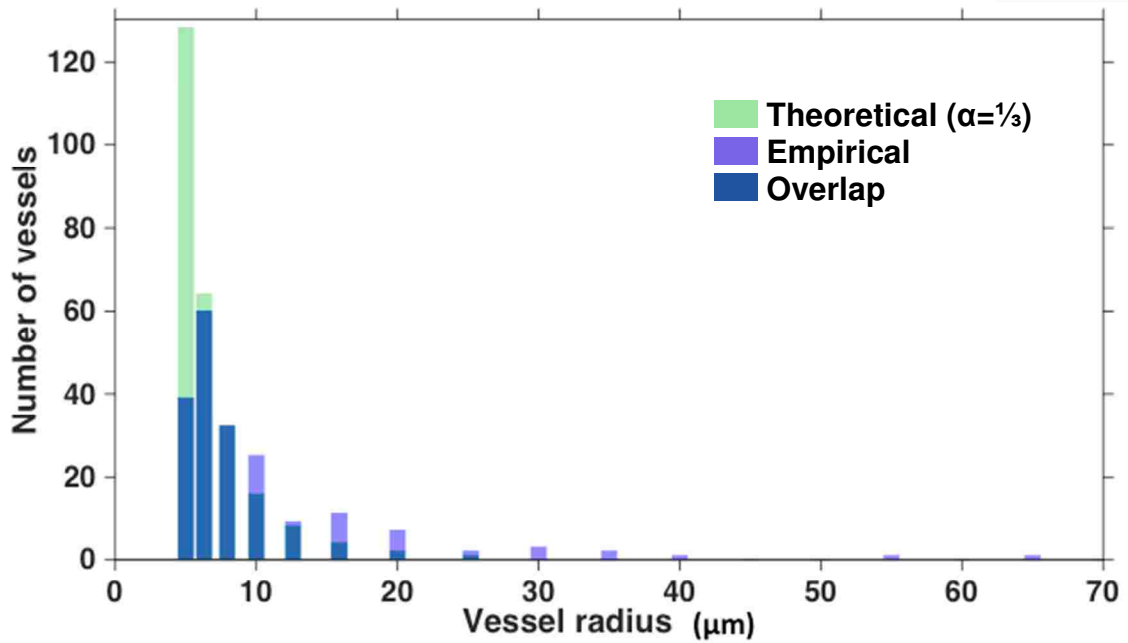


Figure 1: The Empirical distribution of vessel radii is statistically unique from the distribution for normal tissue based on scaling theory. Overlaid histograms of radii based on the Empirical distribution, and Theoretical distribution of a bifurcating tree with the scaling exponent  $\alpha=1/3$  between radii at each branch level, the theoretically predicted vessel size distribution for normal tissue.



A simplified schematic showing the process of drawing a 10x30x30-cell sample at random from a simulated tumor is shown in Figure 2A. Images of the 65-cell-radius vascular mesh generated for each of the three distributions of radii used in the drug simulations are shown in Figure 2B, 2C, and 2D. We created histograms of comprehensive samples from the cube inscribed inside of the spherical volume containing vascular mesh of 10% vascular area in the central z plane for each of the three radius distributions (Fig. (3)). For a sphere of  $R=140$ , vessel volumes were 0 to 55% in the 1000 10x30x30-cell samples from the Theoretical model. This range is close to empirically measured ranges for blood vessel volume in tumors, 5 to 50%<sup>12</sup>. Samples from the Empirical distribution ranged from 0 to 90% vessel volume; clearly some samples came from empty space, and others likely were drawn from the middle of a large vessel. The Gaussian model discluded the large vessels, and did not include the high or low ends of either the Theoretical or the Empirical volume samples, having a range of 5 to 25% vascular volume.

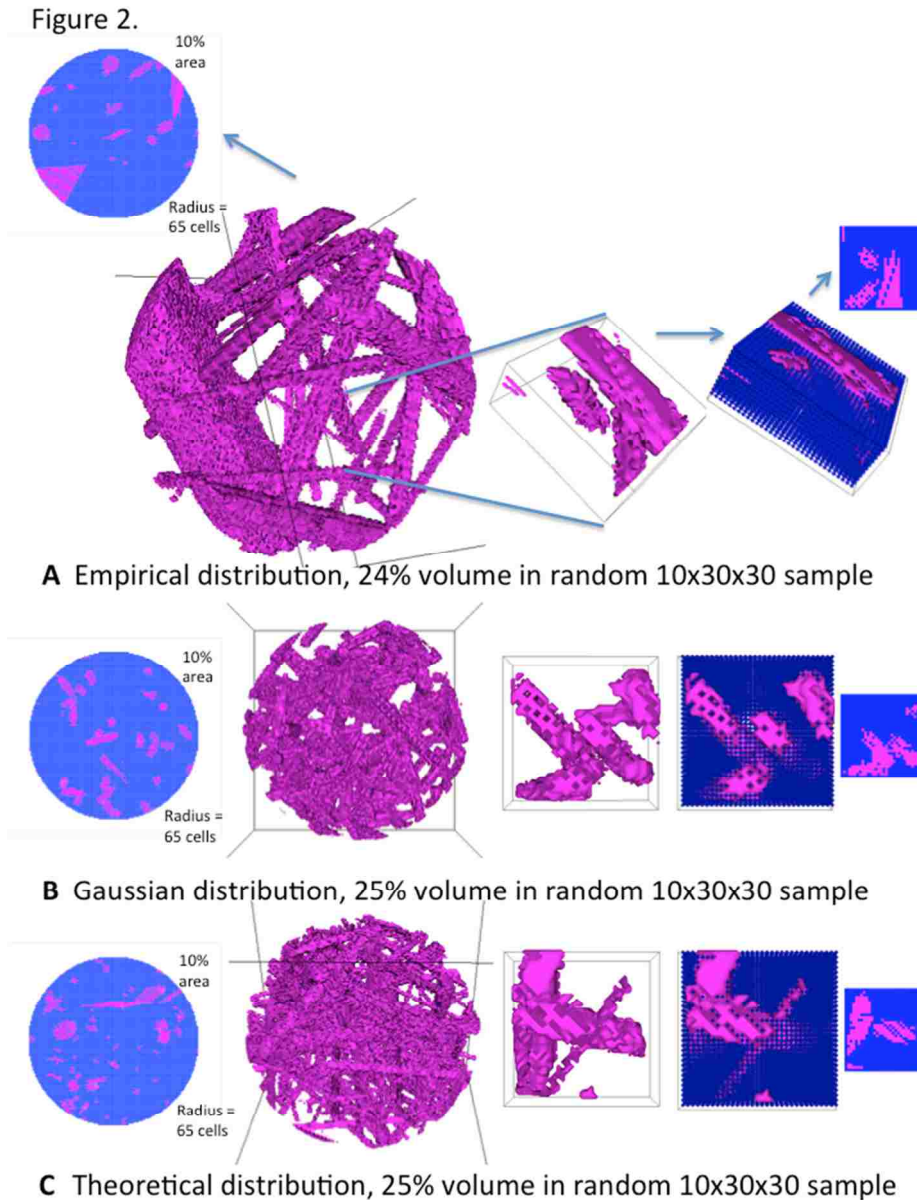


Figure 2: Images of vessels from three distributions of radii, generated in a simulated tumor (65 cells or  $\sim 0.45$ mm in diameter). Pink = vessel, purple = tumor cells. Cross-sections are in the xy plane at  $z=65$  (center of sphere), and contain 10% vessel. (A) Radii drawn from the complete Empirical distribution show thick vessels. (B) Radii drawn from a Gaussian distribution about the mean of empirical data (3.01 to 14.21  $\mu\text{m}$  (mean = 8.61  $\pm$  5.60  $\mu\text{m}$ )), include only small vessels. (C) Radii drawn from the Theoretical distribution show some large vessels and many small vessels. 10x30x30 samples were drawn at random from a cube inscribed in the tumor sphere, selected to represent a variety of vascular volumes, and used to initialize drug simulations. The three images at right in (A,B,C) show the 10x30x30 sample without tumor cells, with tumor cells, and the 2-D slice through the center of the sample at  $z=6$ , the view used to show results of simulations in Figs. 4 and 6.

Figure 3

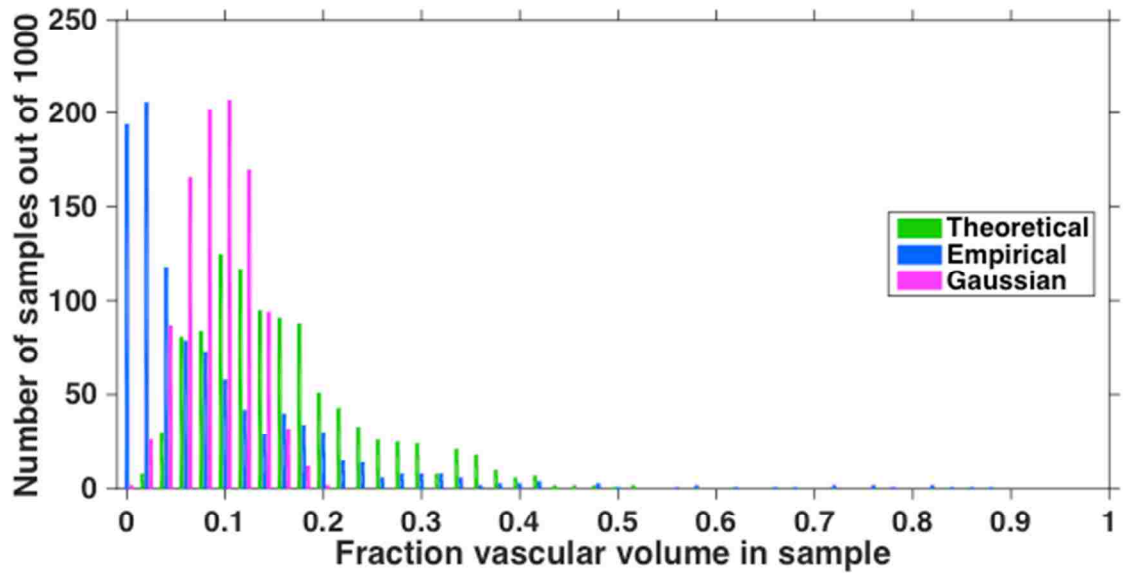


Figure 3: Vascular volume distributions from comprehensive sequential, non-overlapping sampling of a cube inscribed in the sphere of initialized vessels show the differences in vessel volume distribution for the three distributions of radii. Samples = 10 (z dimension) by 30 (y dimension) by 30 (x dimension) cells. The Gaussian distribution generates samples with 0 – 20% vessel volume. The Theoretical distribution has a wider range, up to 53%; and the Empirical distribution is even more variable, generating samples with up to 88% vessel volume.

We examined how the scale of accumulation changed with the various parameters of the model. The highest single-cell level of accumulation (Figs. 4, 5, and 6) increased with larger vessel volume for pertuzumab (10 hours of drug exposure, Fig. 6). For cisplatin, there was only a very small increase in accumulation with vessel volume (at 50 minutes of drug exposure (the half-life and peak of cisplatin exposure is two orders of magnitude shorter than that of pertuzumab<sup>3</sup>)), and only between the 1% and 10% volume cases. There was a 0.6% increase in maximum accumulation of cisplatin for Theoretical, and a 0.4% increase for the Empirical and Gaussian distributions (Fig. 4A). Maximum cisplatin accumulation over time appeared to be identical for all vessel volumes and vascular morphologies at all time points during IV or IP delivery, as the individual plot lines were indistinguishable from one another (Fig. 4B). For pertuzumab (Fig. 5, 6), accumulation increased with vessel volume in IP and IV delivery (except in the 3% case, which is higher than expected (Fig. 5C)), and shows correlation with vessel morphology from 1 to 10% volume (Fig. 5C).

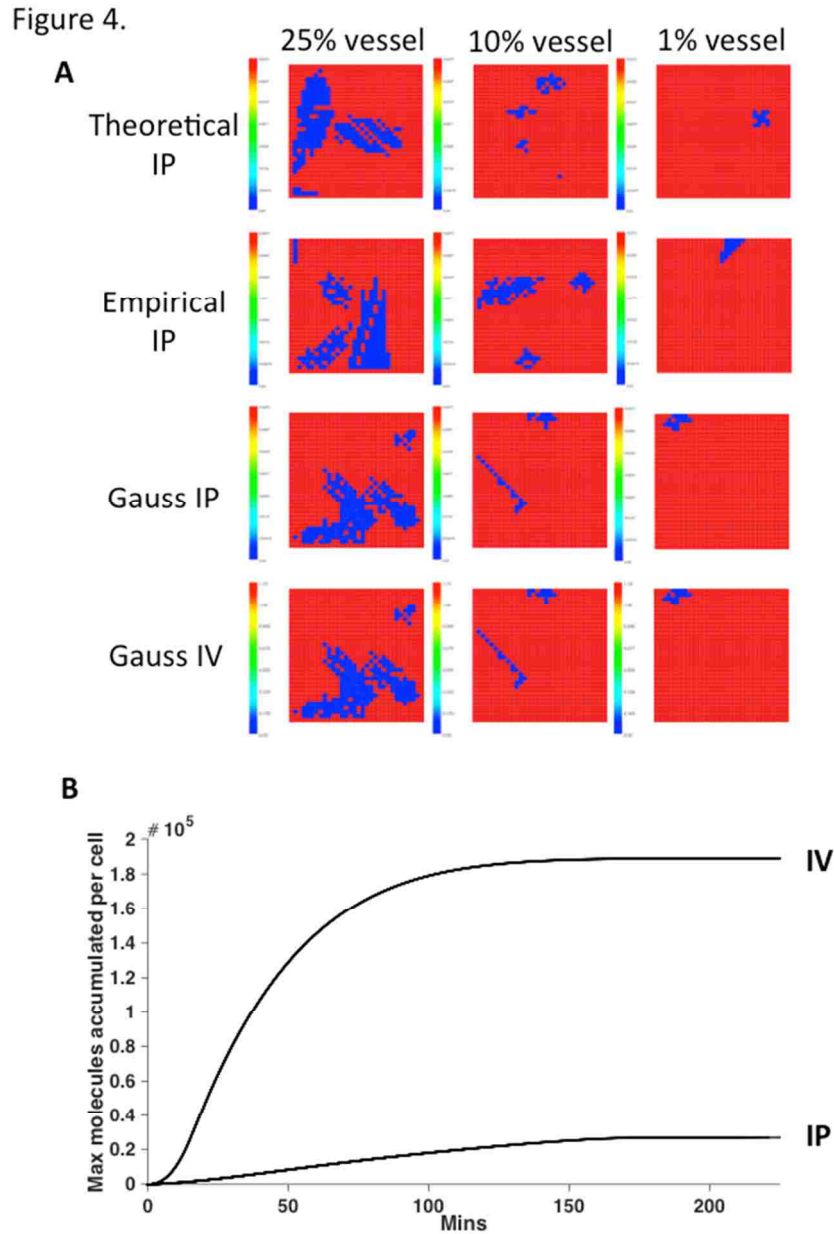


Figure 4: Simulation images show that cisplatin accumulation maximum (red) is uniform in the sample volumes and unaffected by vessel volume and morphology. Vessel = dark blue. Accumulation only depends on concentration of drug in the blood, which depends on route of delivery (IV is higher than IP). (A) Cisplatin accumulation in the tumor cells in the central xy plane ( $z=6$ ) of the  $30 \times 30 \times 10$  rectangular sample solids. Cell accumulation maxima ( $0.047 \mu\text{M}$  IV,  $1.19 \mu\text{M}$  IP) are uniform and nearly identical in samples undergoing the same form of delivery. (B) Cell with the highest accumulation is the same over time for all vascular volumes for each distribution.

Maximum accumulation (maximum value for at least one cell in the simulation) was substantially higher for both drugs in early IV delivery, and at all times for cisplatin IV (Fig. 4B, 5A). The plateau for IV cisplatin, shown in Figure 4B, occurring at ~120 min, was substantially higher (~10x) than that of IP, occurring at approximately 200 minutes. Pertuzumab IV maximum accumulation plateaued at 5 hours (Fig. 5A), while IP maximum accumulation plateaued (Fig. 5A and 5B) at later than 30 hours at roughly the same concentration as IV. The pertuzumab IV plateau also increased ~10% with an increase in vascular volume from 1 to 10%.

Figure 5.

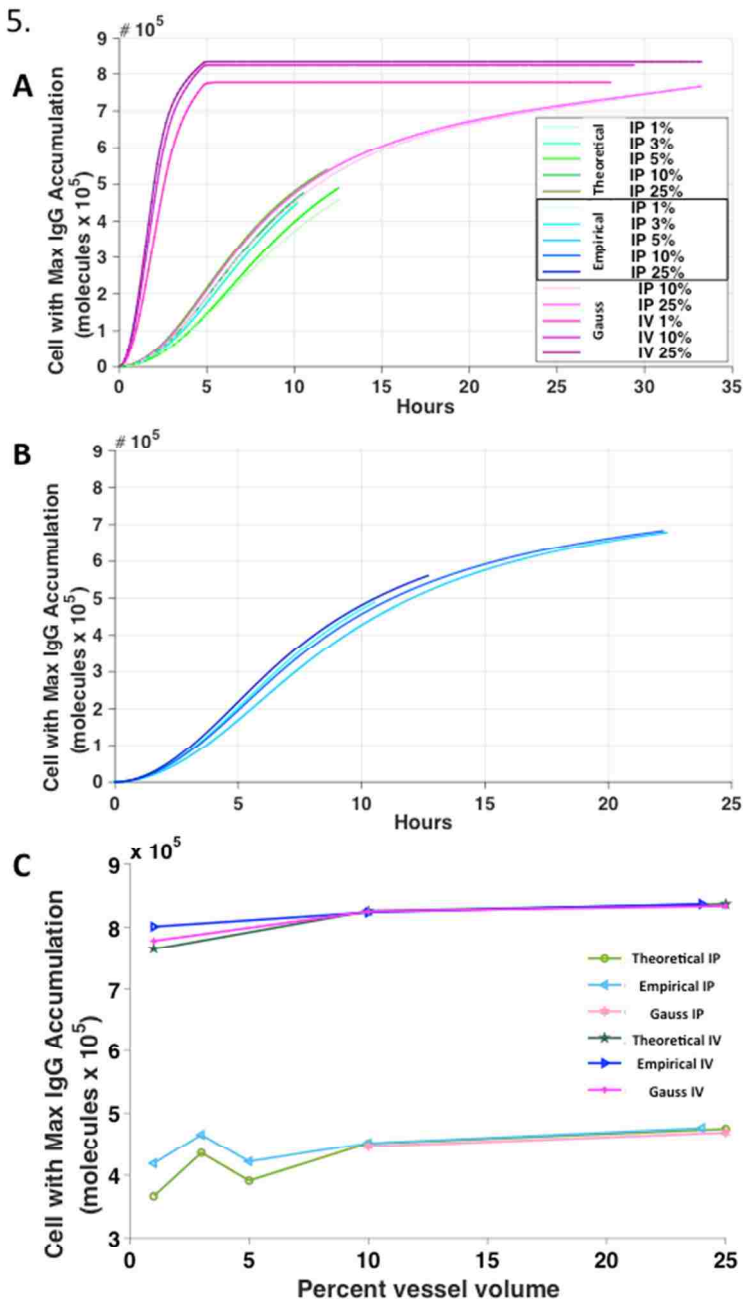


Figure 5: Maximum concentration of accumulated IgG in a single cell varies with vascular volume up to 10%, but does not depend on vessel radius distribution when vascular volume is  $>10\%$ . (A,B) Concentration of IgG molecules in the cell with maximum accumulation for (A) Theoretical IP and Gauss IP and IV, and (B) Empirical distribution IP. (C) Accumulation maxima correlate with vascular volume, and with vessel radius distribution up to 10% volume, whereafter the correlation seems to disappear. Maxima also depend on method of delivery, with IV providing the highest concentration.

Figure 6.

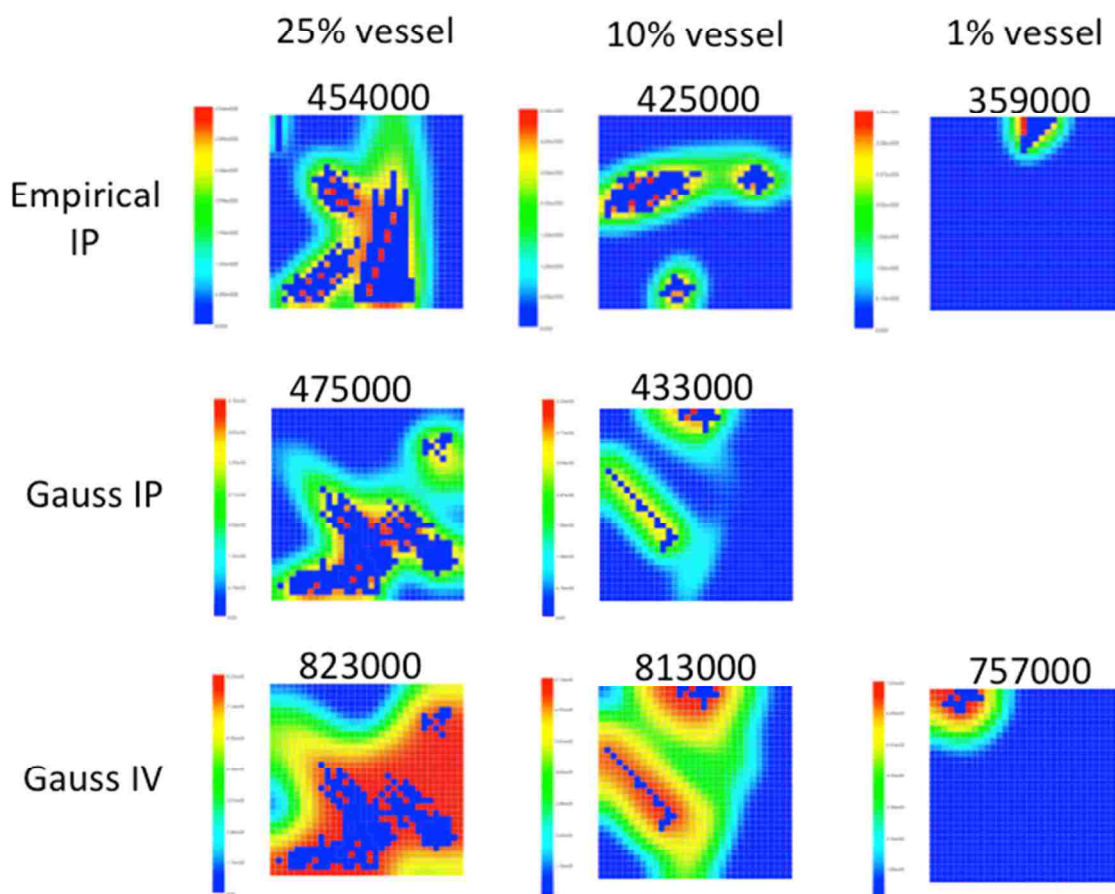


Figure 6. Pertuzumab accumulation in the tumor cells in the central xy plane ( $z=6$ ) of a selection of  $30 \times 30 \times 10$  rectangular sample solids from the 20 total models (IP, IV, pertuzumab, cisplatin, 1, 3, 5, 10, and 25% volume). Maxima in the plane are labeled above the samples. Vessels are royal blue and surrounded by red or yellow pseudocolored drug in each image. Otherwise, royal blue areas where there is a grid of uninterrupted cells represent low or zero drug accumulation.



There is no discernible heterogeneity of drug delivery of cisplatin (Fig. (4)). In contrast, Figures 6 and 7 show great heterogeneity across cells during delivery of pertuzumab to all vascular morphologies and volumes. Figure 7 shows a histogram of accumulation for the randomly selected 10x30x30 sample runs of pertuzumab from the 1, 10, and 25% vascular distributions, for IP and IV delivery methods, at 9.86 hours. We quantified heterogeneity as the Shannon entropy, which increases as the distribution it is testing becomes more uniform (closer to equal across the bins, counter-intuitively appearing as even-looking, homogeneous bins). The shapes of the distributions are distinctly different between the IP and IV simulations, but are highly similar amongst the different vascular distributions within the IV or IP simulations. The models demonstrate that heterogeneity increases with vascular volume during IP delivery (Fig. 7A, B, C). This is an artifact of the low concentrations delivered IP, but shows that vascular volume has an effect. Heterogeneity also increases between 1% and 10% vascular volume for the IV cases (Fig.7D, E), then drops for the 25% (Fig.7D, E) and Gaussian (Fig.7F) cases. Interestingly, this is because delivery is improving, and more cells are in the high accumulation bin for the high-vessel-volume samples. It is notable that at this time point (9.86 hours), all of the low-volume simulations and IP simulations have a very large count of cells below the threshold for ADCC, 100,000 molecules per cell (the lowest bin).

The mode of delivery has the highest effect on heterogeneity. IV creates the highest heterogeneity, again due to higher concentrations being delivered IV. Between the IV and IP cases, the lowest entropy (0.42) was in the Empirical IP 1% volume sample, and

the highest was in the Empirical IV 24% sample. This is actually a reflection of the Empirical distribution providing the lowest drug delivery in all cases (see Discussion). The Gaussian 1% and Empirical 1% are very close to each other in both the IV and IP cases, both delivering far less drug than the Theoretical. Heterogeneity increases between 1% and 10% vascular volume for all IV cases, then drops for the 25% Theoretical and Gaussian cases because of improved delivery.

Figure 7.

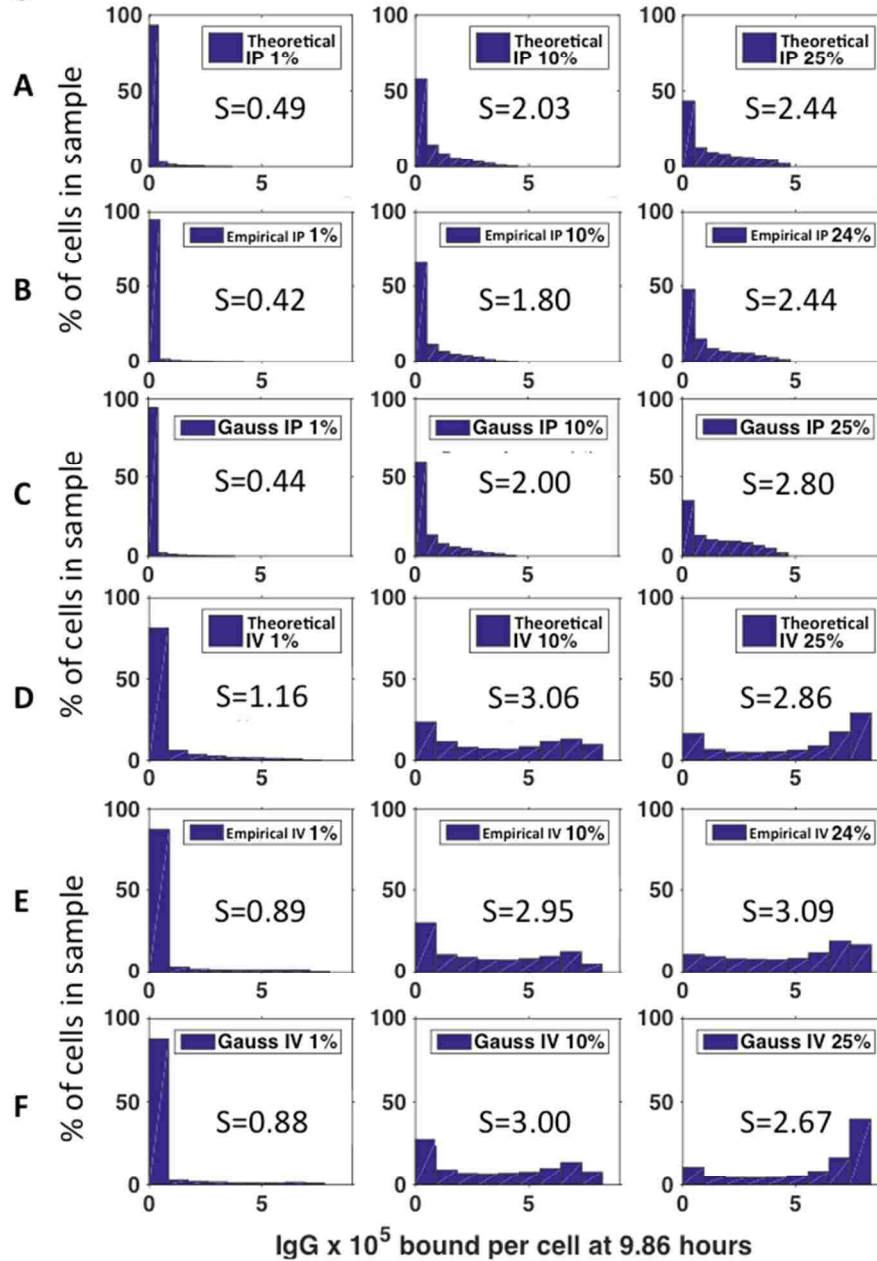


Figure 7. Histograms of pertuzumab accumulation in individual tumor cells at 9.86 hours given (A) Theoretical (B) Empirical and (C) Gaussian vessel distribution during IP delivery and (D) Theoretical (E) Empirical and (F) Gaussian vessel distribution during IV delivery. There is increased heterogeneity of accumulation when accumulation is highest, either through IV delivery or increased vessel volume. The shape of the distribution is similar within each mode of delivery for samples above 1% volume IP, or for all 1% and all IV samples. Delivery is poorest for the Empirical distribution in all cases; it is also the least heterogeneous (or equally heterogeneous in the IV 24% case) for all simulations except for IV delivery to 24% vessel, The Gauss and Theoretical distributions are less heterogeneous due to having more cells in the highest accumulation bin, indicating better delivery than in the Empirical.

Figure 8 shows the histograms approximating the total accumulation distributed within a cube inside of a large tumor, generated according to frequency of samples of similar vessel volume to those of the random sample models. These show similarity in the shapes of the curves between the three vascular distributions for IP (Fig. 7A) and IV (Fig. 7B) concentrations. They show the same increase in entropy when going from IP to IV delivery as in the small, random samples; this increase is again due to higher concentrations resulting in cells being distributed more uniformly across a range of drug exposures, rather than most cells being in the bin for accumulation of less than 100,000 molecules per cell, during IP delivery. To make comparisons about drug delivery between the distributions, the shape of the distribution must be examined in conjunction with the entropy, as they do not always correlate. Therefore, although the Theoretical results for the small samples are variable, for both the IP and IV cases of complete tumor, entropy is higher for the Theoretical distribution, and in these cases correlates with higher drug delivery, with fewer cells in the lowest bin than in the Empirical and Gaussian distributions. The results suggest that in the complete tumors, delivery is better for targeted therapies in tumor samples with vessel sizes that are similar to those in the Theoretical distribution (normal tissue).

Figure 8.

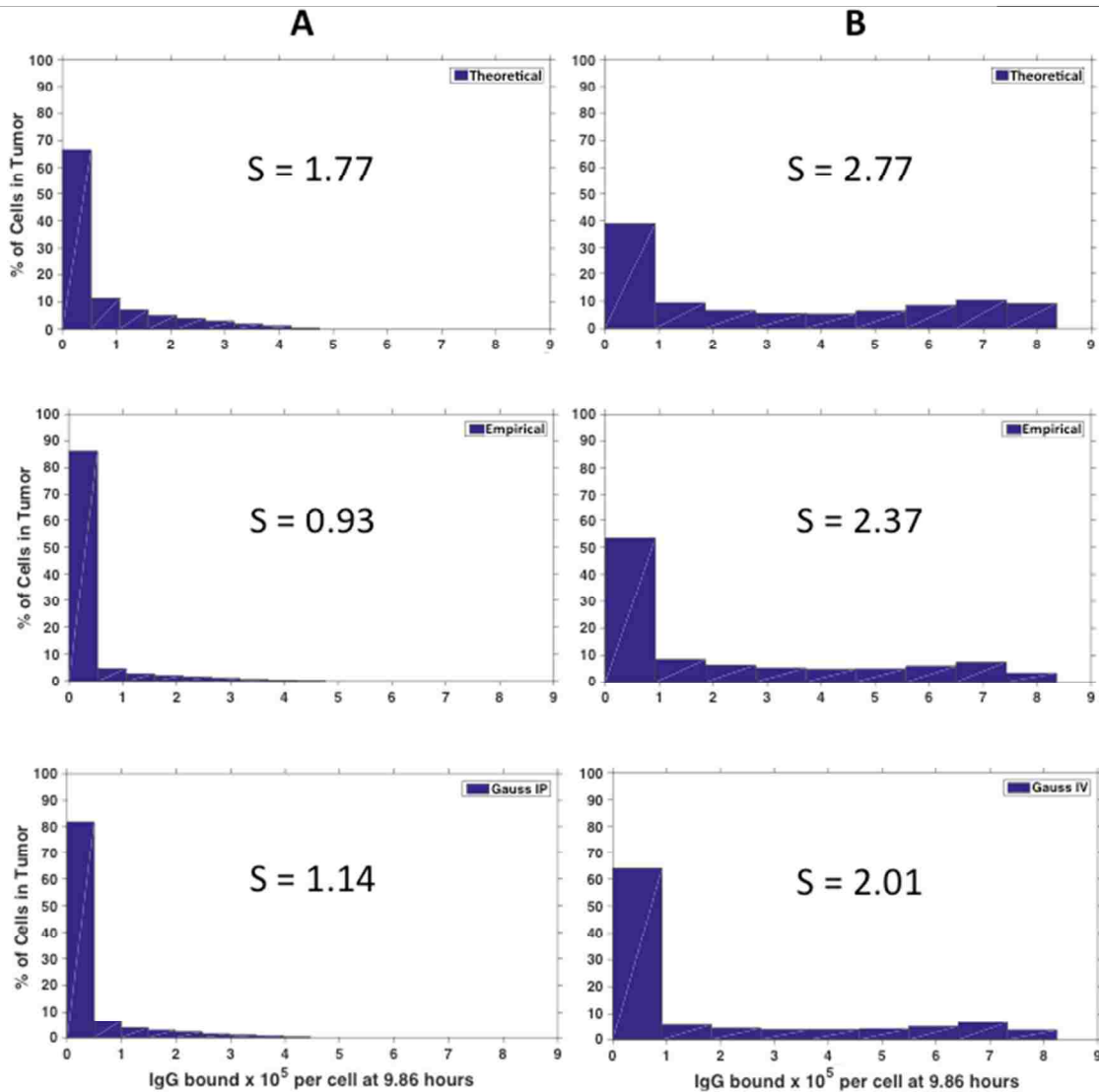


Figure 8: Histograms of pertuzumab accumulation in large tumors ( $R=140$  cells) at 9.86 hours created as composites from accumulation results of the simulations in small samples. Heterogeneity (entropy ( $S$ )) increases with increased plasma concentration due to the change in drug delivery (IV delivery  $>$  IP delivery). Theoretical delivers higher concentrations overall. (A) Range of accumulation in all cells after IP delivery to 140-cell-radius tumors with the Theoretical, Gaussian, and Empirical distributions. (B) Range of accumulation after IV delivery to the same tumors.

## DISCUSSION

Interestingly, our empirical vessel data is not similar to the distribution of radii from an idealized theoretical model<sup>8</sup>. This concurs with results by Herman *et al.*<sup>13</sup>, in which the radius distribution from tumors and normal tissue also differed, and in which it was theorized that tumors exhibit their own scaling exponent, derived from empirical data.

Using theoretical and empirically derived models of tumor vasculature, we see that vessel radius distribution and vessel volume affect the delivery of higher-molecular-weight targeted therapies such as the antibody pertuzumab, but not the small-molecule drug cisplatin. For pertuzumab, heterogeneity of accumulation (entropy), increases with an increase in vessel volume. It further increases with an increase of drug concentration in the vessels, as in IV delivery. However at high vessel volumes (25% case in Fig. 7D, E, F), entropy decreases for the Theoretical case and the Gaussian case, implying that these architectures give more even antibody delivery. This is despite the lack of large, leaky vessels represented in the Empirical model. Delivery is also improved in the Empirical 24% case, with entropy increasing because the lowest bin in the 10% case had the highest number of cells (Fig. 7E, 24%); cells that were previously receiving the lowest doses are moving up into higher bins, improving overall concentration, but also increasing entropy.

The models also imply that for the vessel volumes modeled, for both cisplatin and pertuzumab at clinical dosages (~2/3 the clinical maintenance dose in the pertuzumab IP case), the tumor tissues are receiving either almost completely inadequate drug in the IP

case for both drugs, or highly heterogeneous drug in the IV case for pertuzumab (Figs. (5, 6, 7, 8)). In particular, the composite histograms representing complete tumors show 38%-63% of the cells receiving less than the therapeutic threshold for ADCC. Because the models were built from the most vascularized case in patient ovarian disseminated tumors, ~10% area in a cross-section, this suggests that even highly vascularized tumors receiving high drug concentrations, whether containing many small vessels in the drug-delivering vessel volume, or the same volume instead partially comprised of large, leaky vessels, are not effectively delivering large-molecule antibody therapies to a large proportion of cells in the tumor.

For cisplatin, the morphology of the vascular tree does not affect maximum drug accumulation in any area of the tumor, and neither does vessel volume. However for pertuzumab, vessel volume does correlate somewhat with maximum accumulation during both IV and IP delivery. This result concurs with the drug delivery model of Pascal *et al.*<sup>12</sup>, which found the highest correlation between patient survival rates and fraction of cell kill, which in turn correlated with vessel volume. Our model suggests that, after therapy, if killing levels of drug were delivered only to some parts of the tumor, even if cell kill was higher, a large percentage of remaining cells will have also survived a wide range of sub-therapeutic concentrations. The interpretation of increased Shannon entropy would be that a wider range of signals -- drug levels -- has been given to the survivors, which are genetically heterogeneous, resulting in a variety of combinations of drug accumulation and genetic make-up. This begs the question of how important sub-therapeutic heterogeneity is -- could one homogeneous sub-therapeutic level, as in the

case of IP cisplatin delivery, drive resistance at the same rate as a heterogeneous distribution, or would they differ? It also reinforces the (obvious) idea that, for a given drug regimen, patients should be given the highest tolerable dose of drug to increase cell kill and to push toward less heterogeneous delivery and minimize survival of potentially resistant cells, rather than enhancing it with either heterogeneous sub-therapeutic and therapeutic drug, or more homogeneous but non-effective low levels of drug.



## **ACKNOWLEDGEMENTS**

Matthew Fricke, for help with statistical tests; Joshua Hecker for suggesting the Shannon Information metric as a measure of heterogeneity; the Scalenet lab for their generally helpful suggestions; and the Wilson Lab for the data on ovarian tumor vessel sizes.

## REFERENCES

1. Agarwal R, Kaye SB. Ovarian cancer: strategies for overcoming resistance to chemotherapy. *Nat Rev Cancer*. 2003;3(7):502–16. doi:10.1038/nrc1123.
2. Turner N, Reis-Filho J. Genetic heterogeneity and cancer drug resistance. *Lancet Oncol*. 2012. Available at: <http://www.sciencedirect.com/science/article/pii/S1470204511703357>. Accessed March 25, 2015.
3. Kanigel Winner K, Steinkamp MP, Lee R, et al. Spatial model of drug delivery route for treatment of disseminated ovarian cancer. *to be Submitt*. 2015.
4. Gerlinger M, Rowan AJ, Horswell S, et al. Intratumor Heterogeneity and Branched Evolution Revealed by Multiregion Sequencing. *N Engl J Med*. 2012;366:883–892. doi:10.1056/NEJMoa1113205.
5. Shen D-W, Pouliot LM, Hall MD, Gottesman MM. Cisplatin resistance: a cellular self-defense mechanism resulting from multiple epigenetic and genetic changes. *Pharmacol Rev*. 2012;64(3):706–21. doi:10.1124/pr.111.005637.
6. El-Kareh AW, Secomb TW. A theoretical model for intraperitoneal delivery of cisplatin and the effect of hyperthermia on drug penetration distance. *Neoplasia*. 2004;6(2):117–27. doi:10.1593/neo.03205.
7. Choi J, Credit K, Henderson K, et al. Intraperitoneal immunotherapy for metastatic ovarian carcinoma: Resistance of intratumoral collagen to antibody penetration. *Clin Cancer Res*. 2006;12:1906–1912. doi:10.1158/1078-0432.CCR-05-2141.
8. West GB, Brown JH, Enquist BJ. A general model for the origin of allometric scaling laws in biology. *Science*. 1997;276(5309):122–6. Available at: <http://www.ncbi.nlm.nih.gov/pubmed/9082983>.
9. Dvorak HF, Nagy JA, Dvorak JT, Dvorak AM. Identification and characterization of the blood vessels of solid tumors that are leaky to circulating macromolecules. *Am J Pathol*. 1988;133(1):95–109. Available at: <http://www.pubmedcentral.nih.gov/articlerender.fcgi?artid=1880651&tool=pmcentrez&rendertype=abstract>. Accessed June 9, 2014.
10. Nagy JA, Dvorak HF. Heterogeneity of the tumor vasculature: the need for new tumor blood vessel type-specific targets. *Clin Exp Metastasis*. 2012;29(7):657–62. doi:10.1007/s10585-012-9500-6.
11. Stamatelos SK, Kim E, Pathak AP, Popel AS. A bioimage informatics based reconstruction of breast tumor microvasculature with computational blood flow predictions. *Microvasc Res*. 2014;91:8–21. doi:10.1016/j.mvr.2013.12.003.
12. Pascal J, Bearer EL, Wang Z, Koay EJ, Curley S a, Cristini V. Mechanistic patient-specific predictive correlation of tumor drug response with microenvironment and perfusion measurements. *Proc Natl Acad Sci U S A*. 2013;110(35):14266–71. doi:10.1073/pnas.1300619110.
13. Herman AB, Savage VM, West GB. A quantitative theory of solid tumor growth, metabolic rate and vascularization. Monk N, ed. *PLoS One*. 2011;6(9):e22973. doi:10.1371/journal.pone.0022973.

## Chapter 5: Conclusion

In Chapter One, the cellular Potts model generated hypotheses that high homotypic adhesion and a mechanism for attraction to mesenteric blood vessels are fundamental parts of the ovarian cancer system. Both characteristics suggest exploitable weaknesses that could be used to disrupt the process of cancer relapse. In casual discussion with members of the New Mexico Center for the Spatiotemporal Modeling of Cell Signaling, the usage of a strong detergent during surgery to disrupt adhesion of non-attached cancer cells in the peritoneal cavity was suggested. Whether or not this particular idea is viable, it is the result of discussing the working mechanisms of the cancer process, and this is the job of the model: to help scientists envision a system so that they can think more deeply and creatively about it. The results of the invasion model, which require a special chemotactic factor to get spheroids to travel to vessels, are simple; yet, they stimulate conversations and ideas about what the mechanisms of this process may be (such as the dendritic cell "guides" to vessels that are seen in breast cancer), and provide testable hypotheses. Parameterizing the angiogenesis model led to a hypothetical threshold value of vascular endothelial growth factor to initiate angiogenesis in vascular endothelial cells, and re-examination of lab data, which showed that angiogenic factors are constitutively active in the cultured line of ovarian cancer cells used for the mouse xenografts.

In Chapter 3, models of tumors exposed to the peritoneal cavity demonstrated that drug delivery by the intraperitoneal route was more successful overall for both the chemotherapy cisplatin, and the targeted therapeutic monoclonal antibody Pertuzumab.

However, because vessels act as sinks for highly diffusible therapies such as Cisplatin when the concentration penetrating from the intraperitoneal cavity is higher than that in the vessel, heterogeneity of drug delivery increases in tumors with vascularization.

In Chapter 4, the drug delivery models show that, for tumor volumes unexposed to intraperitoneal delivery, IV delivery is superior to IP. In the case of Pertuzumab, delivery increases with vascular volume, and is also heterogeneous, leading to sub-therapeutic levels of treatment in the tumor sub-volumes of lowest vascularization. This opens to consideration how to conduct drug delivery when a patient has metastases distant from the peritoneal cavity, or large tumors that have grown since surgery, the center of which intraperitoneal drugs will not reach. The models also open the question of whether heterogeneous sub-therapeutic levels of drug or one homogeneous sub-therapeutic level of drug will drive faster evolution of drug resistance in tumors, which are genetically heterogeneous, potentially producing a greater variety of resistance responses to a greater variety of drug levels.

The results of Chapter 3 and Chapter 4 led us to consider that delivery of targeted monoclonal antibodies may benefit from usage of antibodies with medium rather than high affinity. High-affinity antibodies are so “sticky” that they cannot penetrate to deeper parts of the tumors. As we have discussed in our labs, further understanding of receptor recycling rates, receptor production rates, and avidity (rate of binding of the second arm of an antibody to a second receptor after initial binding to the cell surface by its first arm) could suggest mechanisms that could also be exploited in order to improve penetration of antibody therapies.

Our models have generated hypotheses about the mechanics that generate ovarian tumor morphology, which elements in the tumor microenvironment drive tumor behavior during invasion and angiogenesis, and how tumor vascularity and proximity to the abdominal cavity affect how well and how homogeneously they accumulate drugs. Such models can be leveraged to help us think about how we can decrease the fitness of a small tumor, either by disrupting its environment, its morphology, or by optimizing delivery of drugs both to increase cell kill and decrease heterogeneous delivery that could encourage the evolution of drug resistance.

Modeling of cancer systems requires us to examine in explicit detail the functional elements generating tumor behavior. Such guided thinking can lead to biological experiments that provide missing data or elucidate the workings of poorly understood mechanistic processes, and clinical procedures that can address inefficiencies of drug delivery. The utilization of models in envisioning biological systems has tremendous potential to accelerate the understanding and treatment of cancer and all disease. Their value in streamlining the production of hypotheses and experiments cannot be underestimated: modeling should always be considered as a component of research programs in human health. Modeling will play an increasingly important role in understanding the promise and limitations of cancer therapies.